



HAL
open science

Functional connectivity is preserved but reorganized across several anesthetic regimes

Guillaume Jean-Paul Claude Becq, Tarik Habet, Nora Collomb, Margaux Faucher, Chantal Delon-Martin, Véronique Coizet, Sophie Achard, Emmanuel Luc Barbier

► **To cite this version:**

Guillaume Jean-Paul Claude Becq, Tarik Habet, Nora Collomb, Margaux Faucher, Chantal Delon-Martin, et al.. Functional connectivity is preserved but reorganized across several anesthetic regimes. *NeuroImage*, 2020, 219, pp.116945. 10.1016/j.neuroimage.2020.116945 . hal-02935430

HAL Id: hal-02935430

<https://hal.science/hal-02935430>

Submitted on 10 Sep 2020

HAL is a multi-disciplinary open access archive for the deposit and dissemination of scientific research documents, whether they are published or not. The documents may come from teaching and research institutions in France or abroad, or from public or private research centers.

L'archive ouverte pluridisciplinaire **HAL**, est destinée au dépôt et à la diffusion de documents scientifiques de niveau recherche, publiés ou non, émanant des établissements d'enseignement et de recherche français ou étrangers, des laboratoires publics ou privés.

Functional connectivity is preserved but reorganized across several anesthetic regimes

Guillaume J.-P. C. Becq^{a,1,*}, Tarik Habet^b, Nora Collomb^{b,c}, Margaux Faucher^{a,b}, Chantal Delon-Martin^b, Véronique Coizet^b, Sophie Achard^{a,d,1}, Emmanuel L. Barbier^{b,c,1}

^a*Univ. Grenoble Alpes, CNRS, Gipsa-lab, F-38000, Grenoble, France*

^b*Univ. Grenoble Alpes, Inserm, U1216, Grenoble Institut Neurosciences, GIN, F-38000 Grenoble, France*

^c*Univ. Grenoble Alpes, Inserm, UMS017, CNRS, US3552, CHU Grenoble Alpes, IRMaGe, F-38000 Grenoble, France*

^d*Univ. Grenoble Alpes, Inria, CNRS, Grenoble INP, LJK, 38000 Grenoble, France*

Abstract

Under anesthesia, systemic variables and CBF are modified. How does this alter the connectivity measures obtained with rs-fMRI? To tackle this question, we explored the effect of four different anesthetics on Long Evans and Wistar rats with multimodal recordings of rs-fMRI, systemic variables and CBF. After multimodal signal processing, we show that the blood-oxygen-level-dependent (BOLD) variations and functional connectivity (FC) evaluated at low frequencies (0.031 - 0.25 Hz) do not depend on systemic variables and are preserved across a large interval of baseline CBF values. Based on these findings, we found that most brain areas remain functionally active under any anesthetics, i.e. connected to at least one other brain area, as shown by the connectivity graphs. In addition, we quantified the influence of nodes by a measure of functional connectivity strength to show the specific areas targeted by anesthetics and compare correlation values of edges at different levels. These measures enable us to highlight the specific network alterations induced by anesthetics. Altogether, this suggests that changes in connectivity could be evaluated under anesthesia, routinely used in the control of neurological injury.

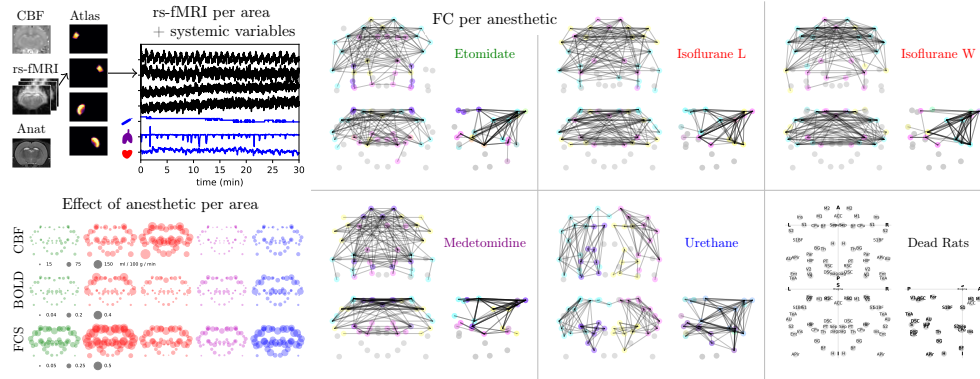
Keywords: anesthesia, cerebral blood flow (CBF), functional connectivity (FC), rat, resting state functional magnetic resonant imaging (rs-fMRI), systemic variables

*Corresponding author

Email addresses: guillaume.becq@grenoble-inp.fr (Guillaume J.-P. C. Becq), sophie.achard@univ-grenoble-alpes.fr (Sophie Achard), emmanuel.barbier@univ-grenoble-alpes.fr (Emmanuel L. Barbier)

¹These authors contributed equally to this work

Graphical Abstract



Highlights

- Different anesthetics lead to different systemic and brain alterations.
- BOLD variations and functional connectivity are affected by anesthesia.
- Systemic variables have little influence on functional connectivity.
- Baseline cerebral blood flow has no influence on functional connectivity.
- Anesthetics reshape distributions of connections.

Abbreviations

BOLD (blood-oxygen-level dependent), $\langle C \rangle$ (average correlation between signals of brain areas, or systemic signals), CBF (cerebral blood flow), FC (functional connectivity assessed by correlations between signals of brain areas in this study), FCS (functional connectivity strength, average correlation for one brain area), rs-fMRI (resting state functional magnetic resonant imaging), SV (systemic variables) such as HR (heart rate), RR (respiratory rate) and Temp (temperature).

1. Introduction

Resting state fMRI (rs-fMRI) is an elegant way to evaluate brain functional connectivity (FC) across species especially on Long Evans, Sprague Dawley or Wistar rats frequently used in the laboratory [1, 2, 3, 4, 5, 6]. While it is easy to ask a human subject to stay still, animals are either trained or anesthetized to limit motion artifacts [7, 2] (see also Appendix A). Training animals may however be too time consuming to be used in routine analysis and the stress from being restrained in a noisy environment could alter FC. The drawbacks of anesthesia are also well-known: it may change systemic variables (SV) such as temperature (Temp), heart rate (HR), respiration rate (RR) and at the brain level, it may alter neural activity, brain metabolism, baseline cerebral blood flow (CBF), and neurovascular coupling [8, 9, 10, 11]. A change in any of these variables may alter the FC mapped by rs-fMRI. This is why preclinical rs-fMRI data, obtained mostly under anesthesia, have been considered with some suspicion. This is related to two main questions: How can this apparent FC estimated from correlations between regional time series, reflect true brain connectivity? Is it possible, using standard methods, to evaluate whether brain connectivity is modified by the anesthetic? In order to map the impact of anesthesia on brain activity and metabolism, we want to evaluate potential biases on FC caused by confounding factors, SV and baseline CBF. Regarding SV, for a given data acquisition and processing protocol, changes in HR or RR may lead to change in the way the BOLD signal is contaminated by physiological noise [12, 13, 7, 14]. Anesthesia might change the frequency of microvascular oscillations, thus requiring an adaptation of the frequency band at which FC should be observed [15, 4, 16]; The effect of anesthesia on the regulation of Temp is also complex and results generally in an important cooling of the animal [17]. Baseline CBF is expected to alter the amplitude of the BOLD response induced by neural activity [18]. It has also been reported that changes in CBF may lead to changes in FC. Petrinovic et al. [19] acknowledge that an increase in baseline CBF could limit neurovascular reactivity and Jann et al. [20] observed positive correlations in human subjects between regional CBF and FC in all resting brain networks. Furthermore, Jonckers et al. [21] suggested that an increase in the variance of the BOLD signal could result in correlations that are less localized. A change in baseline CBF might thus modify the variance of the BOLD signal, the derived correlation coefficients, and thereby the apparent FC.

In this study, we explore large ranges of SV and baseline CBF using four different anesthetics and compare FC derived from long-run rs-fMRI recorded during 30 min with fast acquisition at 2 Hz. A processing pipeline to pick up the appropriate frequency bands to map FC is proposed. We show that FC is modified but preserved under anesthesia. Graphs of FC show different patterns and areas targeted by anesthetics.

2. Materials and methods

2.1. Animals

All experiments were approved by the local ethics committee and were performed in full compliance with the guidelines of the European community (EUVD 86/609/EEC) for the care and use of the laboratory animals, under permits from the French Ministry of Agriculture (number 380820 for EB and B3851610008 for experimental and animal care facilities). Experiments were conducted in the animal research facility of the Grenoble Institute of Neurosciences, a Specific Pathogen Free (SPF) housing facility, and comply with the ARRIVE guidelines [22]. Male rats were housed in enriched cages with 3 animals per cage and access to food and water ad libitum. Acquisitions dedicated to one anesthetic were conducted one after the other, with animals ascribed

Table 1: Systemic variables and baseline CBF.

	Eto-L	Iso-L	Iso-W	Med-L	Ure-L	Dead
N	7	6 (5)	7	7	7 (5)	4
W.	191±7	254 ± 55	316 ± 86	295 ± 23	289 ± 29	333 ± 51
Temp.	36 ± 2	<i>38 ± 0</i>	37 ± 1	37 ± 0	<i>38 ± 1</i>	–
HR	343 ± 51	<i>444 ± 26</i>	350 ± 34	219 ± 16	<i>383 ± 83</i>	–
RR	67 ± 11	<i>67 ± 11</i>	70 ± 3	73 ± 25	<i>108 ± 18</i>	–
SpO2	99 ± 1	<i>96 ± 5</i>	99 ± 0	98 ± 1	<i>75 ± 40</i>	–
N	7	6	6	6	7	–
CBF	25 ± 6	67 ± 10	101 ± 27	19 ± 2	41 ± 9	–

Notations: N - number of rats, *italic indicates missing physiological measures for some individuals*; W. weight (g); Temp. - temperature (°C); HR - heart rate in beats per minute (bpm), RR - respiration rate in cycles per minute (cpm); SpO2 - peripheral oxygen saturation (%) measured on the paw; CBF - baseline CBF (ml / 100 g / min)

45 to the group upon arrival order, with no other randomization. Once all anesthetics were tested,
46 about half the data was collected. A second run of acquisitions was then performed to obtain the
47 full dataset with a population target of at least 6 fMRI recordings per anesthetized group.

48 2.2. Experimental protocol

49 Four anesthetics are evaluated on Long Evans rats: Etomidate (Eto-L), Isoflurane (Iso-L),
50 Medetomidine (Med-L) and Urethane (Ure-L), with standard dosages. After an induction of
51 anesthesia with a gaseous mixture of isoflurane, air and oxygen, the anesthetics of the four groups
52 are the following during rs-fMRI: - Isoflurane (Iso): the level of the isoflurane is set to 1%. -
53 Etomidate (Eto): continuous intravenous infusion at 0.5 mg / kg / min. - Medetomidine (Med):
54 bolus then continuous infusion at 0.05 mg / kg / h. - Urethane (Ure): bolus of 1.25 g / kg injected
55 intraperitoneally. To evaluate whether animal strain biased this comparison, Isoflurane was also
56 administered to Wistar rats (Iso-W). A group of dead rats (Dead) was also created by sacrificing
57 4 animals. Overall, six groups were evaluated. The number of animals per group is given in
58 Table 1. Each Animal (n=34) was included in only one anesthetic group and was recorded only
59 one time, sacrificed if assigned to the Ure group or reused and sacrificed when randomly assigned
60 to the Dead group (n=4 with 1 Med-L, 2 Ure-L and 1 Iso-W). In this last group, recordings begin
61 one hour after sacrifice. Some recordings in CBF and SV were not available because of technical,
62 measurements or artefacts problems and were excluded from the study (cf. Table 1).

63 During rs-fMRI sessions, systemic variables are monitored and recorded: from a pulse oximeter
64 with a rat sensor clipped on the right posterior paw of the animal; a device measuring temperature
65 with a rectal probe and respiration rate from a small pneumatic pillow sensor. Measurements from
66 the two systems are sampled at 1 Hz. During the experiments a warm circulating water positioned
67 below the animal is regulated to maintain the body temperature to a target level of 37 °C inside
68 the MRI device. More technical and supplementary descriptions are given in Appendix B.

69 2.3. MRI Acquisitions at 9.4 T and data processing

70 CBF is mapped using pseudo continuous arterial spin labeling (pCASL) following inter-pulse
71 phase optimization as proposed in [23] with a spatial resolution 0.47 by 0.47 by 1.00 mm, gap
72 0.1 mm, 9 slices. rs-fMRI was performed with a single shot echo-planar imaging with TR/TE

73 = 500/20 ms, the same spatial resolution as CBF, and 3600 repetitions (30 min). fMRI BOLD
74 signals were first extracted on $N = 51$ brain areas from a home-made atlas based on published
75 ones [24, 25] after normalization of anatomical images and co-registration of fMRIs (Appendix B)
76 and signal extraction for each area with weighted averaging on voxels (Appendix D). SV and
77 BOLD signals are decomposed with wavelet transforms (Appendix B) with exclusion of samples
78 contaminated by movements (Appendix E). Correlations are performed on these signals to evaluate
79 FC (Appendix G).

80 2.4. Statistical analysis

81 To test for the difference of values between groups with unknown distributions, two-sided
82 Wilcoxon rank-sum tests, with an appropriate hypothesis for paired samples or independence
83 of samples are applied. The p -value is computed, and the hypothesis H_0 of the same mean of
84 populations is accepted or rejected at different levels: no reject (-), reject at 5 % (+), reject at 1
85 % (\times), reject at 0.1 % (\dagger). Pairwise comparisons are realized for different groups and a sequential
86 notation is given for each group as compared to the other. A small circle (\circ) is used to indicate the
87 position of the current variable. Not available comparisons are indicated by small bullets (\bullet). For
88 example, a comparison of the mean of three populations G1, G2, G3, with: G1 and G2 significantly
89 different at $1e-3$; G2, G3 at $5e-2$; and G1, G3 not significantly different, will be noted with the
90 three sequences : ($\circ \dagger -$) for G1, ($\dagger \circ +$) for G2, and ($- + \circ$) for G3. When linear regressions are
91 estimated on bivariate samples, the null hypothesis that the slope of the regression is 0 is tested
92 with a Wald test using t -values. Significant correlation coefficients are obtained by computing
93 p -values based on ad-hoc hypothesis tests for correlations and wavelets [26, 27] and adjusting for
94 multiple corrections. (see also Appendix G).

95 2.5. Data availability

96 Data and codes are available at DOI 10.5281/zenodo.2452871.

97 3. Results

98 3.1. Effects of anesthesia on SV and baseline CBF

99 Number of animals per group, means (m.) and standard deviations (sd.) of SV measured
100 during the fMRI protocol are given in Table 1 and distributions of values with box plots are given
101 in Fig. 1.

102 SV have usual ranges observed during anesthesia on rats, with high HR for Iso-L, unstable HR
103 for Eto-L and Ure-L (sd. $> 15\%$ m.), high RR for Ure-L, and difficulty to measure peripheral
104 oxygen saturation as a consequence of the cooling of peripheral limbs for Ure-L (missing values
105 and one individual with low values, see Fig. 1d). Homogeneous values of variables are observed
106 within groups (scatter plots of pairs of SV given in Fig. I.20, Fig. I.21 and Fig. I.22). There is a
107 relationship between HR and Temp ($R = 0.56$, $p < 0.01$). Baseline CBF is significantly different
108 between groups (Fig. 1g). The highest baseline CBF is observed under isoflurane (Iso-L: 67, Iso-W:
109 101 ml / 100 g / min), with an influence of the rat strain. The lowest baseline CBF is obtained
110 for Med-L (19 ml / 100 g / min), in line with previous reports [28, 29, 30]. Relationships between
111 baseline CBF and SV are only significant for HR ($R = 0.56$, Fig. I.20) and Temp ($R = 0.49$,
112 Fig. I.22). Overall, anesthetics change SV and baseline CBF values with induced steady states for
113 each group.

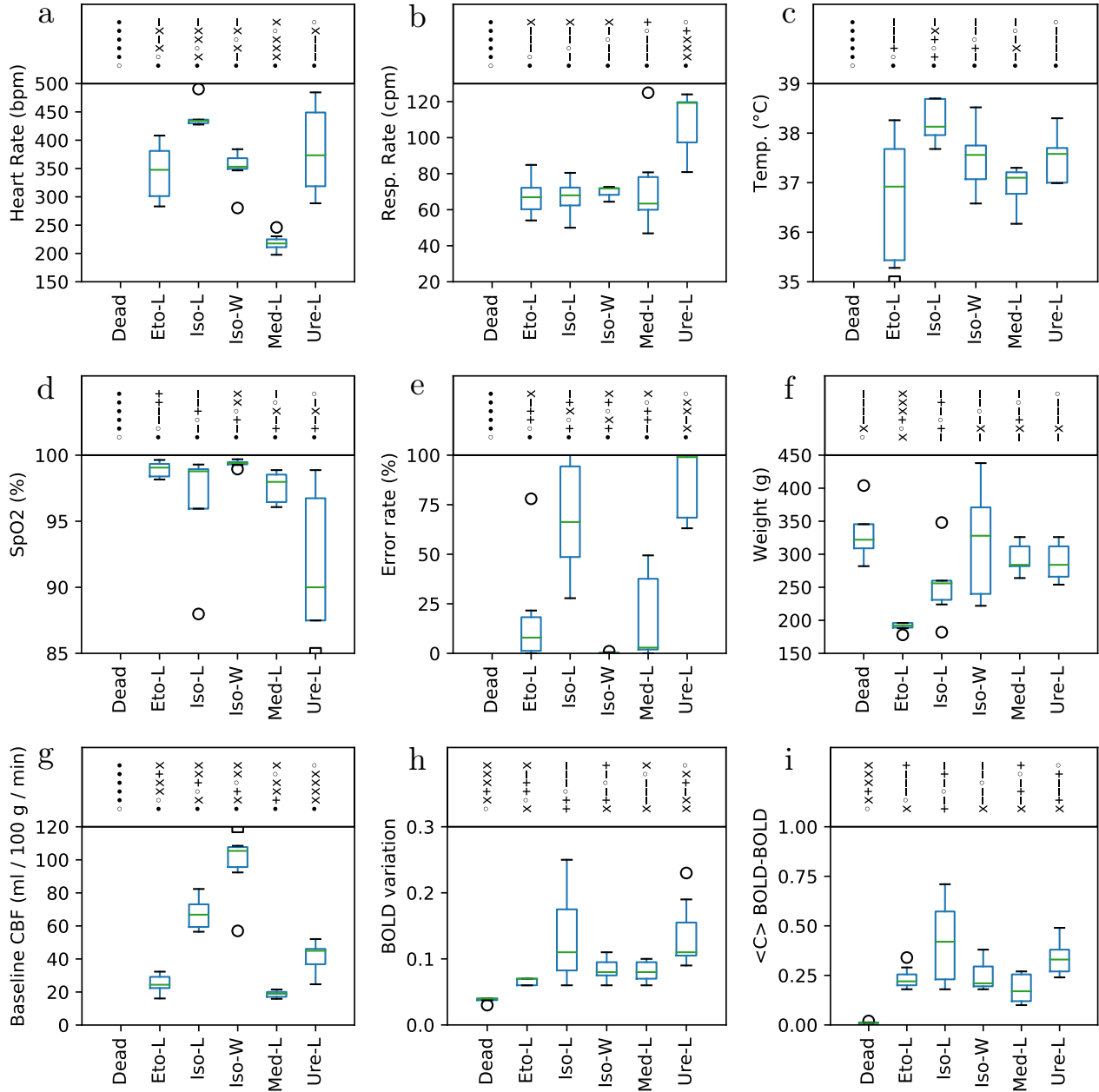


Figure 1: Distributions of variables per group with box plots. The distributions are represented by boxes and whiskers: green bars indicate median values, upper and lower sides of the boxes indicate the 1st and 3rd quartiles, whisker bars are given for values under 1.5 times the interquartile limits and circle markers indicate outlier values outside this interval. Square markers indicate outlier values out of the plot range. Above each whisker plot, the p -value of the test of comparison of distributions with the other groups (unpaired Wilcoxon tests). Markers indicate the level of significance of the p -values: $- > 0.05 > + > 0.01 > \times > 0.001 > \dagger$. The position of the reference group is indicated by \circ and unavailable comparison by \bullet .

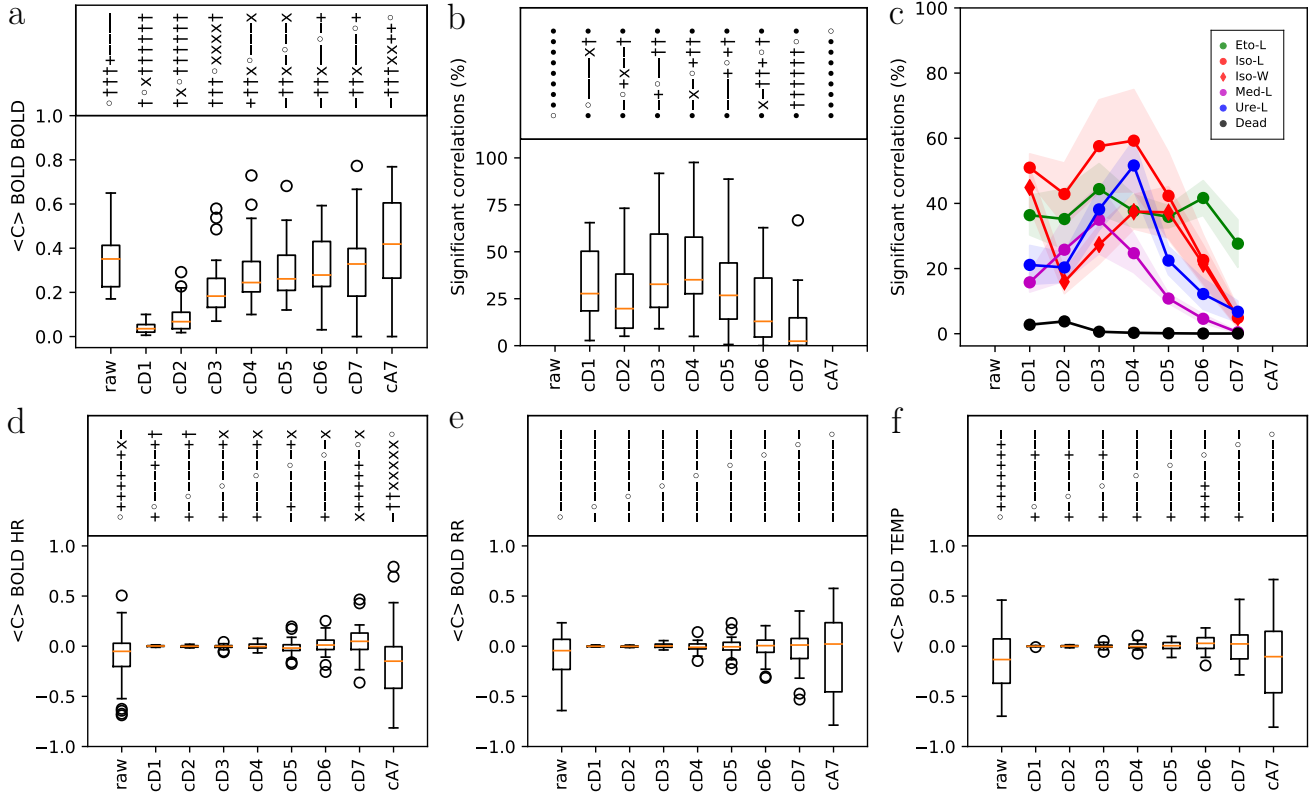


Figure 2: Distributions of correlations by frequency bands. a) Whisker plots of $\langle C \rangle$ BOLD-BOLD, the mean functional connectivity between BOLD signal pairs at a given frequency band for all 51 brain areas, averaged across all animals, as a function of frequency band. b-c) Global and per group distributions of the percentage of significant correlations per frequency band. d-f) Whiskers plots for $\langle C \rangle$ BOLD-HR $\langle C \rangle$ BOLD-RR and $\langle C \rangle$ BOLD-Temp, the average correlation between heart rate (HR), respiratory rate (RR) and temperature (Temp.) signal, and BOLD signals, at a given frequency band.

114 3.2. SV, BOLD signals and FC across frequency bands

115 fMRI BOLD signals were first extracted on $N = 51$ brain areas from a home-made atlas
116 based on published ones [24, 25] (see materials and methods and Appendix C for details). As
117 BOLD signals and SV were simultaneously recorded, we evaluated the relationship between BOLD
118 signals with themselves (BOLD-BOLD) and with SV (BOLD-HR, BOLD-RR and BOLD-Temp)
119 for different frequency bands after motion filtering (see materials and methods Appendix E for
120 details). Frequency bands are obtained using dyadic wavelet transforms. The decomposition is
121 done on rs-fMRI raw signals (raw) to yield signals corresponding to detail coefficients at different
122 scales (cD1 - cD7) and one signal corresponding to approximation coefficients (cA7). The frequency
123 bands are, in Hz: $cA7 < 0.008 < cD7 < 0.016 < cD6 < 0.031 < cD5 < 0.063 < cD4 < 0.125 <$
124 $cD3 < 0.25 < cD2 < 0.5 < cD1 < 1$. Let C_{ij} be the BOLD-BOLD correlation coefficient between
125 signal from area i and signal from area j . The functional connectivity strength (FCS)² for node i is
126 defined as $FCS_i = 1/(N - 1) \sum_{j,j \neq i} C_{ij}$. The mean FCS is then defined as $\langle C \rangle_{\text{BOLD} - \text{BOLD}} =$
127 $1/N \sum_i FCS_i$. For SV signals, we defined $\langle C \rangle_{\text{BOLD} - \text{SV}} = 1/N \sum_j C_{SVj}$ where C_{SVj} is the
128 BOLD-SV correlation between SV signal and signal from area j . Each of these quantities are
129 computed for each frequency band using the corresponding wavelet coefficients.

130 Fig. 2a represents the distributions of $\langle C \rangle_{\text{BOLD} - \text{BOLD}}$ in function of frequency bands over all
131 animals. $\langle C \rangle_{\text{BOLD} - \text{BOLD}}$ increases with the frequency bands with significant differences from
132 cD1 to cD3 with other scales, and median close to 0 for cD1 - cD2. Significant BOLD-BOLD
133 correlation coefficients are obtained by computing p -values based on ad-hoc hypothesis tests for
134 correlations and wavelets [26, 27] and adjusting for multiple corrections (see Appendix G for
135 details). Fig. 2b,c shows a maximum of significant correlations for the frequency band cD4, where
136 mean \pm standard error of the mean ($M \pm \text{SEM}$) are represented for each anesthetic in Fig. 2c. To
137 validate our method, a group of dead rats (Dead) was created by sacrificing 4 animals. Almost no
138 significant BOLD-BOLD correlations are obtained on this group. Fig. 2d-f shows that the variance
139 of $\langle C \rangle_{\text{BOLD} - \text{HR}}$, $\langle C \rangle_{\text{BOLD} - \text{RR}}$ and $\langle C \rangle_{\text{BOLD} - \text{Temp}}$ increases with the observed frequency
140 band. Interestingly, as frequency band increases, the median $\langle C \rangle_{\text{BOLD} - \text{BOLD}}$ increases faster
141 than the variance of $\langle C \rangle_{\text{BOLD} - \text{SV}}$. This suggests that there is a frequency band for which the
142 ratio between the median $\langle C \rangle_{\text{BOLD} - \text{BOLD}}$ and the variance of $\langle C \rangle_{\text{BOLD} - \text{SV}}$ is optimal. This
143 band corresponds to a maximum in edges detection based on signal and not noise, as confirmed by
144 the number of significant BOLD-BOLD correlation coefficients per animal given in Fig. 2c. cD4
145 seems a good compromise for all groups, even though for some anesthetics the same number of
146 significant correlations can be found for cD3 to cD5 (0.031 - 0.25 Hz). The cD4 band (0.063 -
147 0.125 Hz) is thus retained to compute BOLD-BOLD correlations. In the remainder of this paper,
148 BOLD signal corresponds to the BOLD signal filtered in this band.

149 3.3. BOLD variations and FCS are independent of baseline CBF

150 To evaluate the impact of baseline CBF on BOLD signals, we computed the standard deviation
151 of the BOLD signal for each brain area, denoted as BOLD variation. Fig. 3a shows the BOLD
152 variation as a function of baseline CBF, binned per CBF intervals of 10 ml / 100 g / min and
153 averaged across rats per group, with values given in $M \pm \text{SEM}$. Despite the broad range of baseline
154 CBF values, almost flat curves are observed for each anesthetic over a large range of CBF values.
155 Similar results are obtained for different frequency bands (see Fig. I.31). Fig. 3b shows similar

²This definition is related to the one proposed in [31] or the normalized version of vertex (node) strength or weighted degree proposed in [32, 33]

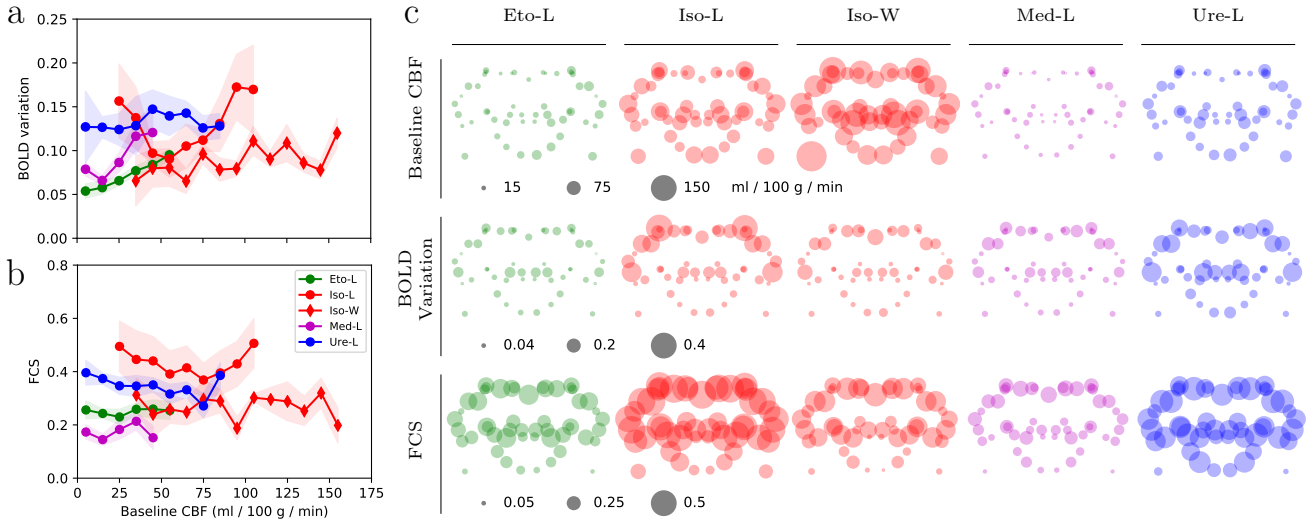


Figure 3: Relationships between baseline CBF, BOLD variation and FCS. a) Average values of BOLD variation per CBF bin and per group with at least 4 animals. b) Functional connectivity strength (FCS) per CBF bin and per group with at least 4 animals. c) Comparison per group on each node for baseline CBF, BOLD variation and FCS. Each area is represented by a node located at its center of gravity on a coronal projection. Node diameter is related to parameter value.

156 almost flat curves obtained for FCS as a function of baseline CBF. This indicates that average
 157 values of BOLD variation and FCS do not depend on the average baseline CBF values. There
 158 is no significant relationship between baseline CBF and BOLD variation or $\langle C \rangle$ BOLD-BOLD
 159 (Fig. I.26), but there is a significant relationship between BOLD variation and $\langle C \rangle$ BOLD-BOLD
 160 ($R = 0.87$, $p < 0.001$) (Fig. I.27). Fig. 3c shows, per group, a coronal view of baseline CBF,
 161 BOLD variation and FCS in the brain. It further suggests that CBF, BOLD variation and FCS
 162 are not tightly linked. For example, even if CBF is high for Iso-W, BOLD variation is low. For
 163 high baseline CBF values observed in the Iso groups, the measures in BOLD are high for Iso-L
 164 and medium for Iso-W. Eto-L and Med-L produces similar patterns, with low values for all three
 165 variables. Altogether, the FCS patterns seem similar across all anesthetics, not sensitive to either
 166 CBF or BOLD variation.

167 3.4. Anesthetics target specific brain areas and reshape distribution of connections

168 For each group of rats, average correlation matrices are computed. Based on our results in
 169 Fig. 2c, edges not significantly different to zero correlations are removed. FCS per group and
 170 area are presented in Fig. 4a with FCS computed here using $FCS_i = \frac{1}{N_i} \sum_{j \in S_i} C_{ij}$ with S_i
 171 the set of significant correlations for area i and N_i the number of elements in S_i . This approach is
 172 validated on the group of dead rats where no connections remain. When computing the average
 173 correlation matrices for the other groups of rats, 9 areas only are not significantly different from
 174 noise. This means that at most 9 (/51) brain areas, or 6 (/26) by grouping bilateral areas can
 175 not be differentiated from random signals, whatever the anesthetic. Hence, we can not conclude
 176 on their specific connections with other areas. On average, sensory (S1, S1BF, S2), motor (M1,
 177 M2) and cingulate cortex (ACC) areas have the highest correlation values. This is emphasized by
 178 Fig. 4b where areas are ranked from the most connected area to the least one. Depending on the
 179 anesthetic, some areas are more connected in some groups (e.g. V1 in Iso-L, Ins in Iso-W, Th in

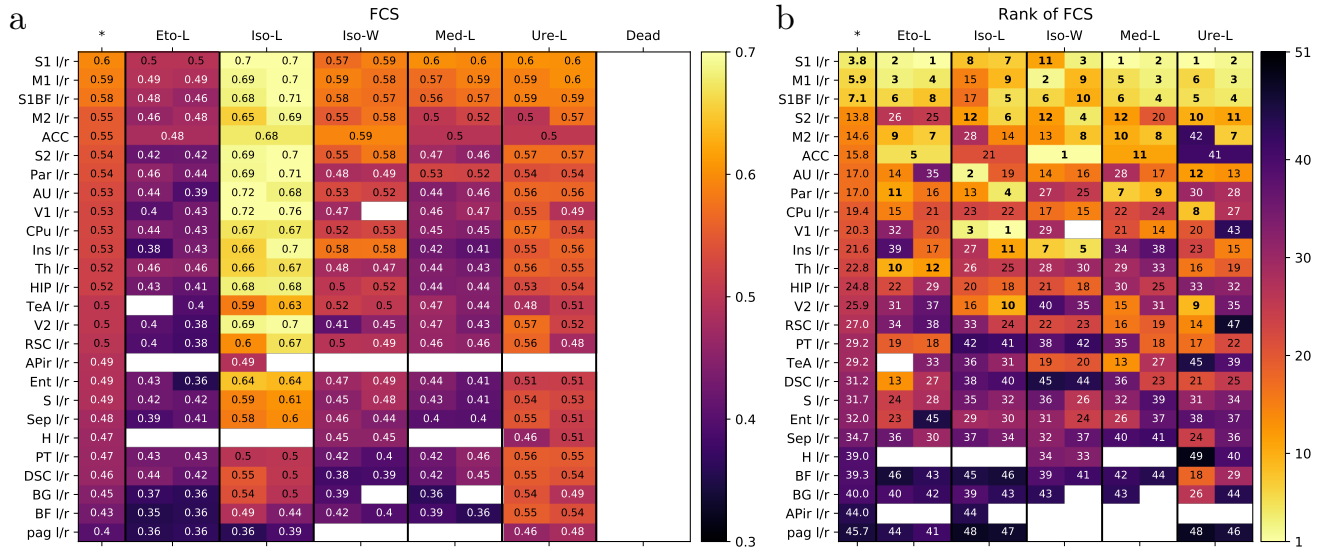


Figure 4: Graph measures and representations per group of average matrices. Average was performed on significant correlations at a symmetrical level $\alpha = 5\%$ (Bonferroni corrections $p=2e-5$) and if present in a minimum of 4 animals per group. (a) FCS. Each area is represented by two columns (left and right hemispheres), except for ACC which is central and for column * which is the average of anesthetized groups. Areas are sorted from this column. Unavailable FCS from areas with no detected edges are not plotted (white). (b) FCS rank per group, sorted from highest to lowest. A rank of 1 indicates that the area has the highest FCS in its group. Areas showing the lowest ranks (first quartile) are in bold. The first column * is the average of anesthetized groups. Areas are sorted from this column. Notations: l: left, r: right, ACC: anterior cingulate cortex, APir: amygdalopiriform transition area, AU: auditory cortex, BF: basal forebrain region, BG: basal ganglia, CPu: caudate-putamen striatum, DSC: superior colliculus, Ent: entorhinal area, Ins: insular cortex H: hypothalamic region, HIP: hippocampus, M1: primary motor cortex, M2: supplementary motor cortex, pag: periaqueductal gray, Par: parietal association cortex, PT: pretecal region, RSC: retrosplenial cortex, S: subiculum S1: somatosensory 1, S1BF: somatosensory 1 barrel field, S2: somatosensory 2, Sep: septal region, TeA: temporal cortex association area, Th: thalamus, V1: primary visual cortex, V2: secondary visual cortex.

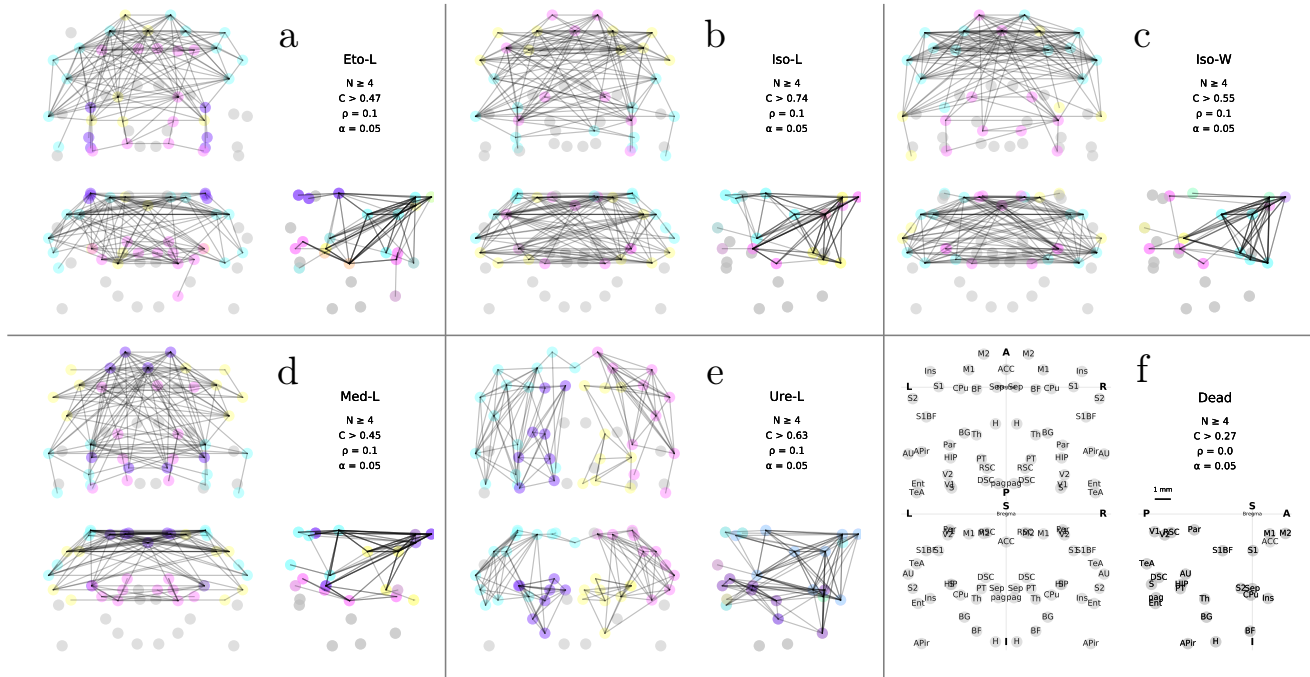


Figure 5: Graph representations of average matrices per group. Average was performed as in Fig. 4. (a)-(f) Graphs based on the average correlation matrices obtained with the frequency band cD4 for all group. The 127 most correlated values (density $\rho = 0.1$) are plotted. Gray nodes represent unconnected nodes and nodes with the same arbitrary color belong to the same community. For each group, the number of animals, the lowest correlation value used in the graph, and the correlation significance threshold are mentioned. (f) The Dead group shows no significant connections. Notations same as Fig. 4 with L-R: left-right axis, A-P: antero-posterior axis, I-S: inferior-superior axis.

180 Eto-L) or less connected (e.g. Acc in Ure-L, S2 and AU r in Eto-L). Asymmetries between left
 181 and right areas may also be observed (e.g. Ins and AU in Eto-L, M2 in Iso-L and Ure-L). These
 182 observations should be mitigated by the fact that FCS values show a moderate but significant
 183 relationship with the area location in the MRI device ($R=-0.68$, $p < 0.001$), and, at a lesser level,
 184 with the area size ($R=0.56$, $p < 0.01$) (Appendix H), with low values of FCS obtained for small and
 185 far from the coil areas, such as TeA. After verifying that correlations did not originate from spurious
 186 neighboring signal contamination by evaluating the presence of significant long-range correlations
 187 in each group (Fig. H.16), graphs were constructed per group to highlight local differences in
 188 connectivity.

189 Fig. 5 displays the thresholded correlations with a density³ $\rho = 0.1$. Nodes communities
 190 detected by clustering are given in color (details in Appendix B). The graphs of anesthetized groups
 191 are structured with the anterior cingulate cortex (ACC) taking a central place in connectivity.
 192 Among the acquired nodes, nodes with low FCS seem less connected for some groups (H, BF, BG,
 193 APir, pag). There is also an obvious loss of the inter-hemispheric connections in the Ure-L group
 194 and a loss of the cortical-subcortical connections in the Med-L group. This is further confirmed
 195 by individual graphs and other representations proposed in Fig. I.32 to Fig. I.37 and Fig. I.38.

196 Finally, we summarized the impact of anesthetics from graphs of Fig. 5 by representing the ratio
 197 of connections between ACC, cortical (c), subcortical (s), interhemispheric (inter) or intrahemi-

³The number of retained edges over the number of all possible edges

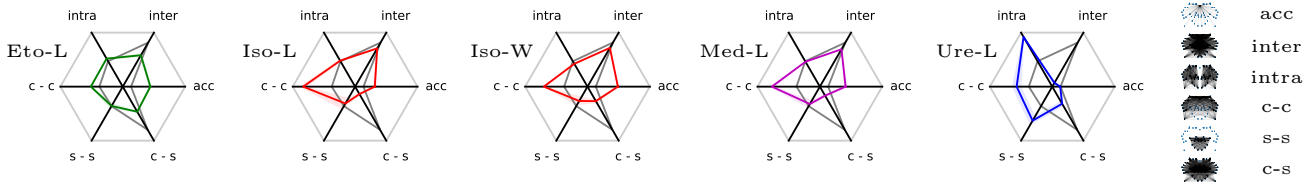


Figure 6: Radar representations of average matrices per group. Average was performed as in Fig. 4. Radar plots represent the distributions of connections for the graphs presented in Fig. 5, obtained at a density $\rho = 0.1$. Gray curve represents percentages for the fully connected graph. Notations: acc: anterior cingulate cortex, inter: interhemispheric, intra: intra-hemispheric, c: cortical, s: subcortical.

198 spheric (intra) areas. Fig. 6 shows the spatial reorganization of the 10% strongest correlations,
 199 given by graphs at density $\rho = 0.1$. We observe low ACC FC for Ure-L, very low inter FC for
 200 Ure-L, low inter FC for Eto-L, and low c-s FC for Iso-L, Med-L and Iso-W (see Appendix H for
 201 values and comparison with other densities).

202 In summary, depending on the anesthetic and the animal strain, 25 to 60% of the total possible
 203 connections are significant with at least 80% of areas connected to at least one other area, with
 204 reordering of the strongest connections.

205 4. Discussion

206 4.1. Summary of findings

207 After observing that SV and CBF under anesthesia were stable, we introduced an approach
 208 based on wavelet decomposition to identify the optimal frequency bands to analyze FC and the
 209 number of significant correlations between areas. This approach limits the interaction with SV
 210 and improves the signal to noise ratio for the detection of significant graph edges. Using this
 211 method, and data including baseline CBF and rs-fMRI acquired in rats under several anesthetic
 212 conditions, we observed that, in the low frequency band 0.06-0.12 Hz, BOLD variation and FCS
 213 are independent of baseline CBF. Overall, the vast majority of brain areas are connected together
 214 with anesthetic dependent connectivity patterns.

215 4.2. Impact of anesthetics on SV, choice of BOLD frequency bands and FC

216 SV values reported in this study are inline with previous reports using comparable anesthetics
 217 and preparations [34, 35, 3, 36, 4]. Fig. 2d-f indicate that, whatever the baseline SV, fluctuations
 218 of SV in some frequency bands (cD3 - cD5: 0.031 - 0.25 Hz) do not correlate with spontaneous
 219 BOLD signals during the 30 min acquisition. We also evaluated whether the SV averaged across
 220 the acquisition duration and the BOLD variation averaged in the same way were correlated when
 221 considering all animals. With this approach, correlations were observed between average SV and
 222 average BOLD variations (Fig. 3; e.g. Temp. vs BOLD variation), possibly resulting from the
 223 increased variability of SV fluctuations at frequencies below 0.031 Hz. Altogether, despite the
 224 broad range of SV conditions produced by the use of different anesthetics, SV fluctuations did not
 225 contaminate BOLD signal in the 0.031 - 0.25 Hz band for a 30 min acquisition.

226 Modifications on signals may also be related to movements of the animals. Since animals were
 227 restrained with teeth and ear bars, the contamination of the BOLD signal is less probable than
 228 in human studies. Nevertheless, motions can occur and a classical scrubbing method with boxcar
 229 filtering [37] has been applied, taking into account HRF and wavelet support at different scales (see
 230 Appendix E). Alternative methods to filter out SV and movements exist and are recommended by

231 other studies [38], but they lead to complex modifications of signal that may prevent a quantitative
232 analysis of correlation coefficients and lead to controversial results, as for example with global
233 signal regression (GSR) [39]. Transformations of correlations are also complex to interpret when
234 working with non-Gaussian processes and lead to distributions of correlations that are difficult to
235 compare [5, 40, 41, 42, 6]. Without any transformations, the distributions of correlations (Fig. I.29)
236 are comparable with the ones presented in [43, 44, 45] and show influences of anesthetics on $\langle C \rangle$.
237 It would however be of interest to further investigate and compare these different transformations.

238 The study of the number of significant correlations as a function of the frequency band seems
239 a useful step to optimize and validate the FC processing pipeline. We advocate the use of both
240 dead rats [4] and random simulations [27, 46]. Indeed, empty graphs may be obtained when the
241 signal to noise ratio is too low (Fig. 5), and thereby enhance contrast for specific communities
242 and networks. The selected frequency band (cD4: 0.062 - 0.125 Hz), determined by experimental
243 constraints and mathematical framework, was narrower than previous experimental reports but
244 included, like most reports, frequencies below 0.1 Hz (see Appendix F). Bandwidths could be
245 further adjusted for example by merging some of them, also based on observations of the power
246 spectrum of signals (Appendix F) as given in [4, 44, 16]. Since the velocity of the hemodynamic
247 response depends on baseline CBF [18], the optimal frequency band could depend on the type of
248 anesthetic or on the animal strain [15, 4, 16]. Since no correlations between baseline CBF and
249 BOLD variations in the cD4 band were observed, our data do not demonstrate this point, in line
250 with a previous report showing that spontaneous sinusoidal oscillations may exist over a range of
251 anesthesia depths [47]. This is also inline with BOLD variations caused by arteriole vasomotor
252 variations [48] under the control of locally regulated vasoactive substances [49, 50]. The method
253 we propose could be adjusted to explore narrower frequency bands and thereby smaller change in
254 hemodynamic response function, based on longer rs-fMRI acquisitions.

255 *4.3. Impact of anesthetics on baseline CBF, BOLD variations, and $\langle C \rangle$ BOLD-BOLD*

256 The choice of anesthetic and of animal strain changed the baseline CBF, a parameter corre-
257 lated to mean HR and mean Temp (Fig. I.30). Baseline CBF was however independent of BOLD
258 variations and of FCS (Fig. 3). This is in line with [51] but seems in contradiction with previous
259 reports, which demonstrated that an increase in baseline CBF decreases the BOLD signal ampli-
260 tude, comparable to the BOLD variation in our study [18]. The difference with [18] is that a change
261 is observed in one given brain area, whereas all brain areas with the same CBF are averaged in
262 our study. Mean $\langle C \rangle$ BOLD-BOLD were however dependent on HR and Temp, suggesting that
263 this parameter is not fully independent of baseline physiology. Mean arterial pressure could also
264 modulate the BOLD variation [52] but was not evaluated in this study. Altogether, extreme care
265 should be taken to maintain normal and stable physiological conditions while performing rs-fMRI.

266 *4.4. Impact of anesthetics on brain connectivity*

267 Our proposed pipeline using anesthetics extracts connectivity matrices of brain rats with 25-
268 60 % significant connections (Fig. 2c), containing 42/51 (80 %) areas significantly connected with
269 at least one other area (Fig. 4). This range of 25 % to 60 % of significant connections is consistent
270 with density observations in the macaque monkey (up to 66 %, 29 areas), using a retrograde tracer
271 analysis [53], and in mice (up to 36 %, 213 areas), using an anterograde tracer [45]. By acquiring
272 good quality data and using robust methods, it seems therefore possible to observe fMRI graphs
273 in which most brain areas remain functionally active, even when the rats are anesthetized. The
274 few apparent not significantly connected areas (H, BF, BG, APir, pag) are located far from the
275 receive surface coil (decrease of FCS in function of distances from Bregma given in Appendix H)

276 and close to large vessels or cerebro-spinal fluid, two sources of noise. The lower signal to noise
277 ratios for these areas could contribute to the absence of significant FCS in some areas such as
278 TeA or APir. The position of the left and right areas near the ears with potential distortions
279 (see Fig.B.8) can also add noise in these areas, but no correlations were observed between FCS
280 and medio-lateral locations of areas (Appendix H). The graph approach provides a global view
281 of the FC and characteristic patterns, with differences in the global organization of the brain
282 connectivity. This is in line with previous studies [4, 54, 3, 21, 6, 43] where the authors used seed
283 based analysis or independent component analysis (ICA). In this work, the impact of anesthetics
284 is visible at the regional level with communities (Fig. 5) partially related to networks such as
285 the default mode network (DMN) or the resting state network (RSN) [55, 43, 38]. Compared
286 to ICA approaches, which highlight the most orthogonal networks, the graph approach used in
287 this study rather seeks for all potential connections [56, 57]. Seed Based Analysis (SBA) also
288 promotes a limited number of connections due to the limited number of seeds. Graphs may be
289 seen as an SBA approach in which every region is a seed, with FCS giving the strength of the seed
290 (Fig. 4). In contrast to graph analysis, ICA or SBA approaches usually distinguish segregated
291 networks. Our results may not appear in agreement with these approaches, and a study using
292 the same data but with different analysis methods is required to conclude whether they lead to
293 similar or complementary conclusions concerning biological processes. The impact of Urethane
294 and Isoflurane on M1, S1 and CPU [21] is shown at the regional level, but also at an intermediate
295 level where balance of connections between cortico-cortical areas, cortico-subcortical areas, or
296 intrahemispheric and interhemispheric areas are modified depending on anesthetics. The study of
297 the effects of anaesthesia on bilateral connectivities in rodents is an active field of research [58],
298 with Medetomidine, which may reduce thalamocortical transmission [35] (Fig. 6, Tab. H.3 also
299 observed for Isoflurane in this study), but also bilateral connectivity [3, 58] (not observed here),
300 and Urethane, which may decrease the strength of bilateral connections [4, 21] (Fig. 6, Tab. H.3 in
301 this study) or even induce fluctuating connectivity states with periods on the order of a few minutes
302 to tens of minutes as reported in [59]. The influence of anaesthetic dose, rodent strain, animal
303 state and details of the analysis method on bilateral connectivity under anaesthesia requires further
304 investigation. Concerning these observations, our results are consistent with literature. However,
305 the different communities extracted with our method are not easily comparable with those obtained
306 with commonly used GSR or ICA. One could expect that our method would show communities
307 comparable to previously reported functional networks such as DMN (including ACC, RSC, and
308 Tea⁴) with stability observed across different anesthetics regimes [38]. Here, we observe that
309 there might be connections between ICA-reported networks. For example, ACC is part of the
310 DMN. It is also known to be involved in several processes such as the balanced between behaviors,
311 autonomous functions or nociception, and known to have a lot of connections with other areas
312 including sensory and motor areas [60, 61, 62]. ACC, as defined in our study, can therefore be
313 involved in different networks. Some comparisons between graph-based analyses and the effect of
314 GSR and ICA are given in [44], but it would be of interest to perform an entire study on the same
315 dataset to compare and enhance the complementarities of the different methods.

316 4.5. Main limitations

317 To overcome the limited brain coverage (10 mm that excluded the cerebellum and the olfactory
318 bulb), simultaneous multislice MRI should be developed at the preclinical level. The number of

⁴with prefrontal cortex area (PFC) not included in the study because this area was not available in several recordings

319 animals per group is limited ($n = 6$ or 7) and some groups exhibit heterogeneity. Main findings
320 are however related to all live animals ($n = 34$) and the impact of physiological variations was
321 carefully analyzed. The anesthetic dose in this study were standard ones but not optimal ones
322 related to anesthesia depth, leading to comparisons between drugs that should be mitigated. It is
323 indeed expected that the anesthetic dose also leads to different functional connectivity patterns, as
324 observed with isoflurane [14, 3, 44, 21], and should be evaluated in other studies in association to
325 the search of an optimal dose. Besides, further studies are required to account for the contribution
326 of the metabolic effects such as oxygen and glucose consumption and electrical activity [63, 64, 36].
327 Lastly, nothing can be interpreted from the remaining 20 % of the areas that are not significantly
328 connected.

329 5. Conclusions

330 In summary, this study introduces a methodological approach to evaluate the influence of
331 different anesthetics on rats during anesthesia. Using a rigorous mathematical framework based
332 on wavelets-based spectral filtering, we have shown that systemic variables and the baseline CBF,
333 in the range evaluated in this study, have no influence on the slow fluctuations of BOLD signals
334 and on FC. Moreover, most brain areas remained functionally active under the anesthetics used in
335 this study with density of the graphs in the range between 25 % to 60 %. This demonstrated, we
336 have proposed measures that highlight the influence of the different anesthetics on FC, at the level
337 of brain areas or between them. Future work could use the proposed methodological framework
338 with increased populations, adjusted anesthetics concentrations or refined spectral bands to better
339 tune the effects of anesthetics on the whole brain, on functional connectivities or on specific target
340 areas.

341 Acknowledgments

342 The authors want to thank the reviewers for their detailed comments and suggestions that have
343 improved the presentation of this work. The authors are very grateful to Sarah E. Morgan for her
344 careful and meticulous reading of the paper.

345 Funding

346 The MRI facility IRMaGe is partly funded by the French program *Investissement d'Avenir* run
347 by the French National Research Agency, grant *Infrastructure d'avenir en Biologie Santé* [ANR-
348 11-INBS-0006]. This project was partly funded by NeuroCoG IDEX UGA in the framework of the
349 *Investissements d'avenir* program [ANR-15-IDEX-02].

350 Competing Interests

351 The authors have no conflict of interests.

352 Author contributions

353 Design research: ELB, SA, GJPCB / Performed research: TH, NC, MF, VC / Contributed
354 analytic tools : GJPCB, SA, MF, VC, CDM / Analyzed data : GJPCB, ELB, SA / Wrote the
355 paper: GJPCB, ELB, SA.

356 References

- 357 [1] L. Chen, A. Mishra, A. T. Newton, V. L. Morgan, E. A. Stringer, B. P. Rogers, J. C.
358 Gore, Fine-scale functional connectivity in somatosensory cortex revealed by high-resolution
359 fMRI, *Magn. Reson. Imaging* 29 (2011) 1330–1337. URL: [https://doi.org/10.1016/j.
360 mri.2011.08.001](https://doi.org/10.1016/j.mri.2011.08.001).
- 361 [2] N. Zhang, P. Rane, W. Huang, Z. Liang, D. Kennedy, J. A. Frazier, J. King, Mapping
362 resting-state brain networks in conscious animals, *J. Neurosci. methods* 189 (2010) 186–196.
363 URL: <https://doi.org/10.1016/j.jneumeth.2010.04.001>.
- 364 [3] E. Jonckers, J. Van Audekerke, G. De Visscher, A. Van der Linden, M. Verhoye, Functional
365 connectivity fMRI of the rodent brain: comparison of functional connectivity networks in rat
366 and mouse, *PLoS One* 6 (2011) e18876. URL: [https://doi.org/10.1371/journal.pone.
367 0018876](https://doi.org/10.1371/journal.pone.0018876).
- 368 [4] J. Grandjean, A. Schroeter, I. Batata, M. Rudin, Optimization of anesthesia protocol for
369 resting-state fMRI in mice based on differential effects of anesthetics on functional connec-
370 tivity patterns, *NeuroImage* 102 (2014) 838 – 847. URL: [https://doi.org/10.1016/j.
371 neuroimage.2014.08.043](https://doi.org/10.1016/j.neuroimage.2014.08.043).
- 372 [5] R. G. Bettinardi, N. Tort-Colet, M. Ruiz-Mejias, M. V. Sanchez-Vives, G. Deco, Gradual
373 emergence of spontaneous correlated brain activity during fading of general anesthesia in
374 rats: Evidences from fMRI and local field potentials, *NeuroImage* 114 (2015) 185–198. URL:
375 <https://doi.org/10.1016/j.neuroimage.2015.03.037>.
- 376 [6] J. Paasonen, P. Stenroos, R. A. Salo, V. Kiviniemi, O. Gröhn, Functional connectivity under
377 six anesthesia protocols and the awake condition in rat brain, *NeuroImage* 172 (2018) 9–20.
378 URL: <https://doi.org/10.1016/j.neuroimage.2018.01.014>.
- 379 [7] J. A. King, T. S. Garelick, M. E. Brevard, W. Chen, T. L. Messenger, T. Q. Duong, C. F.
380 Ferris, Procedure for minimizing stress for fMRI studies in conscious rats, *J. Neurosci.
381 methods* 148 (2005) 154–160. URL: <https://doi.org/10.1016/j.jneumeth.2005.04.011>.
- 382 [8] K. S. Hendrich, P. M. Kochanek, J. A. Melick, J. K. Schiding, K. D. Statler, D. S. Williams,
383 D. W. Marion, C. Ho, Cerebral perfusion during anesthesia with fentanyl, isoflurane, or
384 pentobarbital in normal rats studied by arterial spin-labeled MRI, *Magn. Reson. Med.* 46
385 (2001) 202–206. URL: <https://doi.org/10.1002/mrm.1178>.
- 386 [9] P. J. Drew, A. Y. Shih, D. Kleinfeld, Fluctuating and sensory-induced vasodynamics in
387 rodent cortex extend arteriole capacity, *Proc. Natl. Acad. Sci. U. S. A.* 108 (2011) 8473–
388 8478. URL: <https://doi.org/10.1073/pnas.1100428108>.
- 389 [10] A. Schroeter, F. Schlegel, A. Seuwen, J. Grandjean, M. Rudin, Specificity of stimulus-evoked
390 fMRI responses in the mouse: the influence of systemic physiological changes associated with
391 innocuous stimulation under four different anesthetics, *NeuroImage* 94 (2014) 372–384. URL:
392 <https://doi.org/10.1016/j.neuroimage.2014.01.046>.
- 393 [11] F. Schlegel, A. Schroeter, M. Rudin, The hemodynamic response to somatosensory stimula-
394 tion in mice depends on the anesthetic used: implications on analysis of mouse fMRI data,

- 395 NeuroImage 116 (2015) 40–49. URL: <https://doi.org/10.1016/j.neuroimage.2015.05.013>.
396
- 397 [12] B. Biswal, F. Zerrin Yetkin, V. M. Haughton, J. S. Hyde, Functional connectivity in the
398 motor cortex of resting human brain using echo-planar MRI, *Magn. Reson. Med.* 34 (1995)
399 537–541. URL: <https://doi.org/10.1002/mrm.1910340409>.
- 400 [13] D. Kalthoff, J. U. Seehafer, C. Po, D. Wiedermann, M. Hoehn, Functional connectivity in
401 the rat at 11.7 T: Impact of physiological noise in resting state fMRI, *NeuroImage* 54 (2011)
402 2828–2839. URL: <https://doi.org/10.1002/nbm.1815>.
- 403 [14] K. A. Williams, M. Magnuson, W. Majeed, S. M. LaConte, S. J. Peltier, X. Hu, S. D.
404 Keilholz, Comparison of α -chloralose, medetomidine and isoflurane anesthesia for functional
405 connectivity mapping in the rat, *Magn. Reson. Imaging* 28 (2010) 995–1003. URL: <https://doi.org/10.1016/j.mri.2010.03.007>.
406
- 407 [15] M. A. Franceschini, H. Radhakrishnan, K. Thakur, W. Wu, S. Ruvinskaya, S. Carp, D. A.
408 Boas, The effect of different anesthetics on neurovascular coupling, *NeuroImage* 51 (2010)
409 1367–1377. URL: <https://doi.org/10.1016/j.neuroimage.2010.03.060>.
- 410 [16] G. J. Thompson, W.-J. Pan, J. C. Billings, J. K. Grooms, S. Shakil, D. Jaeger, S. D. Keilholz,
411 Phase-amplitude coupling and infraslow (< 1 hz) frequencies in the rat brain: relationship to
412 resting state fMRI, *Front. Integr. Neurosci.* 8 (2014) 41. URL: <https://doi.org/10.3389/fnint.2014.00041>.
413
- 414 [17] J. Cirone, T. W. Rosahl, D. S. Reynolds, R. J. Newman, G. F. O’meara, P. H. Hutson, K. A.
415 Wafford, γ -aminobutyric acid type a receptor $\beta 2$ subunit mediates the hypothermic effect of
416 etomidate in mice, *Anesthesiology* 100 (2004) 1438–1445. URL: <https://anesthesiology.pubs.asahq.org/article.aspx?articleid=1942784>.
417
- 418 [18] E. R. Cohen, K. Ugurbil, S.-G. Kim, Effect of basal conditions on the magnitude and dynam-
419 ics of the blood oxygenation level-dependent fMRI response, *J. Cereb. Blood Flow Metab.*
420 22 (2002) 1042–1053. URL: <https://doi.org/10.1097/00004647-200209000-00002>.
- 421 [19] M. M. Petrinovic, G. Hankov, A. Schroeter, A. Bruns, M. Rudin, M. von Kienlin, B. Kün-
422 necke, T. Mueggler, A novel anesthesia regime enables neurofunctional studies and imaging
423 genetics across mouse strains, *Sci. Rep.* 6 (2016) 2045–2322. URL: <https://doi.org/10.1038/srep24523>.
424
- 425 [20] K. Jann, D. G. Gee, E. Kilroy, S. Schwab, R. X. Smith, T. D. Cannon, D. J. Wang, Functional
426 connectivity in BOLD and CBF data: similarity and reliability of resting brain networks,
427 *NeuroImage* 106 (2015) 111–122. URL: <https://doi.org/10.1016/j.neuroimage.2014.11.028>.
428
- 429 [21] E. Jonckers, R. Delgado y Palacios, D. Shah, C. Guglielmetti, M. Verhoye, A. Linden,
430 Different anesthesia regimes modulate the functional connectivity outcome in mice, *Magn.*
431 *Reson. Med.* 72 (2014) 1103–1112. URL: <https://doi.org/10.1002/mrm.24990>.
- 432 [22] C. Kilkenny, W. J. Browne, I. C. Cuthill, M. Emerson, D. G. Altman, Improving
433 bioscience research reporting: The ARRIVE guidelines for reporting animal research,

- 434 PLOS Biology 8 (2010) 1–5. URL: <https://doi.org/10.1371/journal.pbio.1000412>.
435 doi:10.1371/journal.pbio.1000412.
- 436 [23] L. Hirschler, C. S. Debacker, J. Voiron, S. Köhler, J. M. Warnking, E. L. Barbier, Interpulse
437 phase corrections for unbalanced pseudo-continuous arterial spin labeling at high magnetic
438 field, *Magn. Reson. Med.* 79 (2018) 1314–1324. URL: [https://doi.org/10.1002/mrm.](https://doi.org/10.1002/mrm.26767)
439 26767.
- 440 [24] P. A. Valdes Hernandez, A. Sumiyoshi, H. Nonaka, R. Haga, E. Aubert Vasquez, T. Ogawa,
441 Y. Iturria Medina, J. J. Riera, R. Kawashima, An in vivo MRI template set for morphometry,
442 tissue segmentation, and fMRI localization in rats, *Front. Neuroinf.* 5 (2011) 26. URL:
443 <https://doi.org/10.3389/fninf.2011.00026>.
- 444 [25] E. A. Papp, T. B. Leergaard, E. Calabrese, G. A. Johnson, J. G. Bjaalie, Waxholm space
445 atlas of the Sprague Dawley rat brain, *NeuroImage* 97 (2014) 374–386. URL: [https://doi.](https://doi.org/10.1016/j.neuroimage.2014.04.001)
446 [org/10.1016/j.neuroimage.2014.04.001](https://doi.org/10.1016/j.neuroimage.2014.04.001).
- 447 [26] B. Whitcher, P. Guttorp, D. B. Percival, Wavelet analysis of covariance with application to
448 atmospheric time series, *Journal of Geophysical Research: Atmospheres* 105 (2000) 14941–
449 14962. URL: <https://doi.org/10.1029/2000JD900110>.
- 450 [27] S. Achard, R. Salvador, B. Whitcher, J. Suckling, E. Bullmore, A resilient, low-frequency,
451 small-world human brain functional network with highly connected association cortical hubs,
452 *J. Neurosci.* 26 (2006) 63–72. URL: <https://doi.org/10.1523/JNEUROSCI.3874-05.2006>.
- 453 [28] X. Liu, R. Li, Z. Yang, A. G. Hudetz, S.-J. Li, Differential effect of isoflurane, medetomidine,
454 and urethane on bold responses to acute levo-tetrahydropalmatine in the rat, *Magn. Reson.*
455 *Med.* 68 (2012) 552–559. URL: <https://doi.org/10.1002/mrm.23243>.
- 456 [29] P. Ganjoo, N. E. Farber, A. Hudetz, J. J. Smith, E. Samso, J. P. Kampine, W. T.
457 Schmeling, In vivo effects of dexmedetomidine on laser-doppler flow and pial arte-
458 riolar diameter, *Anesthesiology* 88 (1998) 429–439. URL: [https://doi.org/10.1097/](https://doi.org/10.1097/0000542-199802000-00022)
459 [0000542-199802000-00022](https://doi.org/10.1097/0000542-199802000-00022).
- 460 [30] R. Weber, P. Ramos-Cabrera, D. Wiedermann, N. van Camp, M. Hoehn, A fully noninvasive
461 and robust experimental protocol for longitudinal fMRI studies in the rat, *NeuroImage* 29
462 (2006) 1303–1310. URL: <https://doi.org/10.1016/j.neuroimage.2005.08.028>.
- 463 [31] X. Liang, Q. Zou, Y. He, Y. Yang, Coupling of functional connectivity and regional cere-
464 bral blood flow reveals a physiological basis for network hubs of the human brain, *Proc.*
465 *Natl. Acad. Sci. U. S. A.* 110 (2013) 1929–1934. URL: [https://doi.org/10.1073/pnas.](https://doi.org/10.1073/pnas.1214900110)
466 [1214900110](https://doi.org/10.1073/pnas.1214900110).
- 467 [32] A. Barrat, M. Barthelemy, R. Pastor-Satorras, A. Vespignani, The architecture of complex
468 weighted networks, *Proc. Natl. Acad. Sci. U. S. A.* 101 (2004) 3747–3752. URL: [https://](https://doi.org/10.1073/pnas.0400087101)
469 doi.org/10.1073/pnas.0400087101.
- 470 [33] M. Rubinov, O. Sporns, Complex network measures of brain connectivity: uses and
471 interpretations, *NeuroImage* 52 (2010) 1059–1069. URL: [https://doi.org/10.1016/j.](https://doi.org/10.1016/j.neuroimage.2009.10.003)
472 [neuroimage.2009.10.003](https://doi.org/10.1016/j.neuroimage.2009.10.003).

- 473 [34] D. De Wildt, F. Hillen, A. Rauws, B. Sangster, Etomidate-anaesthesia, with and without
474 fentanyl, compared with urethane-anaesthesia in the rat, *Br. J. Pharmacol.* 79 (1983) 461–
475 469. URL: <https://doi.org/10.1111/j.1476-5381.1983.tb11019.x>.
- 476 [35] M. D. Sinclair, A review of the physiological effects of α 2-agonists related to the clinical
477 use of medetomidine in small animal practice, *Can. Vet. J.* 44 (2003) 885. URL: <https://www.ncbi.nlm.nih.gov/pmc/articles/PMC385445/>.
- 479 [36] K. Masamoto, I. Kanno, Anesthesia and the quantitative evaluation of neurovascular cou-
480 pling, *J. Cereb. Blood Flow Metab.* 32 (2012) 1233–1247. URL: <https://doi.org/10.1038/jcbfm.2012.50>.
- 482 [37] C.-G. Yan, B. Cheung, C. Kelly, S. Colcombe, R. C. Craddock, A. Di Martino, Q. Li, X.-N.
483 Zuo, F. X. Castellanos, M. P. Milham, A comprehensive assessment of regional variation
484 in the impact of head micromovements on functional connectomics, *Neuroimage* 76 (2013)
485 183–201. URL: <https://doi.org/10.1016/j.neuroimage.2013.03.004>.
- 486 [38] J. Grandjean, C. Canella, C. Anckaerts, G. Ayrancı, S. Bougacha, T. Bienert, D. Buehlmann,
487 L. Coletta, D. Gallino, N. Gass, et al., Common functional networks in the mouse brain
488 revealed by multi-centre resting-state fMRI analysis, *NeuroImage* 205 (2020) 116278. URL:
489 <https://doi.org/10.1016/j.neuroimage.2019.116278>.
- 490 [39] K. Murphy, M. D. Fox, Towards a consensus regarding global signal regression for resting
491 state functional connectivity MRI, *NeuroImage* 154 (2017) 169–173. URL: <https://doi.org/10.1016/j.neuroimage.2016.11.052>.
- 493 [40] D. V. D’Souza, E. Jonckers, A. Bruns, B. Künnecke, M. von Kienlin, A. Van der Linden,
494 T. Mueggler, M. Verhoye, Preserved modular network organization in the sedated rat brain,
495 *PLoS One* 9 (2014) e106156. URL: <https://doi.org/10.1371/journal.pone.0106156>.
- 496 [41] N. Gass, A. J. Schwarz, A. Sartorius, E. Schenker, C. Risterucci, M. Spedding, L. Zheng,
497 A. Meyer-Lindenberg, W. Weber-Fahr, Sub-anesthetic ketamine modulates intrinsic BOLD
498 connectivity within the hippocampal-prefrontal circuit in the rat, *Neuropsychopharmacology*
499 39 (2014) 895. URL: <https://doi.org/10.1038/npp.2013.290>.
- 500 [42] A. Liska, A. Galbusera, A. J. Schwarz, A. Gozzi, Functional connectivity hubs of the mouse
501 brain, *NeuroImage* 115 (2015) 281–291. URL: <https://doi.org/10.1016/j.neuroimage.2015.04.033>.
- 503 [43] F. Sforazzini, A. J. Schwarz, A. Galbusera, A. Bifone, A. Gozzi, Distributed BOLD and
504 CBV-weighted resting-state networks in the mouse brain, *NeuroImage* 87 (2014) 403–415.
505 URL: <https://doi.org/10.1016/j.neuroimage.2013.09.050>.
- 506 [44] X. Liu, X.-H. Zhu, Y. Zhang, W. Chen, The change of functional connectivity specificity
507 in rats under various anesthesia levels and its neural origin, *Brain topography* 26 (2013)
508 363–377. URL: <https://doi.org/10.1007/s10548-012-0267-5>.
- 509 [45] S. W. Oh, J. A. Harris, L. Ng, B. Winslow, N. Cain, S. Mihalas, Q. Wang, C. Lau, L. Kuan,
510 A. M. Henry, et al., A mesoscale connectome of the mouse brain, *Nature* 508 (2014) 207.
511 URL: <https://doi.org/10.1038/nature13186>.

- 512 [46] A. Zalesky, A. Fornito, E. Bullmore, On the use of correlation as a measure of network connec-
513 tivity, *NeuroImage* 60 (2012) 2096–2106. URL: [https://doi.org/10.1016/j.neuroimage.](https://doi.org/10.1016/j.neuroimage.2012.02.001)
514 2012.02.001.
- 515 [47] E. V. Golanov, S. Yamamoto, D. J. Reis, Spontaneous waves of cerebral blood flow
516 associated with a pattern of electrocortical activity, *American Journal of Physiology-*
517 *Regulatory, Integrative and Comparative Physiology* 266 (1994) R204–R214. URL: [https:](https://doi.org/10.1038/npp.2013.290)
518 [//doi.org/10.1038/npp.2013.290](https://doi.org/10.1038/npp.2013.290).
- 519 [48] C. Mateo, P. M. Knutsen, P. S. Tsai, A. Y. Shih, D. Kleinfeld, Entrainment of arteriole
520 vasomotor fluctuations by neural activity is a basis of blood-oxygenation-level-dependent
521 “resting-state” connectivity, *Neuron* 96 (2017) 936–948. URL: [https://doi.org/10.1016/](https://doi.org/10.1016/j.neuron.2017.10.012)
522 [j.neuron.2017.10.012](https://doi.org/10.1016/j.neuron.2017.10.012).
- 523 [49] T. Akata, General anesthetics and vascular smooth muscle direct actions of general anes-
524 thetics on cellular mechanisms regulating vascular tone, *Anesthesiology* 106 (2007) 365–391.
525 URL: <https://doi.org/10.1097/00000542-200702000-00026>.
- 526 [50] A. Devor, P. Tian, N. Nishimura, I. C. Teng, E. M. Hillman, S. Narayanan, I. Ulbert, D. A.
527 Boas, D. Kleinfeld, A. M. Dale, Suppressed neuronal activity and concurrent arteriolar
528 vasoconstriction may explain negative blood oxygenation level-dependent signal, *Journal of*
529 *Neuroscience* 27 (2007) 4452–4459. URL: [https://doi.org/10.1523/JNEUROSCI.0134-07.](https://doi.org/10.1523/JNEUROSCI.0134-07.2007)
530 2007.
- 531 [51] V. A. Maximilian, I. Prohovnik, J. Risberg, Cerebral hemodynamic response to mental
532 activation in normo-and hypercapnia., *Stroke* 11 (1980) 342–347. URL: [https://www.](https://www.ahajournals.org/doi/pdf/10.1161/01.str.11.4.342)
533 [ahajournals.org/doi/pdf/10.1161/01.str.11.4.342](https://www.ahajournals.org/doi/pdf/10.1161/01.str.11.4.342).
- 534 [52] A. G. Hudetz, R. J. Roman, D. R. Harder, Spontaneous flow oscillations in the cerebral
535 cortex during acute changes in mean arterial pressure, *J. Cereb. Blood Flow Metab.* 12
536 (1992) 491–499. URL: <https://doi.org/10.1038/jcbfm.1992.67>.
- 537 [53] N. T. Markov, M. Ercsey-Ravasz, D. C. Van Essen, K. Knoblauch, Z. Toroczkai, H. Kennedy,
538 Cortical high-density counterstream architectures, *Science* 342 (2013) 1238406. URL: [https:](https://doi.org/10.1126/science.1238406)
539 [//doi.org/10.1126/science.1238406](https://doi.org/10.1126/science.1238406).
- 540 [54] R. M. Hutchison, M. Hutchison, K. Y. Manning, R. S. Menon, S. Everling, Isoflurane induces
541 dose-dependent alterations in the cortical connectivity profiles and dynamic properties of
542 the brain’s functional architecture, *Human Brain Mapping* 35 (2014) 5754–5775. URL:
543 <https://doi.org/10.1002/hbm.22583>.
- 544 [55] H. Lu, Q. Zou, H. Gu, M. E. Raichle, E. A. Stein, Y. Yang, Rat brains also have a default
545 mode network, *Proc. Natl. Acad. Sci. U. S. A.* 109 (2012) 3979–3984. URL: [https://doi.](https://doi.org/10.1073/pnas.1200506109)
546 [org/10.1073/pnas.1200506109](https://doi.org/10.1073/pnas.1200506109).
- 547 [56] D. Ribeiro de Paula, E. Ziegler, P. M. Abeyasinghe, T. K. Das, C. Cavaliere, M. Aiello,
548 L. Heine, C. Di Perri, A. Demertzi, Q. Noirhomme, et al., A method for independent
549 component graph analysis of resting-state fmri, *Brain and behavior* 7 (2017) e00626. URL:
550 <https://onlinelibrary.wiley.com/doi/pdf/10.1002/brb3.626>.

- 551 [57] H. Lv, Z. Wang, E. Tong, L. M. Williams, G. Zaharchuk, M. Zeineh, A. N. Goldstein-
552 Piekarski, T. M. Ball, C. Liao, M. Wintermark, Resting-state functional MRI: everything
553 that nonexperts have always wanted to know, *American Journal of Neuroradiology* 39 (2018)
554 1390–1399. URL: <https://doi.org/10.3174/ajnr.A5527>.
- 555 [58] F. A. Nasrallah, H.-C. Tay, K.-H. Chuang, Detection of functional connectivity in the
556 resting mouse brain, *NeuroImage* 86 (2014) 417–424. URL: [https://doi.org/10.1016/j.
557 neuroimage.2013.10.025](https://doi.org/10.1016/j.neuroimage.2013.10.025).
- 558 [59] E. Zhurakovskaya, J. Leikas, T. Pirttimäki, F. C. Mon, M. Gynther, R. Aliev, T. Rantamäki,
559 H. Tanila, M. M. Forsberg, O. Gröhn, et al., Sleep-state dependent alterations in brain
560 functional connectivity under urethane anesthesia in a rat model of early-stage parkinson’s
561 disease, *eNeuro* 6 (2019). URL: <https://doi.org/10.1523/ENEURO.0456-18.2019>.
- 562 [60] B. A. Vogt, M. W. Miller, Cortical connections between rat cingulate cortex and visual,
563 motor, and postsubicular cortices, *Journal of Comparative Neurology* 216 (1983) 192–210.
564 URL: <https://doi.org/10.1002/cne.902160207>.
- 565 [61] T. Paus, Primate anterior cingulate cortex: where motor control, drive and cognition in-
566 terface, *Nature reviews neuroscience* 2 (2001) 417–424. URL: [https://doi.org/10.1038/
567 35077500](https://doi.org/10.1038/35077500).
- 568 [62] B. A. Vogt, Pain and emotion interactions in subregions of the cingulate gyrus, *Nature*
569 *Reviews Neuroscience* 6 (2005) 533–544. URL: <https://dx.doi.org/10.1038%2Fnrn1704>.
- 570 [63] W. E. Hoffman, G. Edelman, E. Kochs, C. Werner, L. Segil, R. F. Albrecht, Cerebral
571 autoregulation in awake versus isoflurane-anesthetized rats., *Anesth. Analg.* 73 (1991) 753–
572 757. URL: <https://doi.org/10.1213/00000539-199112000-00013>.
- 573 [64] H. Sloan, V. Austin, A. Blamire, J. W. Schnupp, A. S. Lowe, K. Allers, P. M. Matthews,
574 N. R. Sibson, Regional differences in neurovascular coupling in rat brain as determined by
575 fMRI and electrophysiology, *NeuroImage* 53 (2010) 399–411. URL: [https://doi.org/10.
576 1016/j.neuroimage.2010.07.014](https://doi.org/10.1016/j.neuroimage.2010.07.014).
- 577 [65] K. Baek, W. H. Shim, J. Jeong, H. Radhakrishnan, B. R. Rosen, D. Boas, M. Franceschini,
578 B. B. Biswal, Y. R. Kim, Layer-specific interhemispheric functional connectivity in the
579 somatosensory cortex of rats: resting state electrophysiology and fMRI studies, *Brain Struct.*
580 *Funct.* 221 (2016) 2801–2815. URL: <https://doi.org/10.1007/s00429-015-1073-0>.
- 581 [66] D. N. Guilfoyle, S. V. Gerum, J. L. Sanchez, A. Balla, H. Sershen, D. C. Javitt, M. J.
582 Hoptman, Functional connectivity fMRI in mouse brain at 7 T using isoflurane, *J. Neurosci.*
583 *methods* 214 (2013) 144–148. URL: <https://doi.org/10.1016/j.jneumeth.2013.01.019>.
- 584 [67] H. Lu, Y. Zuo, H. Gu, J. A. Waltz, W. Zhan, C. A. Scholl, W. Rea, Y. Yang, E. A. Stein,
585 Synchronized delta oscillations correlate with the resting-state functional MRI signal, *Proc.*
586 *Natl. Acad. Sci. U. S. A.* 104 (2007) 18265–18269. URL: [https://doi.org/10.1073/pnas.
587 0705791104](https://doi.org/10.1073/pnas.0705791104).
- 588 [68] W. H. Shim, K. Baek, J. K. Kim, Y. Chae, J.-Y. Suh, B. R. Rosen, J. Jeong, Y. R. Kim,
589 Frequency distribution of causal connectivity in rat sensorimotor network: resting-state fMRI

- 590 analyses, *J. Neurophysiol.* 109 (2012) 238–248. URL: [https://doi.org/10.1152/jn.00332.](https://doi.org/10.1152/jn.00332.2012)
591 2012.
- 592 [69] S. Ogawa, T. M. Lee, A. R. Kay, D. W. Tank, Brain magnetic resonance imaging with
593 contrast dependent on blood oxygenation, *Proc. Natl. Acad. Sci. U. S. A.* 87 (1990) 9868–
594 9872. URL: <https://doi.org/10.1073/pnas.87.24.9868>.
- 595 [70] L. Ciobanu, O. Reynaud, L. Uhrig, B. Jarraya, D. Le Bihan, Effects of anesthetic agents on
596 brain blood oxygenation level revealed with ultra-high field MRI, *PloS One* 7 (2012) e32645.
597 URL: <https://doi.org/10.1371/journal.pone.0032645>.
- 598 [71] K. C. Chan, S.-J. Fan, R. W. Chan, J. S. Cheng, I. Y. Zhou, E. X. Wu, In vivo visuo-
599 topic brain mapping with manganese-enhanced MRI and resting-state functional connectiv-
600 ity MRI, *NeuroImage* 90 (2014) 235–245. URL: [https://doi.org/10.1016/j.neuroimage.](https://doi.org/10.1016/j.neuroimage.2013.12.056)
601 2013.12.056.
- 602 [72] D. Kalthoff, C. Po, D. Wiedermann, M. Hoehn, Reliability and spatial specificity of rat
603 brain sensorimotor functional connectivity networks are superior under sedation compared
604 with general anesthesia, *NMR in Biomedicine* 26 (2013) 638–650. URL: [https://doi.org/](https://doi.org/10.1002/nbm.2908)
605 10.1002/nbm.2908.
- 606 [73] Z. Liang, T. Li, J. King, N. Zhang, Mapping thalamocortical networks in rat brain using
607 resting-state functional connectivity, *NeuroImage* 83 (2013) 237–244. URL: [https://doi.](https://doi.org/10.1371/journal.pone.0032766)
608 [org/10.1371/journal.pone.0032766](https://doi.org/10.1371/journal.pone.0032766).
- 609 [74] Z. Liang, X. Liu, N. Zhang, Dynamic resting state functional connectivity in awake and
610 anesthetized rodents, *NeuroImage* 104 (2015) 89–99. URL: [https://doi.org/10.1016/j.](https://doi.org/10.1016/j.neuroimage.2014.10.013)
611 [neuroimage.2014.10.013](https://doi.org/10.1016/j.neuroimage.2014.10.013).
- 612 [75] M. Magnuson, W. Majeed, S. D. Keilholz, Functional connectivity in blood oxygenation level-
613 dependent and cerebral blood volume-weighted resting state functional magnetic resonance
614 imaging in the rat brain, *J. Magn. Reson. Imaging* 32 (2010) 584–592. URL: [https://doi.](https://doi.org/10.1002/jmri.22295)
615 [org/10.1002/jmri.22295](https://doi.org/10.1002/jmri.22295).
- 616 [76] M. E. Magnuson, G. J. Thompson, W.-J. Pan, S. D. Keilholz, Time-dependent effects
617 of isoflurane and dexmedetomidine on functional connectivity, spectral characteristics, and
618 spatial distribution of spontaneous bold fluctuations, *NMR in biomedicine* 27 (2014) 291–303.
619 URL: <https://doi.org/10.1002/nbm.3062>.
- 620 [77] K. Masamoto, M. Fukuda, A. Vazquez, S.-G. Kim, Dose-dependent effect of isoflurane on
621 neurovascular coupling in rat cerebral cortex, *European J. Neurosci.* 30 (2009) 242–250.
622 URL: <https://doi.org/10.1111/j.1460-9568.2009.06812.x>.
- 623 [78] W.-J. Pan, G. J. Thompson, M. E. Magnuson, D. Jaeger, S. Keilholz, Infralow LFP
624 correlates to resting-state fMRI BOLD signals, *NeuroImage* 74 (2013) 288–297. URL:
625 <https://doi.org/10.1016/j.neuroimage.2013.02.035>.
- 626 [79] K. Sicard, Q. Shen, M. E. Brevard, R. Sullivan, C. F. Ferris, J. A. King, T. Q. Duong,
627 Regional cerebral blood flow and BOLD responses in conscious and anesthetized rats under
628 basal and hypercapnic conditions: implications for functional MRI studies, *J. Cereb. Blood*

- 629 Flow Metab. 23 (2003) 472–481. URL: <https://doi.org/10.1097/01.WCB.0000054755.93668.20>.
- 630
- 631 [80] J. B. Smith, Z. Liang, G. D. Watson, K. D. Alloway, N. Zhang, Interhemispheric resting-state
632 functional connectivity of the claustrum in the awake and anesthetized states, *Brain Struct.*
633 *Funct.* 222 (2017) 2041–2058. URL: <https://doi.org/10.1007/s00429-016-1323-9>.
- 634 [81] J. M. Stafford, B. R. Jarrett, O. Miranda-Dominguez, B. D. Mills, N. Cain, S. Mihalas,
635 G. P. Lahvis, K. M. Lattal, S. H. Mitchell, S. V. David, et al., Large-scale topology and the
636 default mode network in the mouse connectome, *Proc. Natl. Acad. Sci. U. S. A.* 111 (2014)
637 18745–18750. URL: <https://doi.org/10.1073/pnas.1404346111>.
- 638 [82] A. E. Mechling, N. S. Hübner, H.-L. Lee, J. Hennig, D. von Elverfeldt, L.-A. Harsan, Fine-
639 grained mapping of mouse brain functional connectivity with resting-state fMRI, *NeuroImage*
640 96 (2014) 203–215. URL: <https://doi.org/10.1016/j.neuroimage.2014.03.078>.
- 641 [83] C. P. Pawela, B. B. Biswal, Y. R. Cho, D. S. Kao, R. Li, S. R. Jones, M. L. Schulte, H. S.
642 Matloub, A. G. Hudetz, J. S. Hyde, Resting-state functional connectivity of the rat brain,
643 *Magn. Reson. Med.* 59 (2008) 1021–1029. URL: <https://doi.org/10.1002/mrm.21524>.
- 644 [84] C. P. Pawela, B. B. Biswal, A. G. Hudetz, M. L. Schulte, R. Li, S. R. Jones, Y. R. Cho, H. S.
645 Matloub, J. S. Hyde, A protocol for use of medetomidine anesthesia in rats for extended stud-
646 ies using task-induced BOLD contrast and resting-state functional connectivity, *NeuroImage*
647 46 (2009) 1137–1147. URL: <https://doi.org/10.1016/j.neuroimage.2009.03.004>.
- 648 [85] A. J. Schwarz, N. Gass, A. Sartorius, L. Zheng, M. Spedding, E. Schenker, C. Ris-
649 terucci, A. Meyer-Lindenberg, W. Weber-Fahr, The low-frequency blood oxygenation
650 level-dependent functional connectivity signature of the hippocampal–prefrontal network
651 in the rat brain, *Neuroscience* 228 (2013) 243–258. URL: <https://doi.org/10.1016/j.neuroscience.2012.10.032>.
- 652
- 653 [86] V. Zerbi, J. Grandjean, M. Rudin, N. Wenderoth, Mapping the mouse brain with rs-fMRI:
654 an optimized pipeline for functional network identification, *NeuroImage* 123 (2015) 11–21.
655 URL: <https://doi.org/10.1016/j.neuroimage.2015.07.090>.
- 656 [87] W. M. Otte, K. van der Marel, K. P. Braun, R. M. Dijkhuizen, Effects of transient unilateral
657 functional brain disruption on global neural network status in rats: a methods paper, *Front.*
658 *Syst. Neurosci.* 8 (2014) 40. URL: <https://doi.org/10.3389/fnsys.2014.00040>.
- 659 [88] X. Liu, S. Pillay, R. Li, J. A. Vizuite, K. R. Pechman, K. M. Schmainda, A. G. Hudetz,
660 Multiphasic modification of intrinsic functional connectivity of the rat brain during increasing
661 levels of propofol, *NeuroImage* 83 (2013) 581–592. URL: <https://doi.org/10.1016/j.neuroimage.2013.07.003>.
- 662
- 663 [89] K. Wang, M. P. van Meer, K. van der Marel, A. van der Toorn, L. Xu, Y. Liu, M. A. Viergever,
664 T. Jiang, R. M. Dijkhuizen, Temporal scaling properties and spatial synchronization of
665 spontaneous blood oxygenation level-dependent (bold) signal fluctuations in rat sensorimotor
666 network at different levels of isoflurane anesthesia, *NMR Biomed.* 24 (2011) 61–67. URL:
667 <https://doi.org/10.1002/nbm.1556>.

- 668 [90] M. Rolland, C. Carcenac, P. Overton, M. Savasta, V. Coizet, Enhanced visual responses
669 in the superior colliculus and subthalamic nucleus in an animal model of parkinson's dis-
670 ease, *Neuroscience* 252 (2013) 277–288. URL: [https://doi.org/10.1016/j.neuroscience.](https://doi.org/10.1016/j.neuroscience.2013.07.047)
671 2013.07.047.
- 672 [91] J. Ashburner, G. Barnes, C. Chen, J. Daunizeau, G. Flandin, K. Friston, S. Kiebel, J. Kilner,
673 V. Litvak, R. Moran, et al., *SPM12 manual*, Wellcome Trust Centre for Neuroimaging, Lon-
674 don, UK (2014). URL: https://www.fil.ion.ucl.ac.uk/spm/doc/spm12_manual.pdf.
- 675 [92] J. D. Power, K. A. Barnes, A. Z. Snyder, B. L. Schlaggar, S. E. Petersen, Spurious but
676 systematic correlations in functional connectivity MRI networks arise from subject motion,
677 *Neuroimage* 59 (2012) 2142–2154. URL: [https://doi.org/10.1016/j.neuroimage.2011.](https://doi.org/10.1016/j.neuroimage.2011.10.018)
678 10.018.
- 679 [93] D. Alsop, J. Detre, X. e. a. Golay, Recommended implementation of arterial spin labeled
680 perfusion mri for clinical applications: A consensus of the ISMRM perfusion study group
681 and the european consortium for ASL in dementia, *Magn. Reson. Med.* 73 (2015) 102–116.
682 URL: <https://doi.org/10.1002/mrm.25197>.
- 683 [94] K. Gorgolewski, C. Burns, C. e. a. Madison, Nipype: A flexible, lightweight and extensible
684 neuroimaging data processing framework in python., *Front. Neuroinfo.* (2011) 5–13. URL:
685 <https://doi.org/10.3389/fninf.2011.00013>.
- 686 [95] G. Csardi, T. Nepusz, The igraph software package for complex network research, *Inter-*
687 *Journal Complex Systems* (2006) 1695. URL: <http://igraph.org>.
- 688 [96] A. Clauset, M. E. Newman, C. Moore, Finding community structure in very large net-
689 works, *Physical review E* 70 (2004) 066111. URL: [https://doi.org/10.1103/PhysRevE.](https://doi.org/10.1103/PhysRevE.70.066111)
690 70.066111.
- 691 [97] M. D. Greicius, B. Krasnow, A. L. Reiss, V. Menon, Functional connectivity in the
692 resting brain: A network analysis of the default mode hypothesis, *Proc. Natl. Acad.*
693 *Sci. U. S. A.* 100 (2003) 253–258. URL: <https://doi.org/10.1073/pnas.0135058100>.
694 [arXiv:http://www.pnas.org/content/100/1/253.full.pdf](http://www.pnas.org/content/100/1/253.full.pdf).
- 695 [98] Z. Ma, P. Perez, Z. Ma, Y. Liu, C. Hamilton, Z. Liang, N. Zhang, Functional atlas of the
696 awake rat brain: A neuroimaging study of rat brain specialization and integration, *NeuroIm-*
697 *age* (2016). URL: <https://doi.org/10.1016/j.neuroimage.2016.07.007>.
- 698 [99] H. E. Wang, C. G. Bénar, P. P. Quilichini, K. J. Friston, V. K. Jirsa, C. Bernard, A
699 systematic framework for functional connectivity measures, *Front. Neurosci.* 8 (2014) 405.
700 doi:<https://doi.org/10.3389/fnins.2014.00405>.
- 701 [100] B. J. Whitcher, Assessing nonstationary time series using wavelets, *Citeseer*,
702 1998. URL: [http://citeseerx.ist.psu.edu/viewdoc/download?doi=10.1.1.29.5644&](http://citeseerx.ist.psu.edu/viewdoc/download?doi=10.1.1.29.5644&rep=rep1&type=pdf)
703 [rep=rep1&type=pdf](http://citeseerx.ist.psu.edu/viewdoc/download?doi=10.1.1.29.5644&rep=rep1&type=pdf).

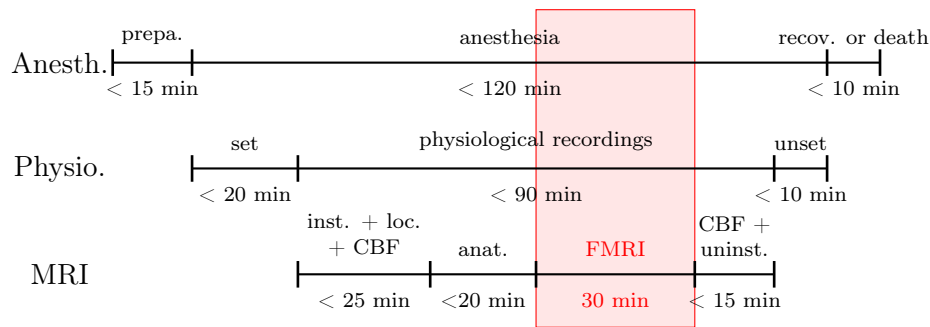


Figure B.7: Experimental protocol. Notations: Anesthesia (Anesth.), SV (Physio.), Magnetic resonance imaging (MRI), preparation of the animal (prepa.), installation of the animal in the scanner (inst.), position verification with a localizer sequence (loc.), cerebral perfusion sequence (CBF), anatomical sequence (anat.), rs-fMRI sequence (FMRI), uninstallation of the animal (uninst.), recovery or death of the animal (recov. or death)

704 Appendix A. Anesthetics used in rodents

705 A list of the anesthetics evaluated on rodents is given here with associated references:

- 706 - α -chloralose [65, 15, 66, 21, 67, 6, 68, 14],
- 707 - diazepam (benzodiazepine) [69],
- 708 - etomidate [19],
- 709 - fentanyl [8],
- 710 - halogeneous derivates [70, 71, 15, 4, 8, 63, 21, 72, 73, 74, 42, 44] [75, 76, 77, 69, 6, 78, 43, 79,
- 711 64, 80, 81, 16, 14],
- 712 - ketamine [5, 70, 41],
- 713 - medetomidine [5, 70, 40, 41, 4, 3, 13, 72, 55, 76, 82, 58, 6, 78, 83, 84, 85, 16, 14, 86],
- 714 - MPEP (mGluR5 antagonist 2-methyl-6-(phenylethynyl)-pyridine [64],
- 715 - pentobarbital [8, 87],
- 716 - propofol [4, 88, 6],
- 717 - urethane (carbamate) [4, 21, 69, 6].

718 Animals can also received curare (pancuronium bromide) infusion [44, 88, 83, 68, 86] to relax
 719 muscle and avoid movements or paralyzing agent (gallamine triethiodide) [43].

720 Elements on what is known about the effects on brain functions, neurons interactions, ionic
 721 channels affinities and physiological interactions can be found for example in [49].

722 Appendix B. Supplementary Materials

723 Appendix B.1. Experimental protocol

724 A scheme of the experimental setup used to record data from anesthetized rats is proposed
 725 Fig. B.7 and can be summarized as follows. For the anesthesia, a preparation of the animal is
 726 realized in an induction room. Anesthesia generally lasted less than 2 hours. At the end of the
 727 protocol the animal is kept alive for another study or euthanized, if in the Ure group or randomly
 728 assigned to the Dead group. For the systemic variables, also denoted SV, sensors are set and
 729 unset before and after the recordings. For magnetic resonance imaging, the animal is installed
 730 in the scanner and positions are verified with localizer sequences. A perfusion sequence and an
 731 anatomical sequence are acquired before the fMRI sequence which lasts 30 min. Then, another
 732 perfusion sequence (CBF) is acquired, followed by the uninstallation of the animal.

733 *Appendix B.2. Anesthesia*

734 At the beginning of the experiment, animals receive a gaseous mixture, composed of isoflurane
735 and a mixture of 80 % air and 20 % oxygen, inhaled through a funnel. A level of 5 % isoflurane is
736 given during 2 min followed by a level of 2 % during 10 minutes. During the animal preparation,
737 ears are filled with a mix of gel (ocry-gel) and wax, to limit air-related susceptibility artifacts in
738 the images. After this common induction, four anesthetics are evaluated:

739 - Isoflurane (Iso): the level of isoflurane is set to 1 % to be in a regime showing persistent
740 behavior of spontaneous BOLD fluctuations [89]. To evaluate the impact of strain, this anesthetic
741 was evaluated in both Long-Evans and Wistar rats.

742 - Etomidate (Eto) (B. Braun, Melsungen, Germany) : An administration in two stages is
743 performed with a bolus of 10 mg / kg / min (3 min) injected in association with isoflurane at 4%
744 during initiation, followed by a continuous intravenous infusion at 0.5 mg / kg / min.

745 - Medetomidine (Med) (Domitor, medetomidine hydrochloride; Orion Corporation, Espoo, Fin-
746 land): An administration in two stages is performed with a bolus of 0.24 mg/kg injected subcu-
747 taneously in association with isoflurane at 4% during initiation, followed by a continuous infusion
748 at 0.05 mg / kg / h.

749 - Urethane (Ure): A bolus of 1.25 g / kg is injected intraperitoneally. [90] The use of this
750 anesthesia is well regulated and rats are euthanized at the end of the experiment because of the
751 carcinogenic toxicity of this agent.

752 - A group of dead rats (Dead) was created by sacrificing 4 animals just before the experiment.

753 Overall, 6 groups were evaluated: Eto-L (n=7), Iso-L (n=6), Iso-W (n=7), Med-L (n=7), Ure-L
754 (n=7), Dead (n=4).

755 *Appendix B.3. Systemic variables*

756 Two devices are used to monitor and record systemic variables (SV):

757 - A MouseOx Pulse oximeter (STARR Life Sciences Corp., Oakmont, PA, USA) with a rat
758 sensor clipped on the right posterior paw of the animal. The system provides different measures:
759 the peripheral arterial oxygen saturation (SpO₂), the heart rate (heart rate). An error measure is
760 also recorded to validate the measures recorded by the device. Only SV samples recorded by the
761 oximeter and marked without errors are retained for the study;

762 - A SAI Trend (Small Animal Instruments Inc., Stony Brook, NY, USA) system is also used
763 to record the temperature (Temp) from a rectal probe and the respiratory rate (resp. rate) from
764 a small pneumatic pillow sensor. The error rate is computed as the ratio of the number of values
765 recorded with code different from 0 (no error) on the oximeter to 3600, the number of samples
766 during the whole rs-fMRI session. Clocks of the recording systems are verified at the beginning
767 and at the end of the recordings, to follow a universal clock, noted, and eventually corrected.
768 Measurements from the two systems are sampled at 1 Hz. No offline adjustments were necessary
769 with the 1 s precision. During the experiments a warm circulating water positioned below the
770 animal is regulated to maintain the body temperature to a target level of 37°C. Dead animals were
771 not monitored, not regulated, and were imaged one hour after sacrifice.

772 *Appendix B.4. MRI acquisitions*

773 Rats brains are scanned at 9.4 T with a volume transmit, 4-channel surface receive cross coil
774 configuration (Paravision 6.0.1, Bruker, Ettlingen, Germany). After an anatomical T2w scan,
775 cerebral blood flow (CBF) is mapped using pseudo continuous arterial spin labeling (pCASL;
776 labeling duration 3000 ms, post-labeling delay 300 ms; TR=3500 ms; TE=9.7 ms; 20 averages;
777 spin-echo 2D echo-planar readout with a spatial resolution 0.47 x 0.47 x 1.00 mm, gap 0.1 mm,

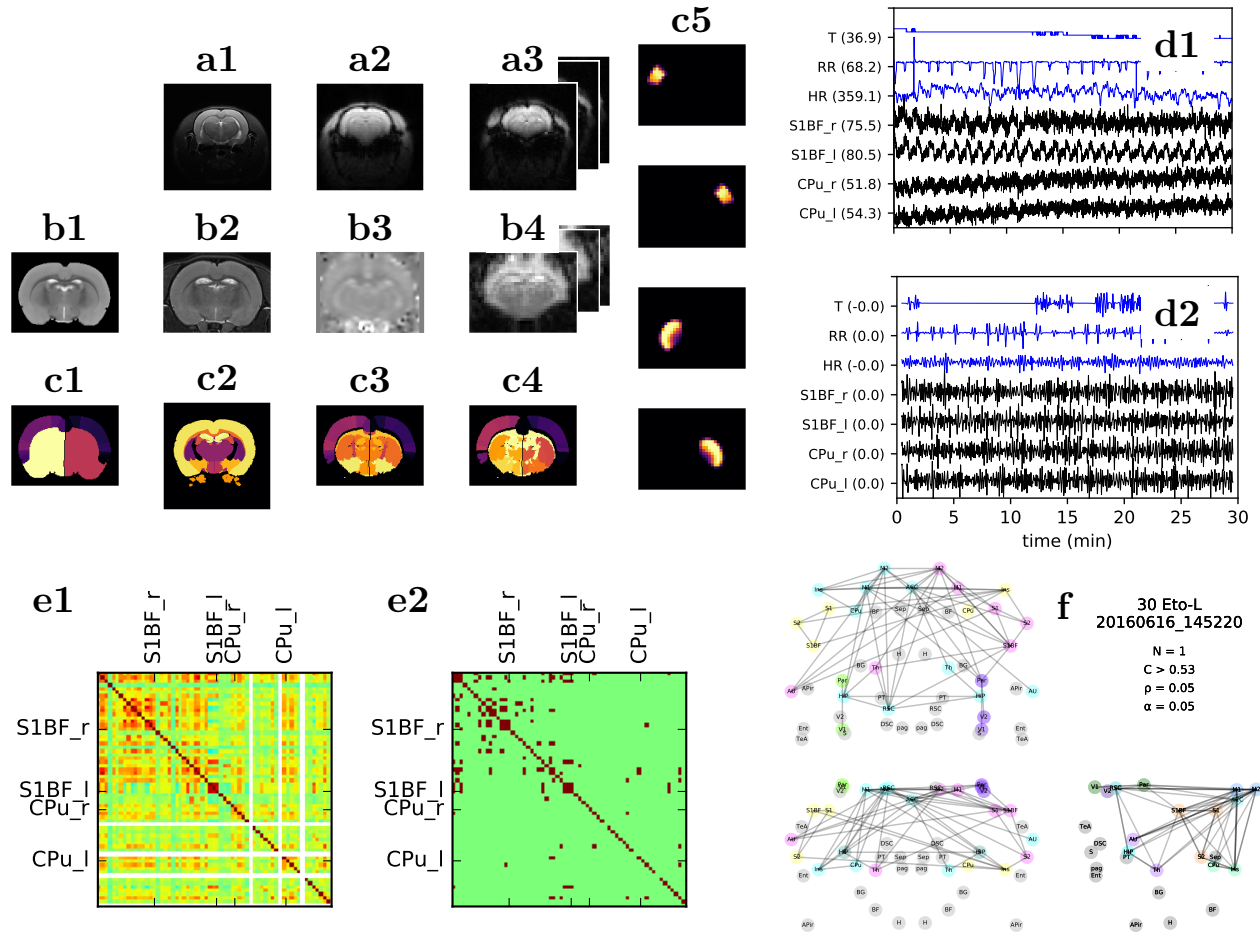
778 9 slices) following inter-pulse phase optimization as proposed in [23]. Then, resting state fMRI
779 (rs-fMRI) was performed with a single shot echo-planar imaging with parameters set to: TR/TE
780 = 500/20 ms, spatial resolution 0.47 x 0.47 x 1.00 mm, gap 0.1 mm, 9 slices, 3600 repetitions,
781 duration 30 min. The volume of interest stands between 0 and -10 mm with respect to bregma
782 and results in a volume of 64 x 64 x 9 voxels. Eventually, a second CBF map is acquired and
783 averaged with the first CBF acquisition to obtain a mean CBF during the rs-fMRI experiment.
784 Rats were strapped to the MRI insertion table with the head maintained with ear bars and a bite
785 bar to prevent movements.

786 *Appendix B.5. data processing*

787 An overview of the data processing is given in Fig. B.8 for one individual, from the MR
788 images to the graph representations of the brain activity and can be summarized as follows: fMRI
789 BOLD signals are first extracted on $N = 51$ brain areas from a home-made atlas (Appendix C)
790 based on published ones [24, 25] after normalization of anatomical images and co-registration of
791 fMRIs; Physiological and BOLD signals are motion corrected (Appendix E) and decomposed into
792 different frequency bands with wavelet transforms described in the main text (see also Appendix F);
793 Correlations are performed on these signals to evaluate FC.

794 *Appendix B.5.1. Atlas creation, co-registration and normalization of MRI*

795 The WHS atlas [25], focusing on subcortical areas is merged into the Tohoku atlas [24], focusing
796 on cortical areas, to obtain our own atlas containing both cortical and subcortical areas (see
797 Appendix C). All MRI recordings are aligned to the Tohoku template. Dimensions of voxels in
798 the different spaces are: in the Tohoku space, 0.125 mm \times 0.125 mm \times 0.125 mm (0.002 mm^3), 136
799 \times 102 \times 180 voxels; in the WHS space, 0.0391 mm \times 0.0391 mm \times 0.0391 mm, 512 by 1024 \times 512
800 voxels; for anatomical MRI, 0.117 mm \times 0.117 mm \times 0.8 mm, 256 \times 256 \times 27; for fMRI, 0.469 mm
801 \times 0.469 mm \times 1.1 mm. Dimensions of anatomical images and rs-fMRI are multiplied by 10 to
802 fit the dimension of the Tohoku atlas made to be compatible with algorithms of the Statistical
803 Parametric Mapping software (SPM12) [91] defined for human images. The origin is manually set
804 to match the origin of the Tohoku template i.e. to the bregma zero coordinate, at the apex of
805 the most forward crossing fibers of the anterior commissure. A segmentation of the tissue of the
806 anatomical image is computed and used to normalize the anatomical image to the Tohoku space.
807 rs-fMRIs are realigned and resliced to the first image of the fMRI sequence. The coregistration
808 variables are used to filter movements by analyzing framewise displacements [92] (Appendix E). A
809 coregistration of the fMRIs on the anatomical image is computed and applied to all fMRIs while
810 keeping the fMRI voxel size. For all these operations, a 4th degree B-spline interpolation is set.
811 More precisely, these operations are realized using SPM 12 [91] with adaptation of rodents volumes
812 to parameters of algorithms based on human volumes, following: 1 - change of origin to the Bregma
813 site and modification of a size of a factor of 10 for anatomical and fMRI volumes. (batch 'Reorient Images' with
814 scaling parameters set to 10), 2 - Normalization of anatomical images to template. (batch 'Old Segment' with
815 Grey matter, White matter and cerebro-Spinal Fluid in the native space and tissue probability maps taken from
816 Tohoku space. Gaussian per class [2 2 2 4] / Affine regularisation: average sized template, Warping regularisation:
817 1, warp frequency cutoff: 25, bias regularisation: light regularisation (0.001), bias FWHM 60 mm cutoff; sampling
818 distance: 3) 3 - Correction of acquisition offset and coregister fMRI volumes to the anatomical volume (batch
819 Realign: Estimate & Reslice / quality:0.9, separation: 4, smoothing (FWHM): 5, Num passes: register to first,
820 interpolation: 2nd Degree B-Spline, Wrapping: no wrap, weighting: 0 files, resliced images: mean image only,
821 interpolation: 4th degree B-spline, wrapping: no wrap, masking: mask images) (batch + Coregister: Estimate:
822 Objective function: Normalised mutual information, separation: [4 2], Tolerances: [0.02, 0.02, 0.02, 0.001, 0.001,



Notations: LR: left right axis; IS: inferior superior axis; PA: posterior anterior axis., T: Temp, RR: resp.rate, HR: heart rate.

Figure B.8: Overview of the data processing to obtain FC graphs between brain areas on one rat: a-b) image transformations with reference on the Tohoku anatomic template (b1): raw (a1) and normalized (b2) anatomical MRI, raw (a2) and norm. (b3) perfusion MRI, raw (a3) and norm. (b4) fMRI; c) Atlas construction with reference on the Tohoku anatomic template (b1): Tohoku atlas (c1), WHS atlas (c2), merged atlas (c3), with left and right labeling (c4), low resolution area weights (c5) from top to bottom S1BF l, S1BF r, CPu l, CPu r; d) SV and fMRI signals extraction and wavelet decomposition: raw signals (d1) extracted from (b3) and (c5) and wavelet decomposition cD4 (d2); e) correlation matrix (e1) and thresholded one (e2) at density $\rho = 5\%$; f) FC graph corresponding to (e2). In this graph, locations of nodes correspond to the centers of gravity of brain areas. Edges indicate the connectivity between two areas. The graph is projected on the three standard projections LR-IS, PA-IS, and PA-LR (LR: left right axis; IS: inferior superior axis; PA: posterior anterior axis).

823 0.001, 0.01, 0.01, 0.01, 0.001, 0.001, 0.001], Histogram smoothing fwhm: [7, 7], interp: 0, wrap: [0, 0, 0], mask:
824 0), 4 - Normalize fMRI images to template using transformation obtained in 2. (batch Old Normalise: Write /
825 Bounding box: [[nan, nan, nan], [nan, nan, nan]], Voxel sizes [1.25, 1.25, 1.25], Interpolation: 0, Wrapping: [0, 0,
826 0].) At the end of the process, all CBF and all rs-fMRI images are in a volume of dimension $36 \times$
827 27×21 , with voxel size $0.469 \times 0.469 \times 1.1$ mm (0.242 mm³), the same resolution of the original
828 fMRI but aligned and normalized to the Tohoku space.

829 *Appendix B.5.2. Cerebral blood flow maps*

830 CBF maps are obtained using homemade Matlab routines based on [93, 23]. CBF values and
831 rs-fMRI time courses are computed for each of the 51 areas of the atlas. If available, mean CBF
832 values are extracted by averaging the values obtained before and after the rs-fMRI acquisition:
833 $(\text{CBF}_{\text{before}} + \text{CBF}_{\text{after}}) / 2$.

834 *Appendix B.5.3. Signal extraction per area and wavelet decomposition*

835 The processing of fMRI images to extract signals from atlas areas is done with Python using the
836 Nipy package [94] and home-made algorithms. The signal of an area is computed as the weighted
837 summation of signals across all the voxels from that area (see Appendix D for details). rs-fMRI time
838 course of an area (raw signal), is decomposed with a maximal overlap discrete wavelet transform
839 (modwt) at different scales and Daubechies orthonormal compactly supported wavelets of length
840 $L=8$, using the wavedec package [27]. Details coefficients cD1 to cD7, and an approximation
841 coefficient cA7 that captures the polynomial trends contained in the signal are extracted. This
842 last is generally a source of noise in observations. The limits of the frequency band j is obtained
843 by dividing the sampling frequency (2 Hz), by 2^{j+1} and 2^j . In our study, j varies from 1 to 7
844 leading to discard details < 0.008 Hz where spectrums become flat (see Appendix F).

845 *Appendix B.5.4. Correlation of signals, graph creation and clustering*

846 The functional connectivity is obtained by computing the pairwise correlation C_{ij} between area
847 i and j of the BOLD signals filtered at different frequency bands [27] denoted x_i and x_j . It is given
848 by:

$$C(i, j) = \frac{\frac{1}{N} \sum_{k=1}^N x_{ci}(k) x_{cj}(k)}{\left(\frac{1}{N} \sum_{k=1}^N x_{ci}^2(k) \frac{1}{N} \sum_{k=1}^N x_{cj}^2(k)\right)^{1/2}} \quad (\text{B.1})$$

849 with x_{ci} the centered variable i. e. the variable with its sample mean subtracted $x_{ci} = x_i - \bar{x}_i$ for
850 area i over N temporal samples. Graphs are then obtained :

851 - by finding a threshold for which the number of retained correlation values over the total
852 number of possible connections represents the target density;

853 - by selecting areas as nodes and defining edges with correlation values over the retained
854 threshold. The selection is made on significant correlations values (see also Appendix G).

855 The community detection algorithm is a greedy optimization of the modularity measure, from
856 the default method of the `igraph` package [95], `igraph.Graph.community_fastgreedy` [96].

857 **Appendix C. Merging Tohoku and Waxholm atlases**

858 Brain areas are obtained from the fusion of areas in the Tohoku atlas [24] and areas in the
859 Waxholm Space atlas (WHS) [25]. The first contains cortical areas, the second focuses on sub-
860 cortical ones. Nomenclatures from Tohoku atlas are: agranular insular area dorsal (AID), posterior (AIP),
861 ventral(AIV); amygdalopiriform transition area (APir); primary auditory area (Au1); secondary auditory cortex, dorsal area (AUD);
862 secondary auditory cortex, ventral area (AuV); cingulate cortex, area 1 (Cg1); cingulate cortex, area 2 (Cg2); dysgranular insular cortex

863 (DI); Entorhinal area (DIEnt); Entorhinal area (DLEnt); dorsolateral orbital cortex (DLO); entorhinal cortex (Ect); frontal association
864 cortex (Fr3); granular insular cortex (GI); granular insular cortex dysgranular insular cortex (GIDI); lateral parietal association cortex
865 (LPtA); primary motor cortex (M1); supplementary motor cortex (M2); entorhinal cortex, medial part (MEnt); medial parietal associa-
866 tion cortex (MPtA); perirhinal cortex (PRh); Parietal association cortex (PtPC), (PtPD), (PtPR); retrosplenial cortex (RSD), (RSGb),
867 (RSGc); primary somatosensory cortex (S1), barrel field (S1BF), dysgranular zone (S1DZ), dysgranular zone (S1DZ0), forelimb region
868 (S1FL), hindlimb region (S1HL), jaw region (S1J), (S1Sh), trunk region (S1Tr), upper limb (S1ULp); second somatosensory cortex
869 (S2); temporal cortex, association area (TeA); primary visual cortex (V1), binocular region (V1B), monocular region (V1M); secondary
870 visual cortex, lateral part (V2L), mediolateral part (V2ML), mediomedial part (V2MM); Entorhinal area (VIEnt) **Nomenclatures**
871 **from WHS atlas are:** Clear Label (0); descending corticofugal pathways (cfp); substantia nigra (SN); subthalamic nucleus
872 (STh); molecular layer of the cerebellum (Cb m); granule cell level of the cerebellum (Cb g); alveus of the hippocampus (alv); inferior
873 cerebellar peduncle (icp); striatum (CPu); globus pallidus (GP); entopeduncular nucleus (EP); ventricular system (VS); medial lemnis-
874 cus (MI); facial nerve (7n); anterior commissure, anterior part (aca); anterior commissure, posterior part (acp); ventral hippocampal
875 commissure (vhc); thalamus (Th); septal region (Sep); optic nerve (2n); optic tract and optic chiasm (opt); pineal gland (Pi); inner ear
876 (IE); commissure of the superior colliculus (csc); brainstem (BS); hypothalamic region (H); inferior colliculus (IC); superficial gray layer
877 of the superior colliculus (SuG); periaqueductal gray (pag); fornix (f); mammillothalamic tract (mt); commissural stria terminalis (cst);
878 deeper layers of the superior colliculus (DpG); periventricular gray (PVG); genu of the facial nerve (g7); pontine nuclei (Pn); fimbria
879 of the hippocampus (fi); fasciculus retroflexus (fr); stria medullaris of the thalamus (sm); stria terminalis (st); posterior commissure
880 (pc); glomerular layer of the accessory olfactory bulb (GIA); glomerular layer of the olfactory bulb (GI); olfactory bulb (OB); corpus
881 callosum and associated subcortical white matter (cc); brachium of the superior colliculus (bsc); commissure of the inferior collicu-
882 lus (cic); interpeduncular nucleus (IP); ascending fibers of the facial nerve (asc7); anterior commissure (ac); spinal trigeminal nuclus
883 (SPN); spinal trigeminal tract (sp5); frontal association cortex (FrA); middle cerebellar peduncle (mcp); transverse fibers of the pons
884 (tfp); habenular commissure (hbc); nucleus of the stria medullaris (SM); basal forebrain region (BF); supraoptic decussation (sox); bed
885 nucleus of the stria terminalis (BST); pretectal region (PT); cornu ammonis 3 (CA3); dentate gyrus (DG); cornu ammonis 2 (CA2);
886 cornu ammonis 1 (CA1); fasciola cinereum (FC); subiculum (S); postrhinal cortex (PrCx); presubiculum (PrS); parasubiculum (PaS);
887 perirhinal area 35 (Per35); perirhinal area 36 (Per36); entorhinal cortex (Ent); lateral entorhinal cortex (LEnt); parabrachial nucleus
888 (PB); **Some areas are both atlases and are merged in the final one. Fusions of areas for left and right**
889 **hemisphere are as follows, with the name of the resulting area given in Table 1, followed by the**
890 **list of the regrouped areas:** 0: {0}; ACC: {Cg1 r, Cg2 r, Cg1 l, Cg2 l}; Ins: {AID, AIP, AIV, DI, GI, GIDI}; APir: {APir};
891 AU: {AU1, AUD, AUV}; Ent: {DIEnt, DLEnt, Ect, MEnt, PRh, VIEnt, PrCx, Per35, Per36, Ent, LEnt}; Par: {LPtA, MPtA, PtPC,
892 PtPD, PtPR}; M1: {M1}; M2: {M2}; RSC: {RSD, RSGb, RSGC}; S1: {S1, S1DZ, S1DZ, S1FL, S1HL, S1J, S1Sh, S1Tr, S1ULp};
893 S1BF: {S1BF}; S2: {S2}; TeA: {TeA}; V1: {V1, V1B, V1M}; V2: {V2L, V2ML, V2MM}; CPu: {CPu}; BG: {SN, STh, GP, EP}; Th:
894 {Th}; Sep: {Sep}; H: {H}; DSC: {SuG, DpG, bsc}; pag: {pag}; BF: {BF}; PT: {PT}; HIP: {CA3, DG, CA2, CA1}; S: {S, PrS, PaS};
895 f: {cfp, MI, 7n, aca, acp, vhc, 2n, opt, csc, f, mt, cst, g7, fi, fr, sm, st, pc, cc, cic, asc7, ac, sp5, mcp, tfp, hbc, sox, FC, BST}; n: {IC,
896 Cb m, Cb g, alv, icp, VS, Pi, IE, BS, PVG, Pn, GIA, GI, IP, SPN, SM, Fr3, FrA, DLO, OB, PB}; **Note that 0 clear label,**
897 **fibers (f) and not available areas (n) are not taken into account in the study.**

898 Centers are projected on the left and right (LR) axis, inferior-superior (IS) axis and on the
899 posterior-anterior (PA) with the origin at (0, 0, 0) given by the position of bregma at the apex of
900 the most forward crossing fibers of the anterior commissure. Coordinates are given in millimeters.
901 For sake of symmetry, the average left-right center of gravity is considered. The position of ACC
902 is set to 0 on the LR axis, even if a small shift is present in the template. The smallest area TeA r
903 has a volume of 3.070 mm^3 (1572 voxels at 0.002 mm^3 or 12 voxels at 0.242 mm^3), the largest one
904 CPu r, has a volume of 45.143 mm^3 (23113 or 186 voxels, respectively).

905 **Appendix D. Extraction of signals from fMRI and atlas**

906 The simple way to compute the signals in areas defined in the atlas is to transform the data
907 from the fMRI low resolution volume to data in the high resolution volume where the atlas is

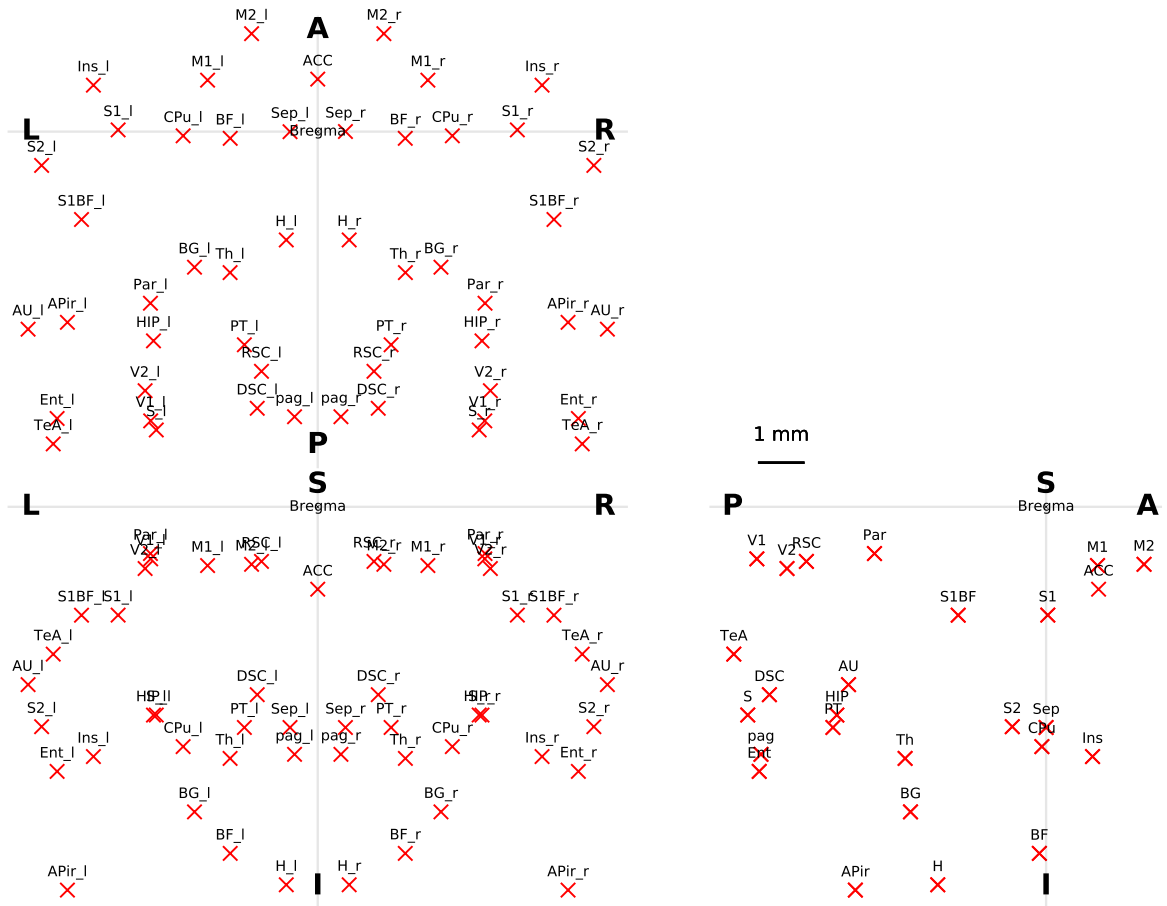


Figure C.9: Locations of the centers of gravity of the areas retained in this study on the three projections LR-IS, PA-IS, and PA-LR. Notations: left to right axis (LR), inferior to superior axis (IS), posterior to anterior axis (PA).

Table C.2: Brain areas in the atlas

#	name	label	x	y	z	N	h.	w. a.
<i>0</i>	<i>Clear Label</i>	<i>0</i>	<i>0.2</i>	<i>-4.6</i>	<i>-4.5</i>	<i>1718587</i>		
1	anterior cingulate cortex	ACC	0.2	-1.9	1.2	16670		acc
2	insular cortex right	Ins r	5.2	-5.7	0.9	11026	r	c
3	amygdalopiriform transition area right	APir r	5.7	-8.8	-4.3	3264	r	c
4	auditory cortex right	AU r	6.6	-4.2	-4.5	8781	r	c
5	entorhinal area right	Ent r	5.9	-6.1	-6.4	18392	r	c
6	parietal association cortex right	Par r	4.0	-1.2	-3.9	4557	r	c
7	primary motor cortex right	M1 r	2.7	-1.4	1.1	11027	r	c
8	supplementary motor cortex right	M2 r	1.7	-1.3	2.2	6619	r	c
9	retrosplenial cortex right	RSC r	1.5	-1.3	-5.5	8222	r	c
10	somatosensory 1 right	S1 r	4.6	-2.6	-0.0	20647	r	c
11	somatosensory 1 right, barrel field	S1BF r	5.5	-2.6	-2.0	9249	r	c
12	somatosensory 2 right	S2 r	6.2	-5.1	-0.8	2365	r	c
13	temporal cortex right, association area	TeA r	6.1	-3.5	-7.1	1572	r	c
14	primary visual cortex right	V1 r	4.0	-1.3	-6.5	9100	r	c
15	secondary visual cortex right	V2 r	4.1	-1.5	-5.9	4350	r	c
16	insular cortex left	Ins l	-5.0	-5.6	1.2	9002	l	c
17	amygdalopiriform transition area left	APir l	-5.7	-8.6	-4.3	3411	l	c
18	auditory cortex left	AU l	-6.5	-3.9	-4.5	9338	l	c
19	entorhinal area left	Ent l	-5.9	-5.8	-6.6	17859	l	c
20	parietal association cortex left	Par l	-3.6	-0.9	-3.9	4557	l	c
21	primary motor cortex left	M1 l	-2.3	-1.3	1.3	11160	l	c
22	supplementary motor cortex left	M2 l	-1.3	-1.3	2.2	5708	l	c
23	retrosplenial cortex left	RSC l	-1.1	-1.2	-5.3	7527	l	c
24	somatosensory 1 left	S1 l	-4.4	-2.3	0.1	21813	l	c
25	somatosensory 1 left, barrel field	S1BF l	-5.2	-2.3	-2.0	9578	l	c
26	somatosensory 2 left	S2 l	-6.3	-4.8	-0.8	2547	l	c
27	temporal cortex left, association area	TeA l	-5.9	-3.2	-7.1	1731	l	c
28	primary visual cortex left	V1 l	-3.6	-1.1	-6.6	9439	l	c
29	secondary visual cortex left	V2 l	-3.7	-1.3	-5.9	4276	l	c
30	caudate-putamen striatum right	CPu r	3.0	-5.6	-0.1	23113	r	s
31	basal ganglia right	BG r	2.6	-7.1	-3.1	3548	r	s
32	thalamus right	Th r	2.0	-5.8	-3.2	16544	r	s
33	septal region right	Sep r	0.6	-5.0	0.0	2167	r	s
34	hypothalamic region right	H r	0.6	-8.6	-2.5	2613	r	s
35	superior colliculus right	DSC r	1.4	-4.4	-6.3	6253	r	s
36	periaqueductal gray right	pag r	0.5	-5.5	-6.6	2745	r	s
37	basal forebrain region right	BF r	1.8	-8.0	-0.3	13759	r	s
38	pretectal region right	PT r	1.6	-5.1	-4.8	1805	r	s
39	hippocampus right	HIP r	3.7	-4.9	-4.7	19137	r	s
40	subiculum right	S r	3.6	-4.8	-6.8	5671	r	s
41	caudate-putamen striatum left	CPu l	-3.1	-5.2	-0.1	22803	l	s
42	basal ganglia left	BG l	-3.0	-6.7	-3.1	3238	l	s
43	thalamus left	Th l	-2.0	-5.6	-3.2	18218	l	s
44	septal region left	Sep l	-0.6	-5.0	-0.0	2733	l	s
45	hypothalamic region left	H l	-0.8	-8.5	-2.4	4246	l	s
46	superior colliculus left	DSC l	-1.3	-4.2	-6.3	6465	l	s
47	periaqueductal gray left	pag l	-0.5	-5.7	-6.3	3794	l	s
48	basal forebrain region left	BF l	-2.1	-7.7	-0.0	17694	l	s
49	pretectal region left	PT l	-1.7	-4.9	-4.8	1706	l	s
50	hippocampus left	HIP l	-3.8	-4.5	-4.8	18981	l	s
51	subiculum left	S l	-3.7	-4.6	-6.7	5962	l	s
<i>52</i>	<i>fasciculum</i>	<i>f</i>	<i>-0.0</i>	<i>-4.8</i>	<i>-3.1</i>	<i>59834</i>		
<i>53</i>	<i>not available</i>	<i>n</i>	<i>-0.1</i>	<i>-5.8</i>	<i>-7.7</i>	<i>261557</i>		

For each area: name of the area (name); label (label); the coordinates of the center of gravity (x, y, z), in mm, in the referential LR, IS, PA, with the origin centered at bregma location; N, the number of voxels in the area with a voxel size of 0.125 mm by 0.125 mm by 0.125 mm, in a cube of 136 by 102 by 180 voxels; the hemisphere (hemi.), left (l.) or right (r.); and the name of the wider area (w. a.), anterior cingulate cortex (acc), cortical (c) or subcortical (s). Rows in italic correspond to areas containing unlabeled subareas, undefined or unspecific residuals components not used in the study.

908 defined. The signal in one fMRI area is obtained as the sum of all voxels of this area in the atlas.
 909 This process implies to transform large voxels into small ones. The extraction of signals from the
 910 low resolution volume fMRI is possible if one can compute the proportion of each area contained in
 911 voxels of the fMRI. The processing of signals from the low resolution volume fMRI can then be seen
 912 as a weighted summation of voxel data for each area or a source separation problem. This enables
 913 to reduce the size of the processed images and reduce the computation times, while obtaining the
 914 same result as if working in the high resolution volume of the atlas. The mathematical framework
 915 for this operation is described here.

916 *Appendix D.1. Equivalence of operations for processing low resolution volumes and high ones*

917 Let V_1 and V_2 be two volumes containing MRI values at different resolutions. V_1 and V_2 contains
 918 respectively N_1 and N_2 voxels. We consider here that: each voxel i_1 in V_1 is associated to one label
 919 of one area of the atlas; V_1 contains more voxels than V_2 , or $N_1 \geq N_2$. This is generally the case
 920 when V_1 is the anatomical volume and V_2 is the fMRI volume with a lower resolution. Voxels in V_2
 921 intersect voxels in V_1 at different locations. An example in two dimensions is given in Fig. D.10.
 922 Let K be the number of areas in the atlas and k the area label with index k . Let $s(k, t)$ be the
 923 signal of area k at time t . Let $s_1(k, t)$ and $s_2(k, t)$ be the signals computed from V_1 and V_2 . The
 924 problem here is to obtain $s_2(k, t) = s_1(k, t) = s(k, t)$.

925 If the fMRI is obtained from V_2 , values $x_2(i_2, t)$ of voxels i_2 are transformed into V_1 such that
 926 i_1 contains values $x_1(i_1, t)$ by applying:

$$\begin{aligned} x_1(i_1, t) &= \sum_{i_2} \rho(i_1, i_2) x_2(i_2, t) \\ \text{or } X_1(t) &= R X_2(t) \quad \text{in matrix notation} \end{aligned} \quad (\text{D.1})$$

927 where $\rho(i_1, i_2)$ contains the fraction of i_2 in i_1 . $s_1(k, t)$ can be computed by taking the voxels
 928 labeled with area k , or when taking $\omega(i_1)$, the label of the area related to the voxel i_1 in the atlas,
 929 by:

$$\begin{aligned} s_1(k, t) &= \sum_{i_1 | \omega(i_1)=k} x_1(i_1, t) \\ \text{or } s_1(k, t) &= \sum_{i_1} w_1(k, i_1) x_1(i_1, t) \\ \text{or } S_1(t) &= W_1 X_1(t) \quad \text{in matrix notation} \end{aligned} \quad (\text{D.2})$$

930 Where w_1 is an indicator function giving $w_1(k, i_1) = 1$ if $\omega(i_1) = k$ and 0 otherwise. This leads to
 931 :

$$\begin{aligned} s_1(k, t) &= \sum_{i_1} w_1(k, i_1) \sum_{i_2} \rho(i_1, i_2) x_2(i_2, t) \\ S_1(t) &= W_1 R X_2(t) \end{aligned} \quad (\text{D.3})$$

932 By taking $w_2(k, i_2) = \sum_{i_1} w_1(k, i_1) \rho(i_1, i_2)$ or $W_2 = W_1 R$ in matrix notation this leads to:

$$\begin{aligned} s_1(k, t) &= \sum_{i_2} w_2(k, i_2) x_2(i_2, t) \\ S_1(t) &= W_2 X_2(t) = S_2(t) \end{aligned} \quad (\text{D.4})$$

933 This implies that $s_1(t)$ computed in this way does not rely on the computation of x_1 and can be
 934 noted $s_2(t)$.

935 Now, suppose that the signal recorded in V_2 , $x_2(t)$ is a combination of $s(k, t)$ such that:

$$X_2(t) = M S(t) \quad (\text{D.5})$$

936 With M a mixing matrix of size (N_2, K) . The resolution of this equation is given by the pseudo
 937 inverse and leads to:

$$S(t) = (M^t M)^{-1} M^t X_2(t) \quad (\text{D.6})$$

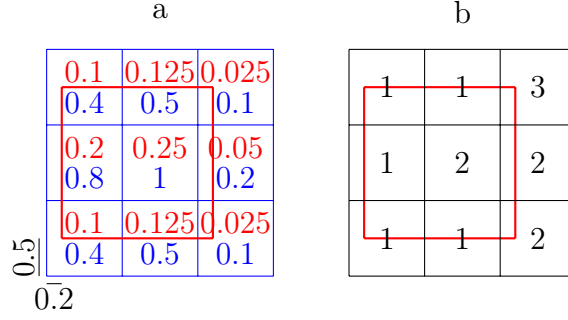


Figure D.10: Example of: a) the transformation from volume V_1 to volume V_2 and in blue the fraction $\rho(i_1, i_2)$ and the proportion of components from $s(i, t)$ in red (see text for details); b) the label contained in V_1 and the intersection with V_2 .

938 with \cdot^t the notation for the transpose operator. This implies that one admissible solution for
 939 $S_2(t) = S(t)$ is obtained if $W_2 = (\hat{M}^t \hat{M})^{-1} \hat{M}^t$ or $W_2 \hat{M} = I$. \hat{M} is then a pseudo inverse of W_2
 940 and can be chosen this way. Thus, the matrix W_2 is obtained from R and W_1 computed on our
 941 configuration, with the atlas in high resolution and the fMRI in low resolution. This last has been
 942 used to compute the signals of each area from the signals in the fMRI volumes in 3D.

943 *Appendix D.2. Example of the equivalence of operations for processing low resolution volumes and*
 944 *high ones*

945 An example of equivalence of operations for extracting brain areas signals from volume V_1 (in
 946 blue) and V_2 (in red) is given in Fig. D.10. In the 2D example, there are three labels $\{1, 2, 3\}$, nine
 947 voxels in V_1 and one in V_2 . If voxels are viewed rowwise, one can make the hypothesis that x_2 is
 948 obtained from :

$$x_2(1, t) = M (s(1, t), s(2, t), s(3, t))^t$$

949 with M being a 3 by 1 matrix here. Taking the red proportions, obtained by computing the ratio
 950 of the areas of the intersections of the blue voxels over the area of the red voxel, and summing
 951 them for each labeled area leads to:

$$\begin{aligned} M &= (0.1 + 0.125 + 0.2 + 0.1 + 0.125, 0.25 + 0.05 + 0.025, 0.025) \\ M &= (0.65, 0.325, 0.025) \end{aligned} \tag{D.7}$$

952 The signal recorded in the red voxel is a composition of the signal in the three areas with a mixture
 953 according to M . In simple words, the signal recorded in the red voxel is made of 65% of signal
 954 from area 1, 32.5% of signal from area 2 and 2.5% of signal from area 3.

955 All blue voxels are represented in a flat vector of dimension 9 in rowwise reading, from the
 956 top left to the bottom right. Taking the blue proportions, obtained by computing the ratio of the
 957 intersections of the red voxel with the areas of each blue voxel, gives R , the weights of voxels from
 958 V_2 in V_1 :

$$R = (0.4, 0.5, 0.1, 0.8, 1, 0.2, 0.4, 0.5, 0.1)^t$$

959 The mixture matrix in V_1 from the 9 voxels to the 3 signals is given by W_1 :

$$W_1 = \begin{pmatrix} 1 & 1 & 0 & 1 & 0 & 0 & 1 & 1 & 0 \\ 0 & 0 & 0 & 0 & 1 & 1 & 0 & 0 & 1 \\ 0 & 0 & 1 & 0 & 0 & 0 & 0 & 0 & 0 \end{pmatrix}$$

960 This leads to:

$$W_2 = W_1 R = (2.6, 1.3, 0.1)^t$$

961

$$\hat{M} \approx (0.31, 0.15, 0.01)$$

962 \hat{M} and M are related with a factor equals to $\sum_k \hat{m}_k \approx 0.47$. Thus, signals at low resolution and
 963 high resolution just differ by a scaling factor.

964 **Appendix E. Movement filtering with framewise displacement**

965 Following observations in [92], we examined carefully the potential influence of motions on the
 966 obtained signals. In order to obtain the best estimates of FC during resting state, a selection of the
 967 parts of signals not contaminated potentially by movement is performed. Samples with a framewise
 968 displacement (FD) [92] over an experimental threshold are discarded from the study. The threshold
 969 is set manually to 0.1 mm, based on observations, see infra., and corresponding to approximately
 970 1/4 of the smaller voxel dimension (0.47 mm) and 1/9 of the larger voxel dimension (0.9 mm). All
 971 samples following a sample with FD over this threshold are also marked as movement and discarded
 972 for the study. This is done to take into account the effect of an hemodynamic response function
 973 (HRF). The maximal duration of this HRF is set to 20 s based on values proposed in literature (see
 974 [91] for example and references). The border effects of the signals at different scales are then taken
 975 into account. To summarize, with technical terms of the field, we applied a scrubbing method with
 976 boxcar filtering [37] taking into account HRF and wavelet support at different scales. An example
 977 of the FD obtained for one rat is given in the Fig. E.11 a) with the impact on the signals at the
 978 different frequency bands. An overview of the FD obtained for all rats is given in the Fig. E.11 b).
 979 Three rats showed major displacements (FD over 0.47 mm). Distributions of FD are proposed in
 980 the Fig. E.11 c-d) with the proposed threshold for this study. The impact of the selection of the
 981 unretained samples on the signals at the different frequency bands is presented in the Fig. E.11
 982 h-g) for all rats. The impact on signals at low frequencies (g - cD7) is important, as a consequence
 983 of the width of the wavelet support at this scale, leading to few or no available samples to estimate
 984 FC.

985 **Appendix F. Spectral analysis of fMRI signals and frequency bands**

986 To evaluate which part of the BOLD raw signal is filtered at each frequency band, the power
 987 spectral densities (PSD) by groups are given in Fig. F.12. PSD are estimated using a Welch
 988 averaging method (frequency precision 3.9e-3 Hz, duration of segments 128 s, overlap: 50%). PSD
 989 per area and per rat are superimposed in black with a transparency factor. The median PSD
 990 for each rat is computed and the average value is given in color for each group with a margin
 991 corresponding to the standard error of the mean. An acquisition artifact, visible in all groups
 992 including the dead animal, may be seen close to the cD2 upper frequency (0.5 Hz).

993 *Appendix F.1. Frequency bands used in other FC studies*

994 For comparison purpose, a graphical representation of the different frequency bands retained
 995 in other rat studies is proposed in the Fig. F.13 (see also [36]).

996 **Appendix G. Construction of FC graphs from band filtered signals taking into account 997 significant correlations**

998 Two important points must be considered during the construction of FC graphs:

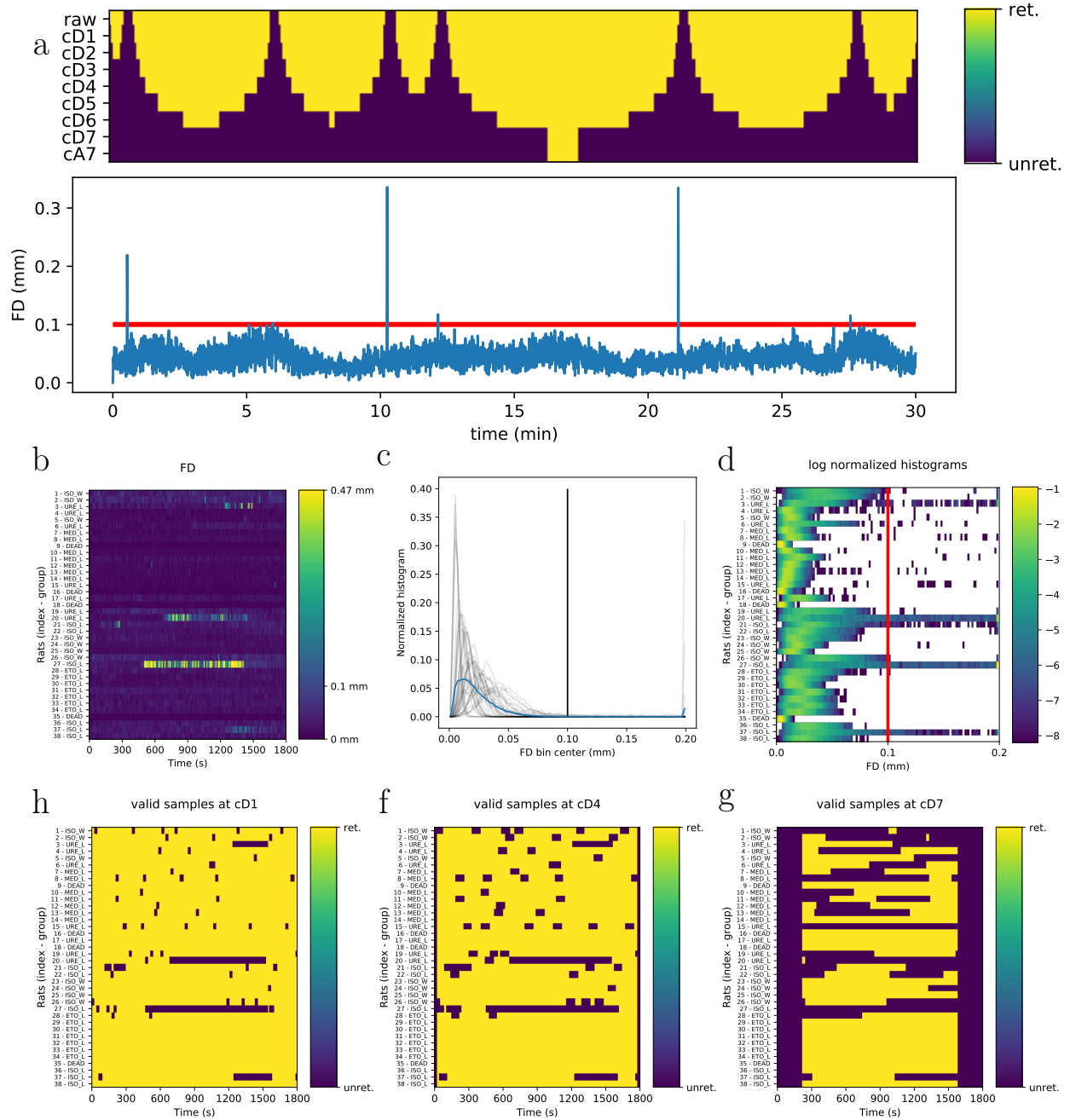


Figure E.11: Selection of retained rs-fMRI based on framewise displacement (FD). a) FD and impact on the raw signal and signals at different frequency bands. b) Overview of the FD for all rats. 0.47 mm represents the lowest dimension of voxels. 0.1 is the threshold used in the study. c) Normalized histograms of FD: rats histograms are proposed in gray. Values of FD over 0.2 are set to 0.2. Values in bins are normalized by dividing samples in bins with the total number of samples. The average histogram computed with all individuals is given in blue. d) Overview of histograms for each rat: a logarithmic version is proposed to enhance details and put in evidence that some values over the threshold are observed in several rats. h-f) Examples of the retained (ret.) and unretained (unret.) samples for the signal at cD1 (h), cD4 (f) and cD7 (g). The number of rejected samples increases as the frequency decreases because of the impact of the wavelet support.

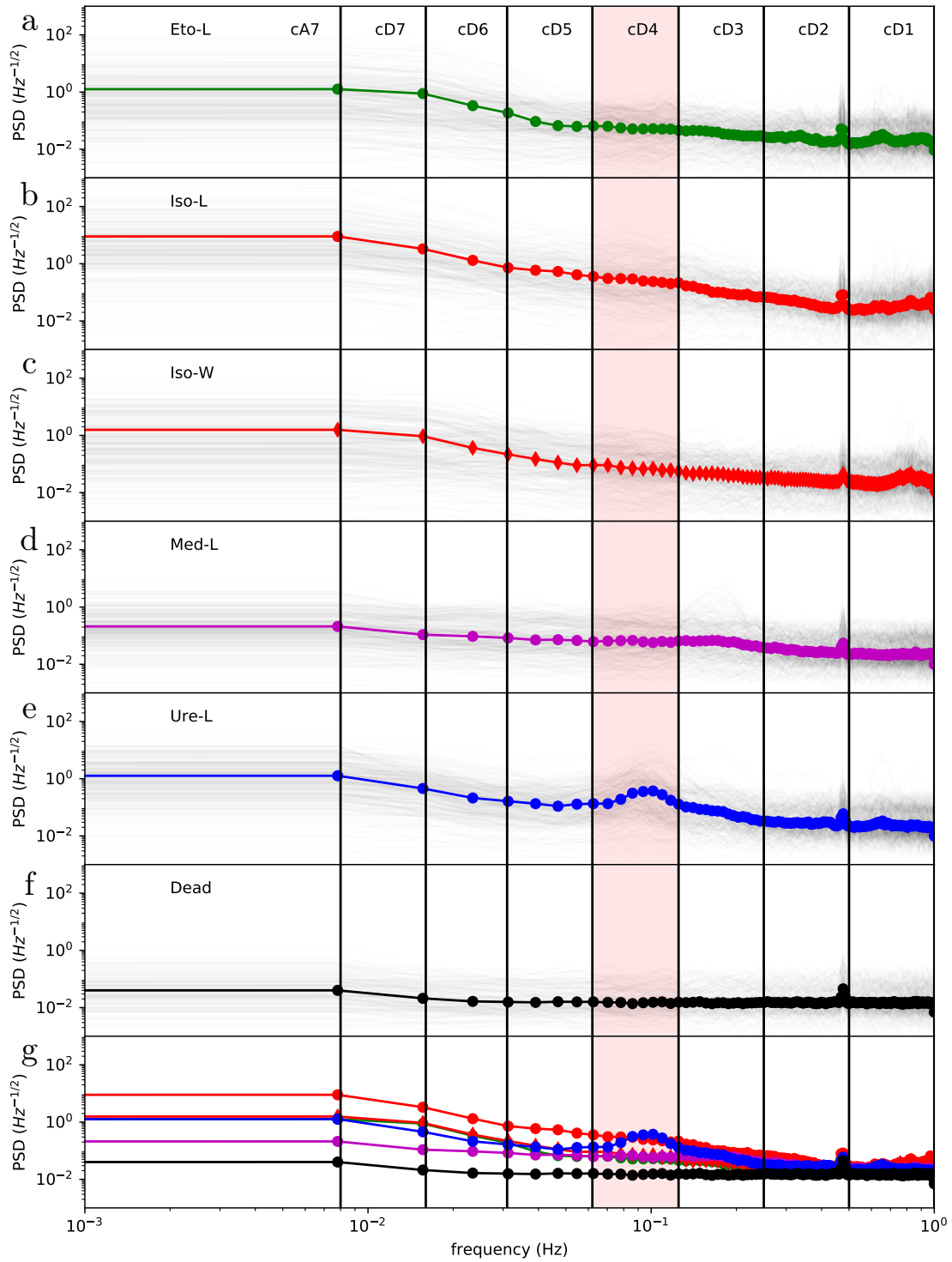


Figure F.12: Power spectral density (PSD) of BOLD raw signals by group. a-f) For each group, the 51 PSD of each animal are superimposed in black with a transparency factor. The median values per frequency is computed for each animal. Means and standard errors of the mean are given in colors. The cD4 band, retained in this study and called BOLD signal, is colored in red. g) Average PSD for the different groups.

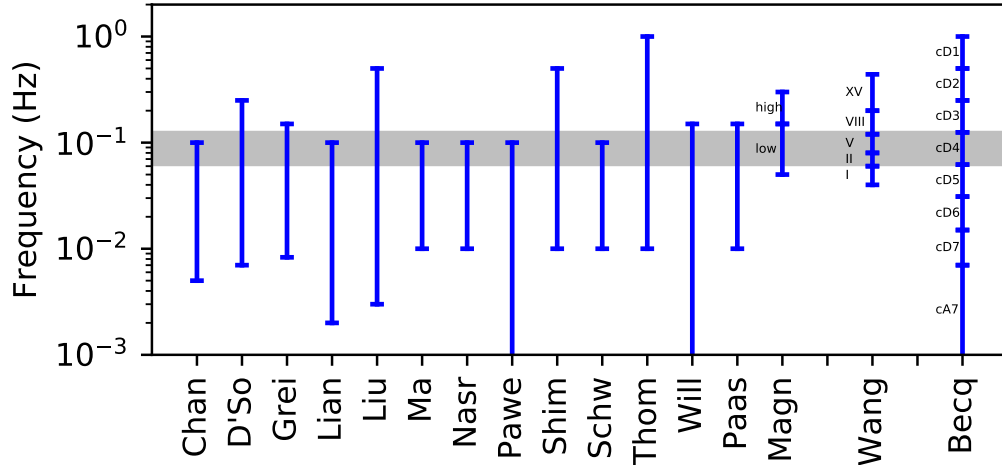


Figure F.13: Frequency bands retained in different rat rs-fMRI studies and all the frequency bands available in this study. The cD4 band (i.e. the BOLD signal) is filled in gray. Frequency cuts in Hz are given in parenthesis. The repetition time TR is also provided. [71] (0.005, 0.1) TR = 1.5 s; [40] (0.007, 0.25) TR = 2 s; [97] (0.0083, 0.15) TR = 2 s; [74] (0.002, 0.1) TR = 1 s; [44] (0.003, 0.5) TR = 0.612 s; [98] (0.01, 0.1) TR = 1 s; [58] (0.01, 0.1) TR = 2 s; [83] (0, 0.1) TR = 2 s; [68] (0.01, 0.5), and detrended to the second order, TR = 1 s; [85] (0.01, 0.1) TR = 1.7 s; [16] (0.01, 1), and linear detrend, TR = 0.5 s; [14] (0, 0.15), and normalisation, TR = 0.1 s; [6] (0.01, 0.15), TR = 2 s; [76] (0.05, 0.15, 0.30) and normalisation TR = 0.5 s; [99] (0.04, 0.06, 0.08, 0.12, 0.2, 0.44) simulated TR = 2 s; Becq et al., this study, (0, 0.007, 0.015, 0.031, 0.062, 0.125, 0.25, 0.5, 1) TR = 0.5 s.

- 999 • Spurious correlations depend of the number of samples used to compute correlations. This
1000 number is function of the frequency band of interest. For a lower frequency of interest, fewer
1001 samples are needed, and spurious correlations are less likely.
- 1002 • Spurious correlations are obtained when comparing multiple values of correlations as a conse-
1003 quence of multiple connections between brain areas. This implies to adjust level for multiple
1004 corrections.

1005 First, we evaluate whether there are enough signals in the graphs to get a sufficient number of
1006 edges by counting the number of significant edges different from zero. This number is computed
1007 using the results from [26] where it is shown that the Fisher transform z of the empirical correlation
1008 $\hat{\rho}$ follows a Gaussian law with mean the Fisher transform of the true value and variance depending
1009 on the number of available wavelet coefficients at scale j , denoted N_j here. The confidence interval
1010 $[\rho_m, \rho_M]$ for the correlation of two random signals is given in [100, 26] at a given scale j with a
1011 Daubechies wavelet filter of length L .

$$\rho_{m,M} = \tanh \left(h(\rho) \pm \frac{\Phi^{-1}(1-p)}{\sqrt{(\hat{N}_j - 3)}} \right) \quad (\text{G.1})$$

$$\hat{N}_j = \frac{N}{2^j} - [L_j] \quad (\text{G.2})$$

$$L_j = (L - 2) (1 - 2^{-j}) \quad (\text{G.3})$$

1014 where \hat{N}_j is the number of wavelet coefficients associated with scale λ_j , $h(\rho) = \tanh^{-1}(\rho)$ and
1015 $\Phi^{-1}(p)$ is the p th quantile of the standard normal distribution. A Bonferroni procedure is applied

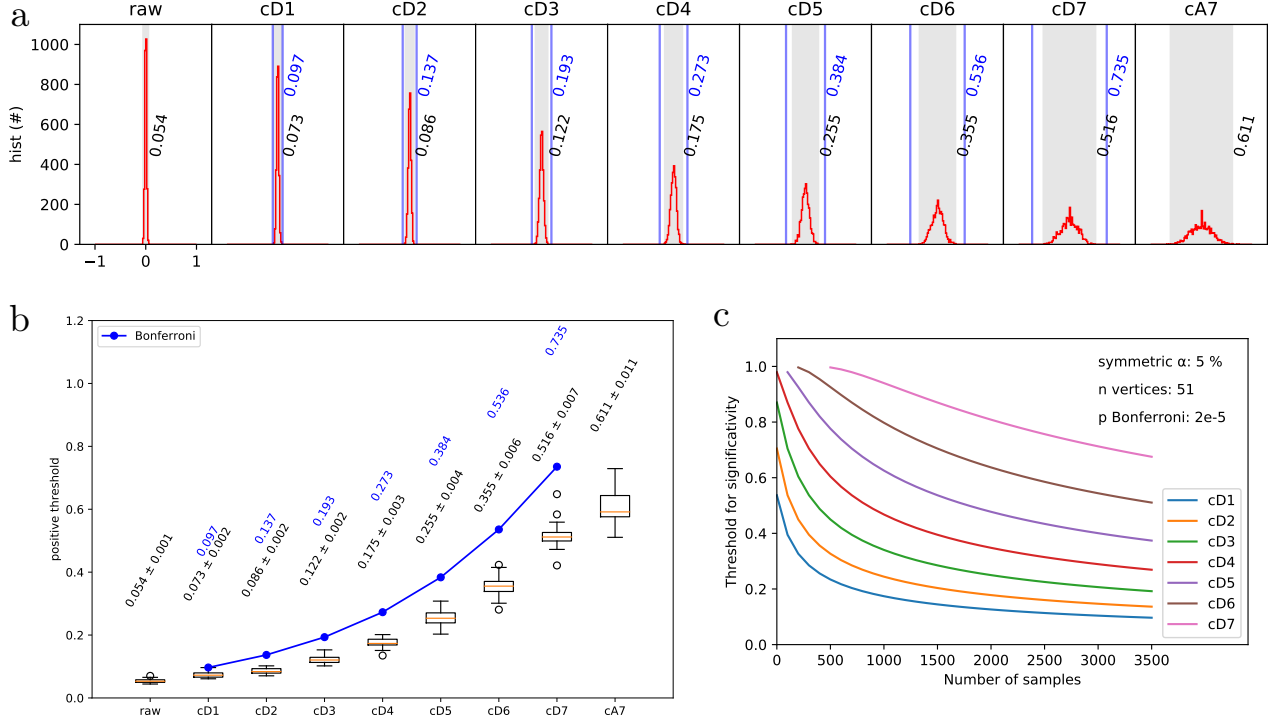


Figure G.14: Distributions of correlations at different scales for one drawing of random signals and the empirical upper limit threshold of the segment containing 99.998% (95% Whitcher + Bonferroni procedure) of the values. a) Histograms estimated on 100 bins between $[-1, 1]$; b) Boxplot of the thresholds containing 99.998% of the distributions at different wavelet levels. Values from the Bonferroni procedure with a an initial symmetrical confidence interval at 95 % are in blue. Values from empirical distributions of the simulated noises are given in black. c) Threshold for significant correlations in function of the number of samples per frequency bands. Plots are obtained with Eq.G.4 setting $p=2e-5$ for taking into account Bonferroni corrections on a symmetric test at level $\alpha = 5\%$ with 51 areas.

1016 to the p value to take into account $ne = nv(nv - 1)/2 = 51 \times 50/2 = 1275$ repetitions of the
 1017 $nv = 51$ brain areas to obtain a level with $p_{bf} = p/ne$.

1018 A model of uncorrelated random noises, with $\rho = 0$, is used to obtain significant thresholds at
 1019 an initial symmetrical confidence interval set to 95 % leading, after Bonferroni correction, to a level
 1020 $p_{bf} = 0.025/1275 = 1.96e-5 = 0.002\%$. 51 signals with 3600 samples with i.i.d. samples following
 1021 a Gaussian distribution $N(0, 1)$ are simulated. The same wavelet decomposition than the one used
 1022 for the BOLD signals is applied and the ne correlations are estimated for each wavelet coefficients.
 1023 Examples of distributions of the correlations at different wavelet levels are given in Fig. G.14a.
 1024 Values are ranked and the correlation value of the $i_{th} = ne(1 - p_{bf}) = 1275 \times (1 - 1.96e-5) = 1275$
 1025 th (max) is retained as the threshold level for which 99.998% of $abs(C)$ is contained. Theoretical
 1026 values given by Whitcher and the Bonferroni procedure are given in blue. Distributions and values
 1027 of these thresholds at different wavelet levels are given in Fig. G.14b with the segment containing
 1028 99.998% of the values represented in gray.

1029 Differences between theoretical thresholds and experimental ones increase with scale indices.
 1030 Unfortunately, there is no result about the theoretical distribution of the correlation coefficients
 1031 to the best of our knowledge and it seems not easy to obtain.

1032 Because of the scrubbing based on FD, signals obtained on different rats do not have the same

1033 size. Besides, nonsuccessive samples are retained and in this condition, Eq. G.1 can not be applied
 1034 properly. But since the retained samples are already taking into account the influence of the
 1035 wavelet support, the following formula is used to obtain the limits of significant correlations:

$$\rho_{m,M} = \tanh \left(h(\rho) \pm \frac{\Phi^{-1}(1-p)}{\sqrt{\left(\frac{N_r}{2^j} - 3\right)}} \right) \quad (\text{G.4})$$

1036 with N_r the number of retained samples. The limits of significant correlations at different scales
 1037 in function of the number of retained samples is proposed in Fig. G.14c putting in evidence the
 1038 importance of the number of samples for obtaining significant correlations at low frequencies (cD7).

1039 This allows the computation of a confidence interval to remove the correlations that are below
 1040 the significance level. For examples, the theoretical Bonferroni threshold is 0.273 for the cD4 band,
 1041 if all samples are retained with $N = 3600$ for Eq. G.1 and $N_r = 3495$ for Eq. G.4 with a Daubechies
 1042 wavelet of size $L=8$. This is illustrated on the dead rats data where no signal is detected in the
 1043 graphs. Following this first step, the idea to use graphs is to be able to compare them. The
 1044 comparison of graphs with different number of edges is difficult because graph metrics are directly
 1045 impacted by this factor. We choose here to force the graphs to have the same number of edges,
 1046 selected from the significant ones. Because dead rats have a too small number of significant edges,
 1047 it is not possible to construct a graph with a constant number of edges for these animals.

1048 Appendix H. Supplementary Analyzes

1049 Appendix H.1. Scatter plots

1050 Scatter plots of SV, baseline CBF, BOLD variation and $\langle C \rangle$ BOLD-BOLD (Fig. I.20 to
 1051 Fig. I.28) can be further analyzed here. Most of the individuals in each group remain close to
 1052 each other indicating an homeostatic state specific to each anesthetic. The effect of the strain
 1053 can be evaluated on the Iso-L and Iso-W groups that show separated clouds. There are some
 1054 outliers: One individual with Temp < 35 °C in the Eto group but this is caused by problems
 1055 with the temperature sensors (regular values between 35 and 37 °C); One individual with SpO2 $<$
 1056 80% in the Ure group. Estimation of regression parameters and correlation coefficients are given
 1057 in each figure, with outliers discarded for the regression. There are some statistically significant
 1058 correlations:

- 1059 • weak correlations ($|R| < 0.5$): BOLD variation with (RR, Temp, Error rate, raw BOLD);
 1060 $\langle C \rangle$ BOLD-BOLD with (HR, Error rate, raw BOLD); HR with Error rate; RR with SpO2;
 1061 Temp with Error rate; Weight with raw BOLD.
- 1062 • medium correlations ($0.5 \leq |R| < 0.75$): BOLD variation with ($\langle C \rangle$ BOLD-BOLD, Error
 1063 rate); $\langle C \rangle$ BOLD-BOLD with Temp; baseline CBF with (HR, Temp); HR with Temp; RR
 1064 with Error rate; SpO2 with Error rate.
- 1065 • one strong correlation ($|R| \geq 0.75$): BOLD variation with $\langle C \rangle$ BOLD-BOLD.

1066 The error rate is correlated with several variables. This can be explained by the fact that when
 1067 the signal is lost on the oximeter, either the animal is not stable during the anesthesia creating
 1068 some artifacts measures, either the animal is in a state in which he needs to regulate himself. If the
 1069 animal is suffering, reactions can induce error rates, and these reactions are observed and can be

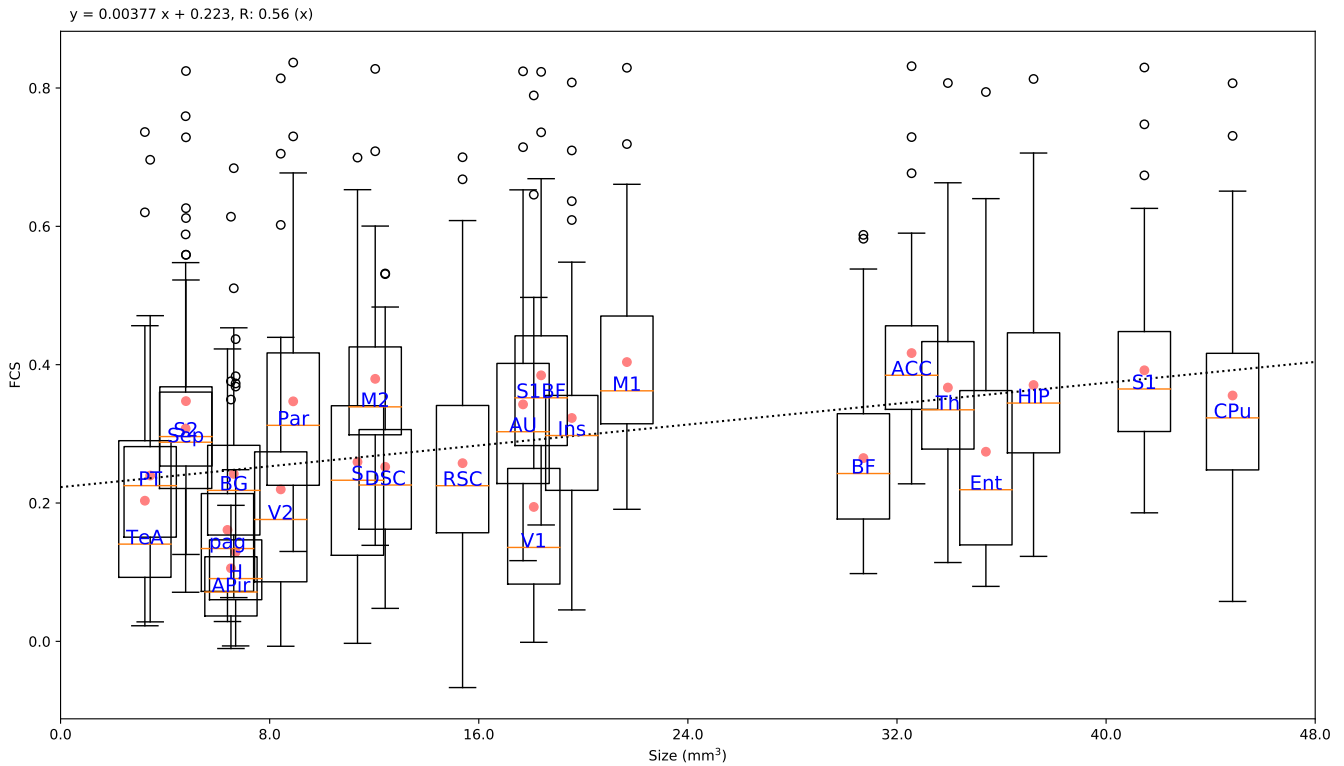


Figure H.15: FCS distributions across rats versus area size. Each box corresponds to one area with left and right areas pooled together. The dotted line corresponds to a linear fit estimated from the average values of the areas represented with red dots.

1070 related to the activity in BOLD signals. These reactions can also be related to an increase in $\langle C \rangle$
 1071 BOLD-BOLD with answers to the same conditional stimuli, e.g. pain, suffering, wake up. The
 1072 temperature is related to different variables especially, HR, baseline CBF, BOLD variation and
 1073 $\langle C \rangle$ BOLD-BOLD. This potentially indicates that 'hot rats' are better perfused, have stronger
 1074 neural activities and stronger FCS between areas. BOLD variation has a strong correlation with
 1075 $\langle C \rangle$ BOLD-BOLD indicating that rats with high BOLD variations show high correlations values
 1076 even after taking into account the motions correctly.

1077 *Appendix H.2. Influence of area size on FCS*

1078 Mean FCS across animals as a function of area size are shown Fig. H.15. There is a medium
 1079 correlation ($R=0.56, p<0.01$) between the area size and the FCS. The slope between these two
 1080 variables is weak (0.0035 per mm^3) and the high variability of the distributions indicates a low
 1081 influence of the size of the area on FCS.

1082 *Appendix H.3. Influence of distances on pairwise correlations*

1083 The distributions of pairwise correlations in function of pairwise distances between areas are
 1084 proposed in Fig.H.16 for each rat in each group (top) and for all rats in groups (bottom). Signif-
 1085 icant correlations are values above thresholds represented with black lines. The distributions are
 1086 homogeneous within groups except for some individuals, in particular in the Iso groups. Values of
 1087 correlations above thresholds are observed for all pairwise distances, even at long distances, except
 1088 for dead rats were only few spurious values are observed at short distances. This indicates that
 1089 long range correlations in all groups are observed.

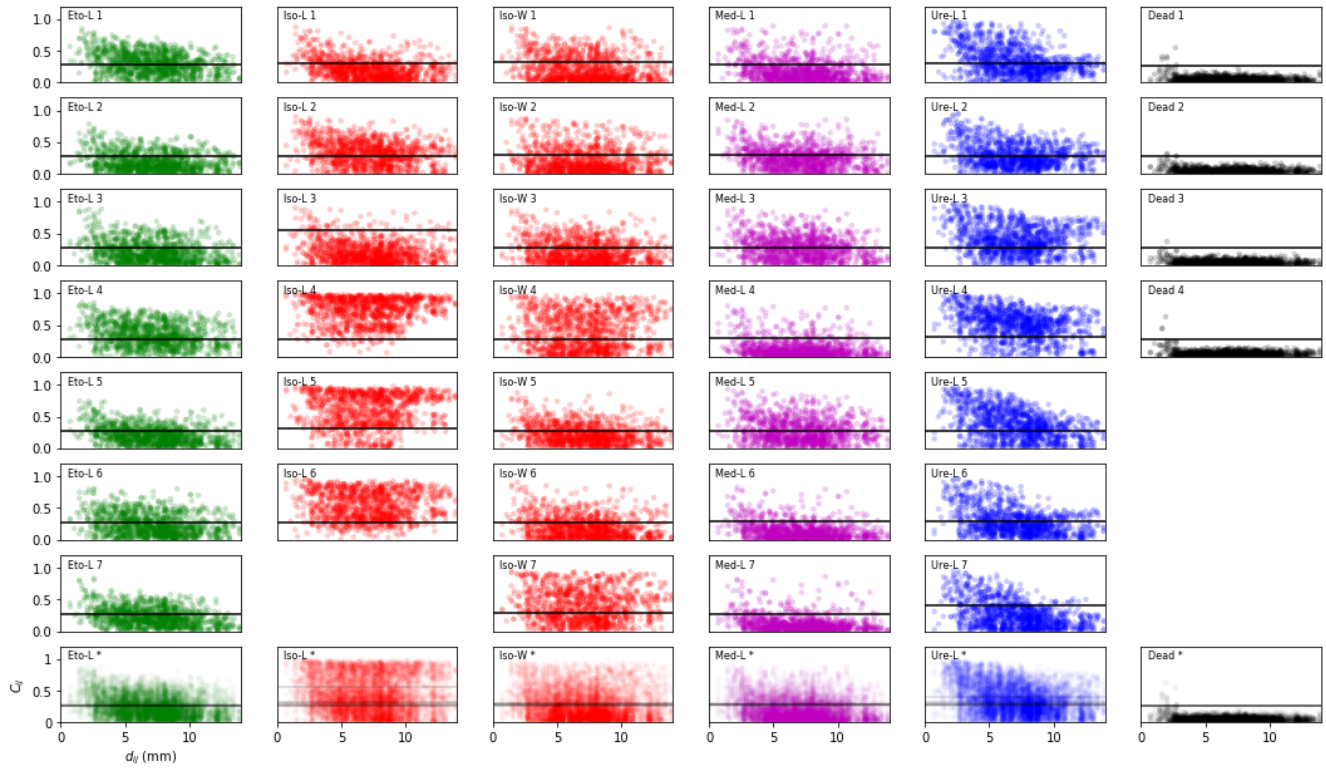


Figure H.16: Correlations between pairs of areas in function of distances between them. Scatters are given for each rat in each group and the total distribution is given in the bottom row indicated by *.

1090 *Appendix H.4. Influence of distances on pairwise FCS*

1091 The distributions of FCS computed on significant correlations, versus the spatial locations of
 1092 areas are given in Fig.H.17 for the different axis (LR, IS, AP) and in function of the Euclidean
 1093 distances to the Bregma origin. An area is represented by the coordinates of its center of gravity.
 1094 Anesthetized rats are pooled together to compute the box and whisker plots. Linear regressions
 1095 between the median values of FCS and distances are also computed. FCS does not seem to be
 1096 influenced by medio-lateral positions, even near ears (AU areas). There is a decrease of FCS in
 1097 function of the position to the sensors put in evidence in the dorso-ventral (IS) representation.
 1098 There is a decrease of FCS in function of the antero-posterior localization of the areas. These
 1099 attenuations of FCS are put in evidence with the representation in function of the Euclidean
 1100 distance to Bregma with a medium significant linear correlation ($R=-0.68$, $p=3.2e-8$), a light slope
 1101 ($-0.02 / \text{mm}$), and a high variability of distributions for some areas between rats. For all these
 1102 representations, range of values are more or less extended in function of areas.

1103 *Appendix H.5. Average matrices per group*

1104 Average matrices per group of the significant connections are computed. Representations using
 1105 graphs with nodes represented by the center of gravity of each area, on the 3 projections LR, IF,
 1106 AP, are proposed in Fig. I.38a. Edges are plotted one over the other with the lowest values plotted
 1107 first and the highest ones last. Different colors are also retained to show highest connected areas.
 1108 Highest connections are more or less different from one group to another. All areas are connected
 1109 on the anesthetized groups except one for Eto-L. Few edges are observed on the Dead group and
 1110 correspond to edges between close areas in the anatomic template. The average matrices obtained

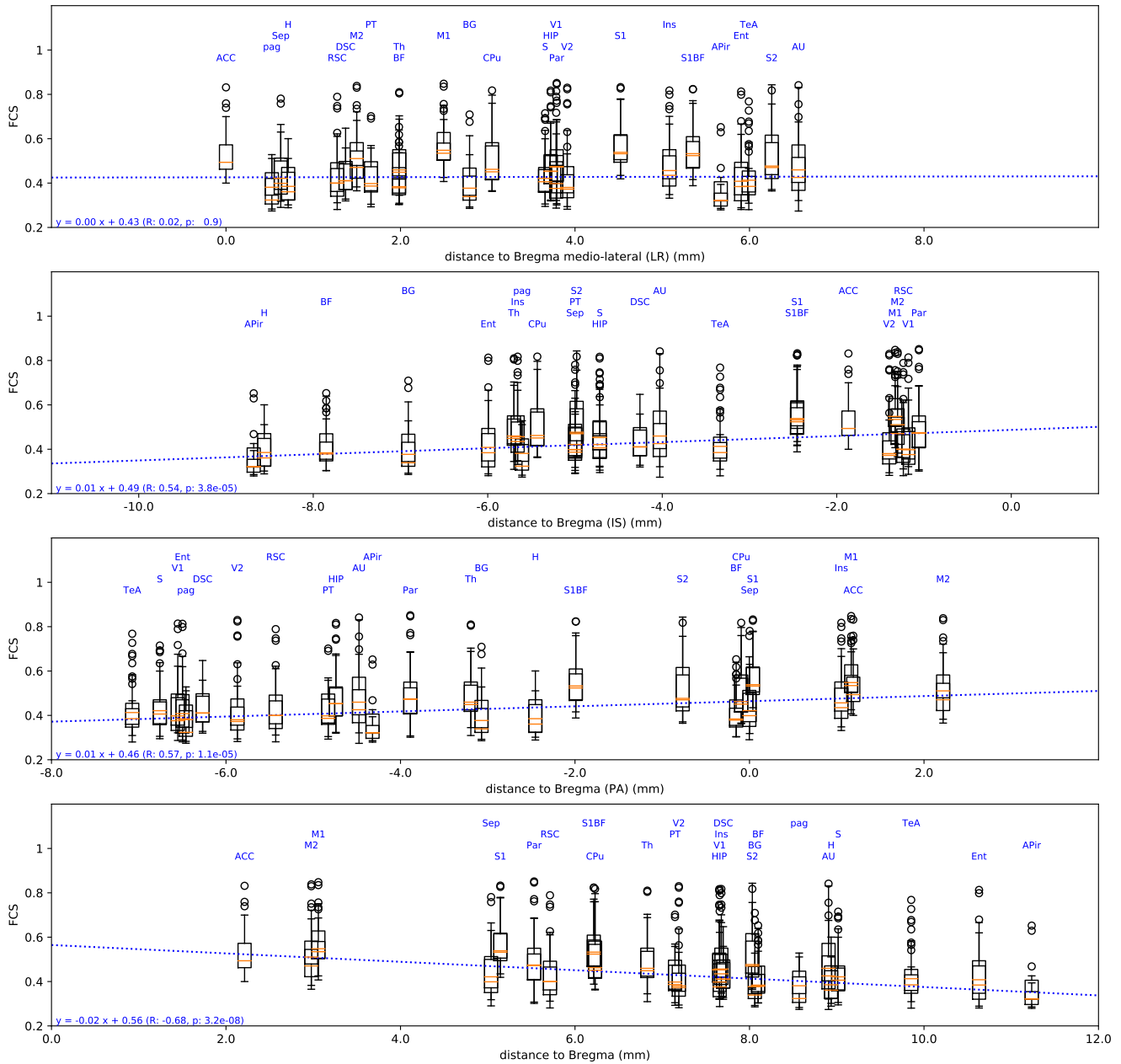

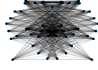
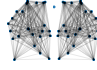
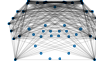

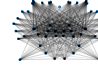


Figure H.17: Distribution of FCS versus spatial position of areas. The origin Bregma is at (0, 0, 0) in the LR, IS, AP coordinate system. A linear regression is fitted with median values of FCS. a) For medio-lateral positions (LR axis). b) For dorso-ventral positions (IS axis). c) For antero-posterior positions (PA axis). d) For Euclidean distances to Bregma.

Table H.3: Distributions of connections per group.

	ACC	inter	intra	c - c	s - s	c - s
						
$\rho = 0.05$						
Eto-L	16 \pm 0	27 \pm 2	55 \pm 1	48 \pm 3	17 \pm 3	17 \pm 2
Iso-L	11 \pm 1	40 \pm 1	48 \pm 2	73 \pm 4	11 \pm 5	2 \pm 1
Iso-W	19 \pm 0	42 \pm 1	38 \pm 1	65 \pm 3	9 \pm 3	4 \pm 1
Med-L	13 \pm 1	41 \pm 1	44 \pm 1	73 \pm 3	10 \pm 2	2 \pm 0
Ure-L	2 \pm 0	1 \pm 0	96 \pm 1	56 \pm 4	29 \pm 4	11 \pm 3
$\rho = 0.1$						
Eto-L	13 \pm 0	34 \pm 2	51 \pm 1	40 \pm 1	17 \pm 2	27 \pm 1
Iso-L	9 \pm 0	42 \pm 1	48 \pm 2	66 \pm 5	15 \pm 5	8 \pm 1
Iso-W	14 \pm 0	43 \pm 1	42 \pm 1	56 \pm 2	13 \pm 4	16 \pm 2
Med-L	12 \pm 0	41 \pm 0	46 \pm 0	61 \pm 3	16 \pm 3	10 \pm 1
Ure-L	3 \pm 0	4 \pm 1	92 \pm 2	45 \pm 5	31 \pm 4	19 \pm 2
Full	4	49	47	30	18	48

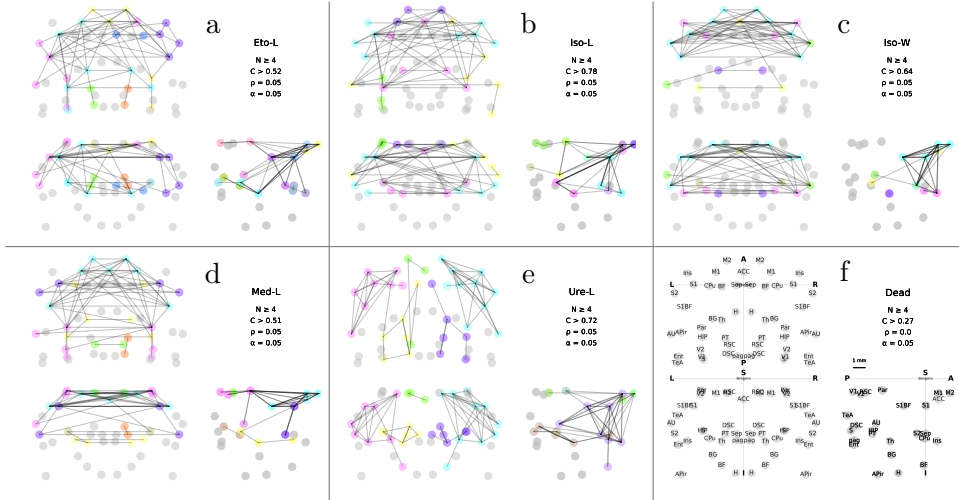
Mean \pm SEM are given in %. Notations: interhemispheric (inter), intrahemispheric (intra), cortex (c), subcortical (s)

1111 with at least significant values from 4 animals are also represented as graphs in Fig. I.38b. Con-
 1112 nections are enhanced, with enhanced differences between groups. No connections are persistent
 1113 in the Dead group. The number of significant values obtained on each connections is displayed
 1114 in Fig. I.38c. where a probability of 1 indicates that all rats of the group have this connection
 1115 significant. Stable networks within groups are enhanced.

1116 The observations that can be made on average graphs across group Fig. I.38 may also be
 1117 observed on individual graphs (Fig. I.32 to Fig. I.37):

- 1118 • For Eto-L, there is a widespread fronto-parietal complex associating frontal and inter-hemispheric
 1119 sensory communities, with shared connections between left and right cortical areas. The con-
 1120 nection with a large subcortical area is preserved with an important role of the thalamus.
- 1121 • For Iso-L, regarding cortical areas, there are widespread fronto-parietal, ipsi- and inter-
 1122 hemispheric communities containing the motor area in one hemisphere connected to its
 1123 contralateral sensory area. There are wide subcortical communities associated to cortical
 1124 communities. The cortical-subcortical connections mediated by Th and HIP are part of the
 1125 highly correlated coefficients, and indicate connections with visual areas.
- 1126 • For Iso-W, only four communities are put in evidence: a widespread cortical, well-connected
 1127 module; an isolated subcortical interhemispheric Th-HIP; An ACC-CPU module well con-
 1128 nected to cortical areas and an Ins module, more or less present in individuals.
- 1129 • For Med-L, there is a widespread inter-hemispheric fronto-parietal community connected
 1130 to an inter-hemispheric sensory module connected to HIP and RSC. The subcortical inter-
 1131 hemispheric communities is weakly connected to cortical areas.
- 1132 • For Ure-L, large left and right cortical fronto-parietal communities are shown. These two
 1133 cortical left-right communities are weakly connected. Two subcortical left-right communities
 1134 are also disconnected. There are few connections between these cortical-subcortical commu-
 1135 nities. The connections between cortical-subcortical communities, left and right communities
 1136 are weak. The role of ACC seems weaker than in other groups.

I - $\rho = 0.05$



II - $\rho = 0.10$

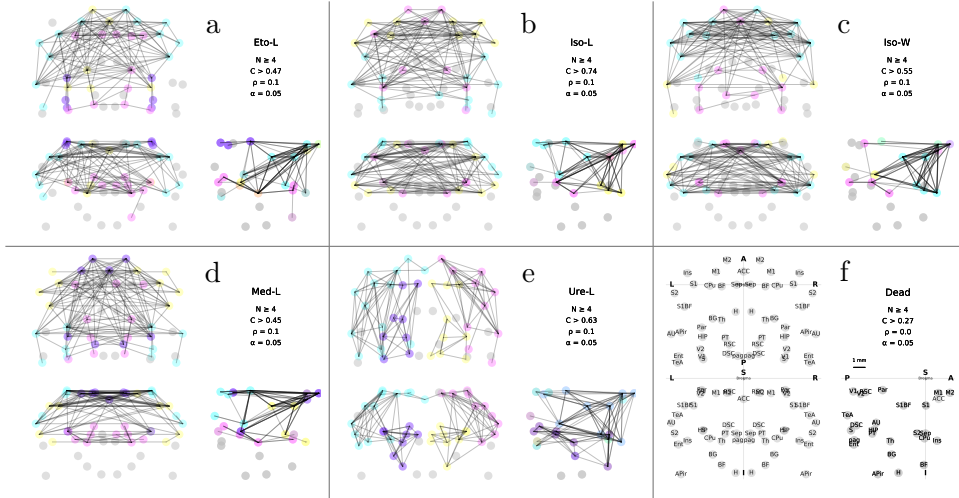
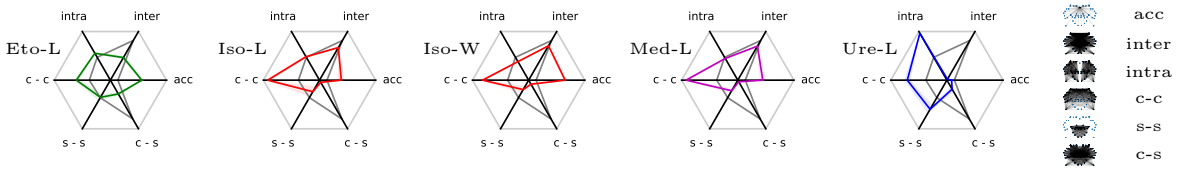


Figure H.18: Graphs based on the average correlation matrices for each group at two density: I) by taking the 63 most significant correlated values (density = 0.05) with at least 4 animals; II) by taking the 127 most significant correlated values (density = 0.1) with at least 4 animals.

I - $\rho = 0.05$



II - $\rho = 0.10$

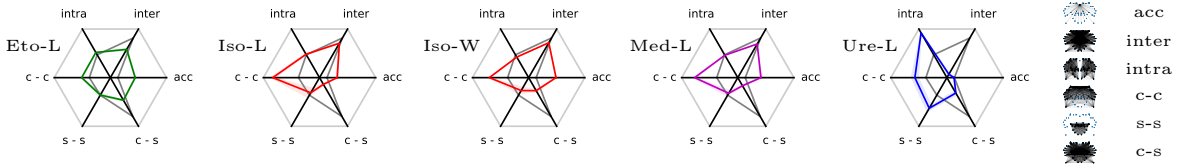


Figure H.19: Radar plots for the distributions of connections for a) $\rho = 0.05$ and b) $\rho = 0.1$. The gray curve corresponds to the fully connected graph (Full).

1137 *Appendix H.6. Comparison of graphs at different densities*

1138 Distributions of connections per wide areas are given in Table H.3 and Fig. H.19 for the two
 1139 densities $\rho = 0.05$ and $\rho = 0.1$. The comparison of values between densities indicates that from
 1140 the low density graphs at $\rho = 0.05$ to the dense one at $\rho = 0.1$, the ratio of c-s connections
 1141 increased for all groups, especially for Med-L and Iso-W, towards the ratio of the complete graph.
 1142 For these groups, the c-c balance decreases and the s-s balance increases. This is also observed
 1143 on the global patterns observed in Fig. H.18 for $\rho = 0.05$ and $\rho = 0.1$. In vivo graphs differ
 1144 from the theoretical full-graph, which has a small ACC contribution (4%), and equivalent inter-
 1145 and intra-hemispheric connections. In vivo, the contribution of ACC is comparable across groups
 1146 (between 9 and 14 %), except for Ure-L for which it barely contributes (3 %) (values given for
 1147 the density $\rho = 0.1$ but same comparisons can be drawn from $\rho = 0.05$). Ure-L also differs by
 1148 the fact that most connections (92 %) are intra-hemispheric rather than inter-hemispheric (4 %).
 1149 For the other groups, the balance between inter-hemispheric and intra-hemispheric proportions
 1150 are comparable with less intra-hemispheric connections for the Eto-L group. For this group, the
 1151 cortical-subcortical proportion is the highest one (27 %), to the detriment of the cortical-cortical
 1152 proportion (the lowest one). Iso-L shows the lowest proportion of subcortical-cortical connections
 1153 (8 %) and the highest proportion of cortical cortical connections (66 %) and is comparable with
 1154 Iso-W and Med-L. A graphical comparison using radar profiles is proposed in Fig. H.19, that
 1155 highlights the similarities and dissimilarities between groups.

1156 **Appendix I. Supplementary figures**

1157 *Appendix I.1. 1*

1158 *Appendix I.2. 2*

1159 *Appendix I.3. 3*

1160 *Appendix I.4. 4*

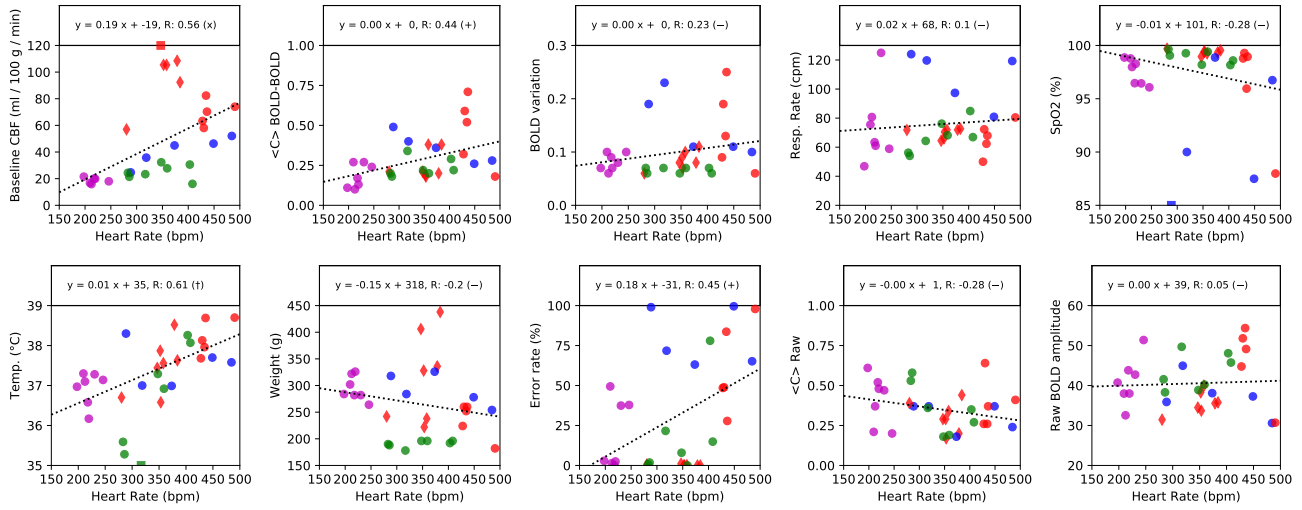


Figure I.20: Distributions of variables per group with scatter plots as a function of HR. Outliers are marked with a square. A linear trend is computed without the outliers.

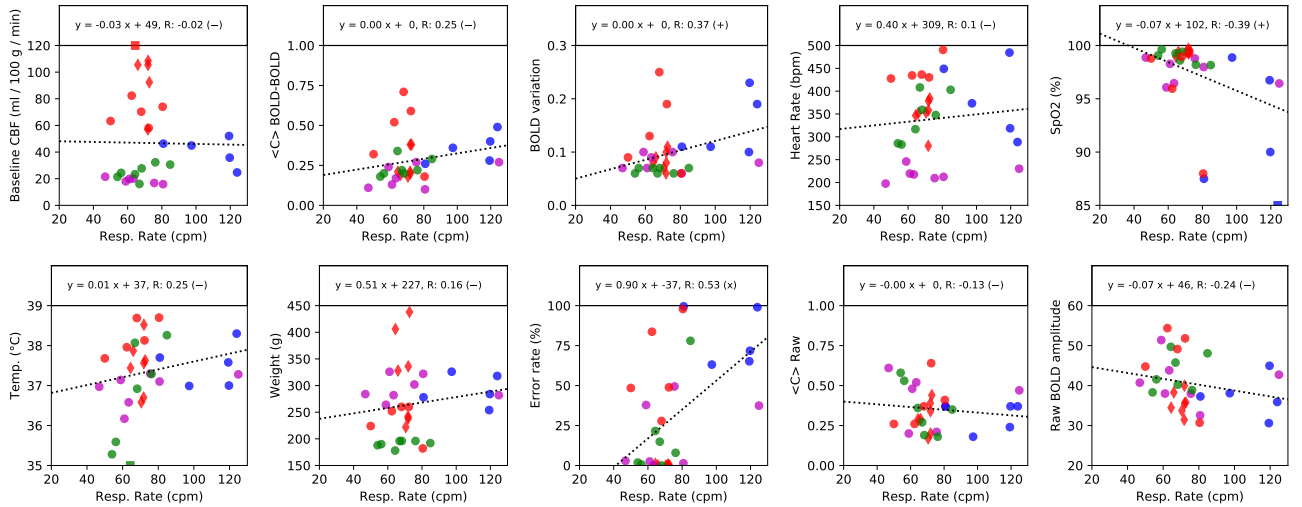


Figure I.21: Distributions — scatter plots — as a function of RR.

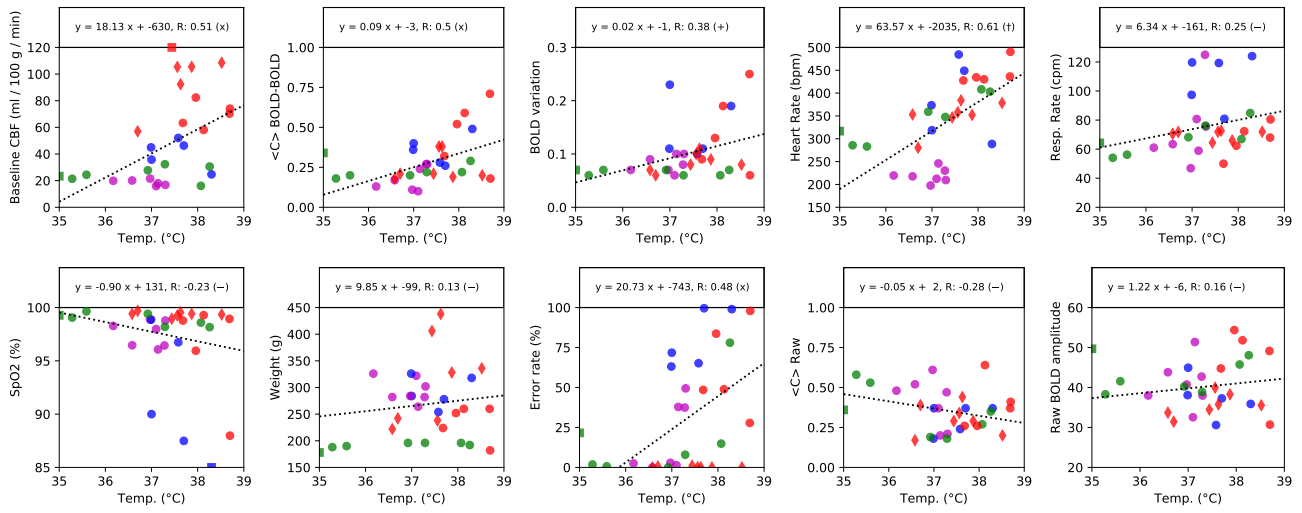


Figure I.22: Distributions — scatter plots — as a function of Temp.

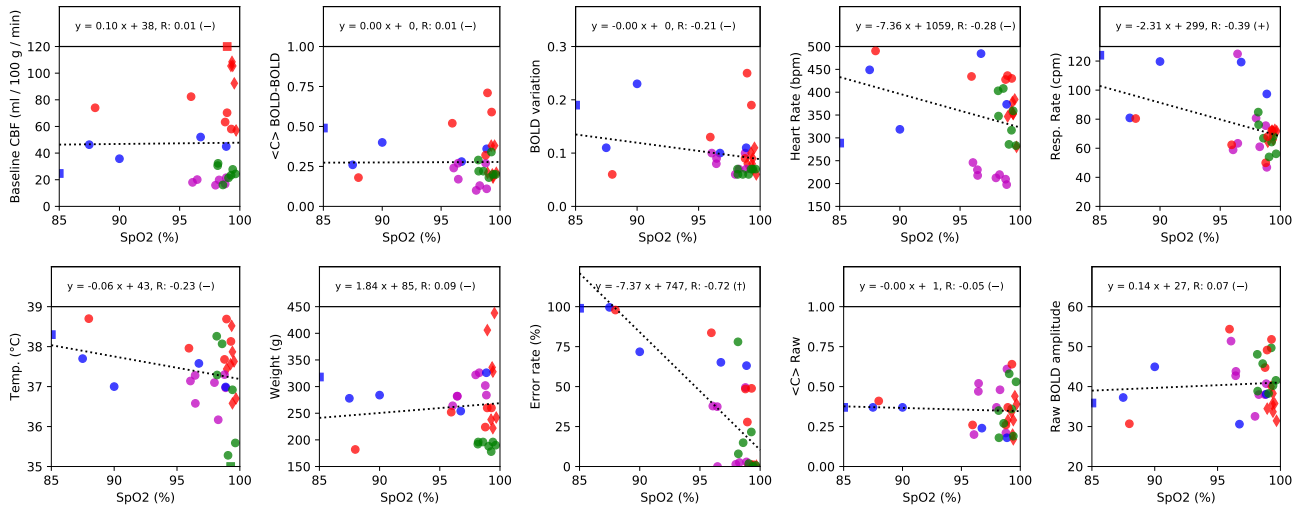


Figure I.23: Distributions — scatter plots — as a function of SpO2.

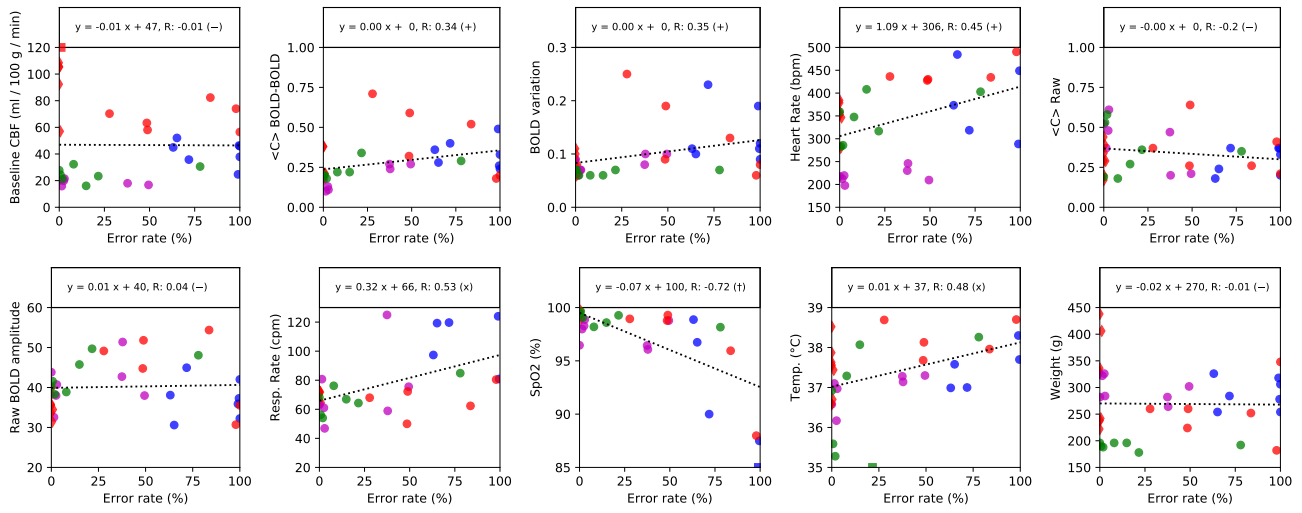


Figure I.24: Distributions — scatter plots — as a function of Error rate.

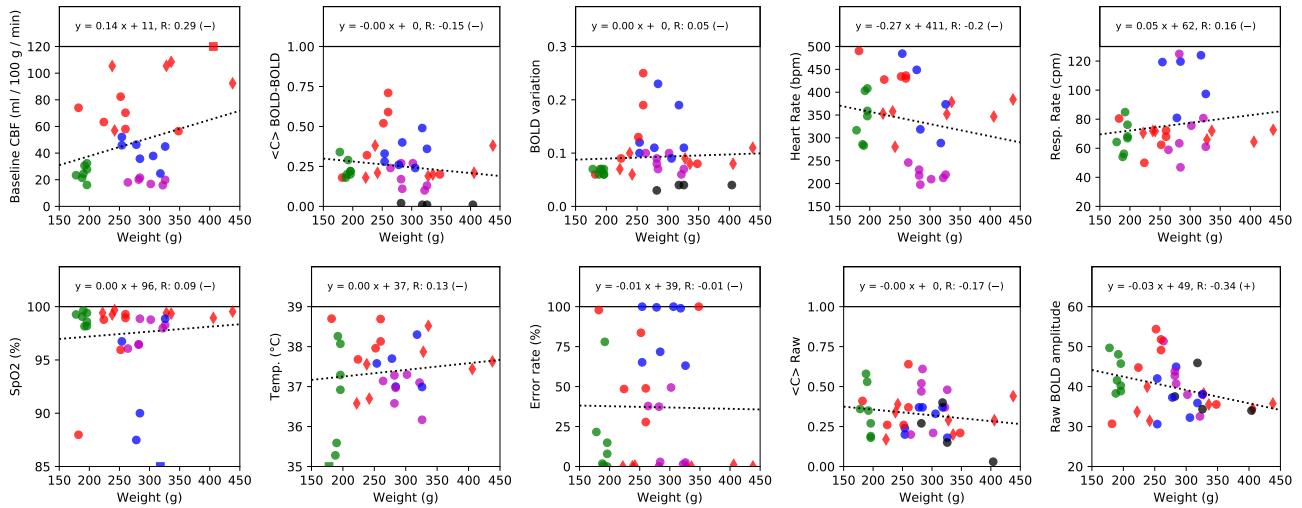


Figure I.25: Distributions — scatter plots — as a function of Weight.

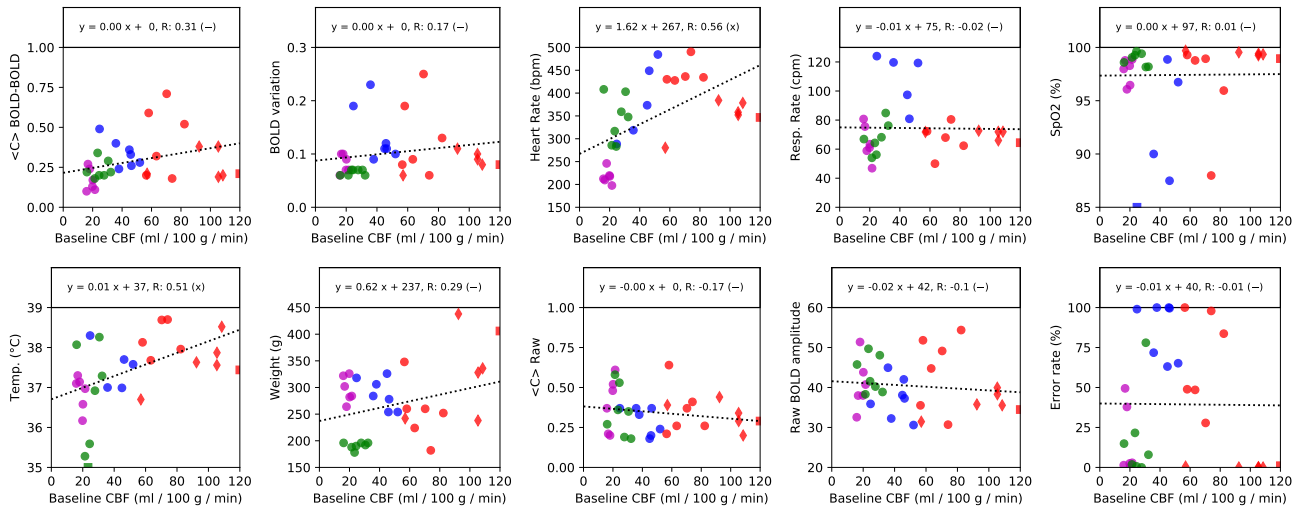


Figure I.26: Distributions — scatter plots — as a function of CBF.

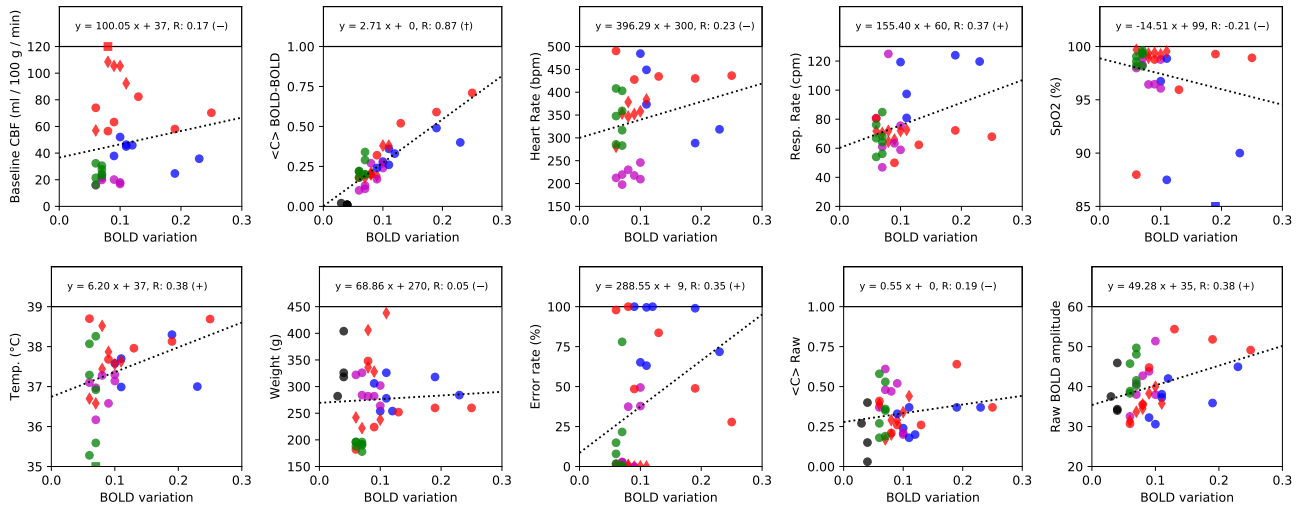


Figure I.27: Distributions — scatter plots — as a function of BOLD variations.

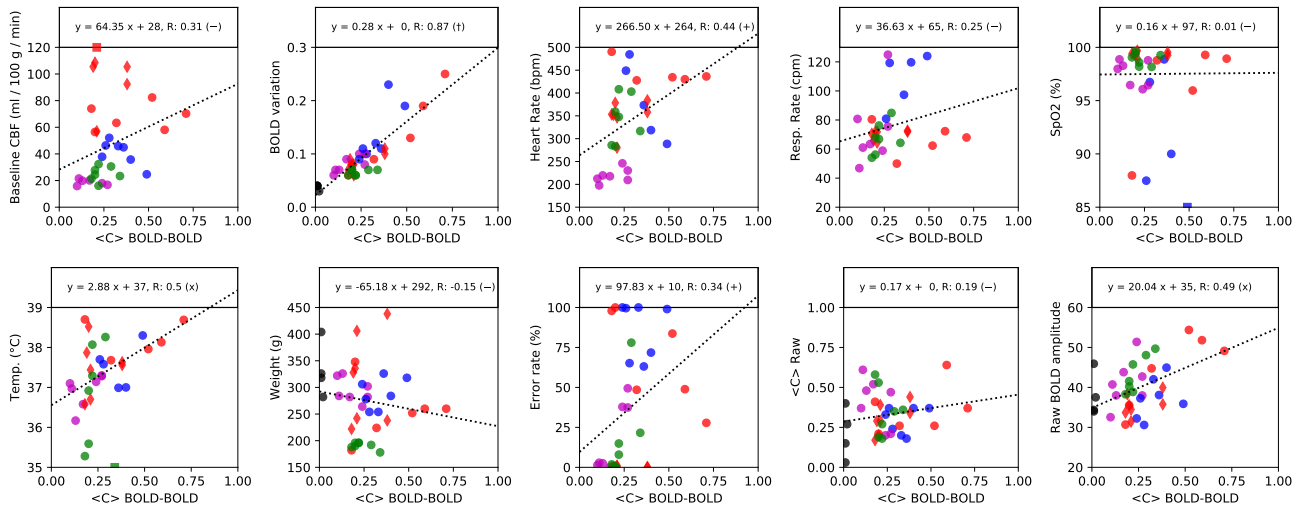


Figure I.28: Distributions — scatter plots — as a function of average correlations $\langle C \rangle$.

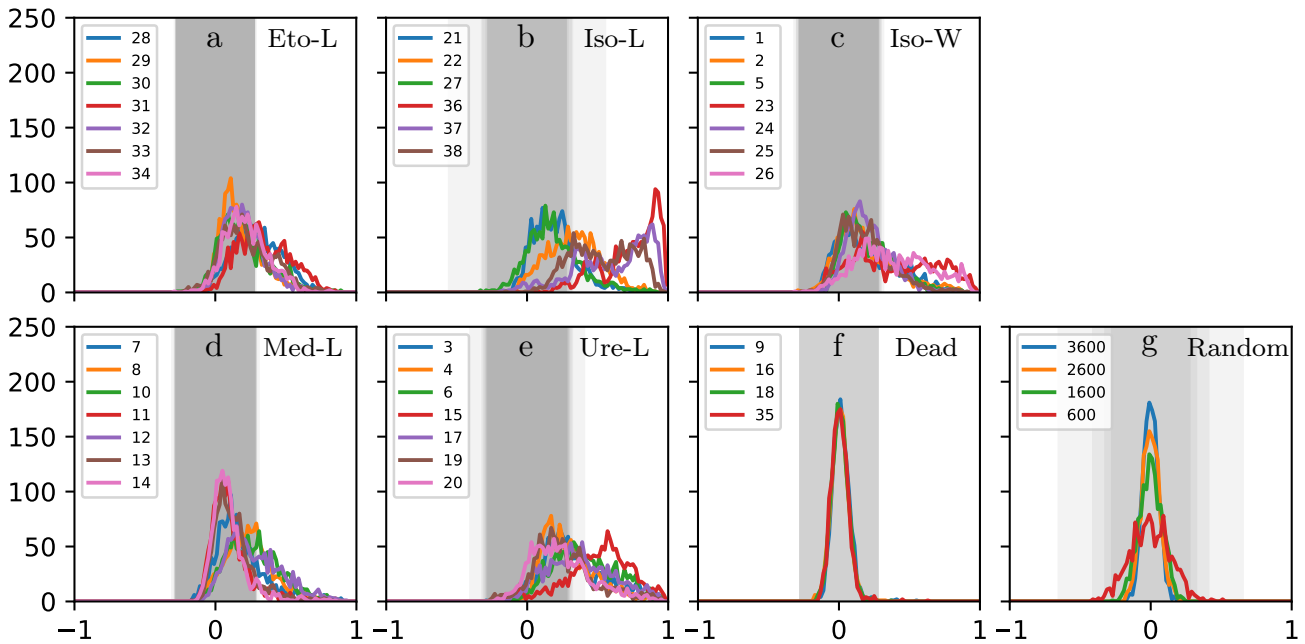


Figure I.29: Histograms of the BOLD-BOLD correlations per group in frequency band cD4. Histograms are estimated on 100 bins between $[-1, 1]$: a) – f) per anesthetic and for the Dead group with one color per animal; g) for simulated signals obtained with random values with the same number of areas and signal processing methods with different number of samples given in legend. The gray range represents the two-sided distribution of correlations below significance level given by the Bonferroni threshold.

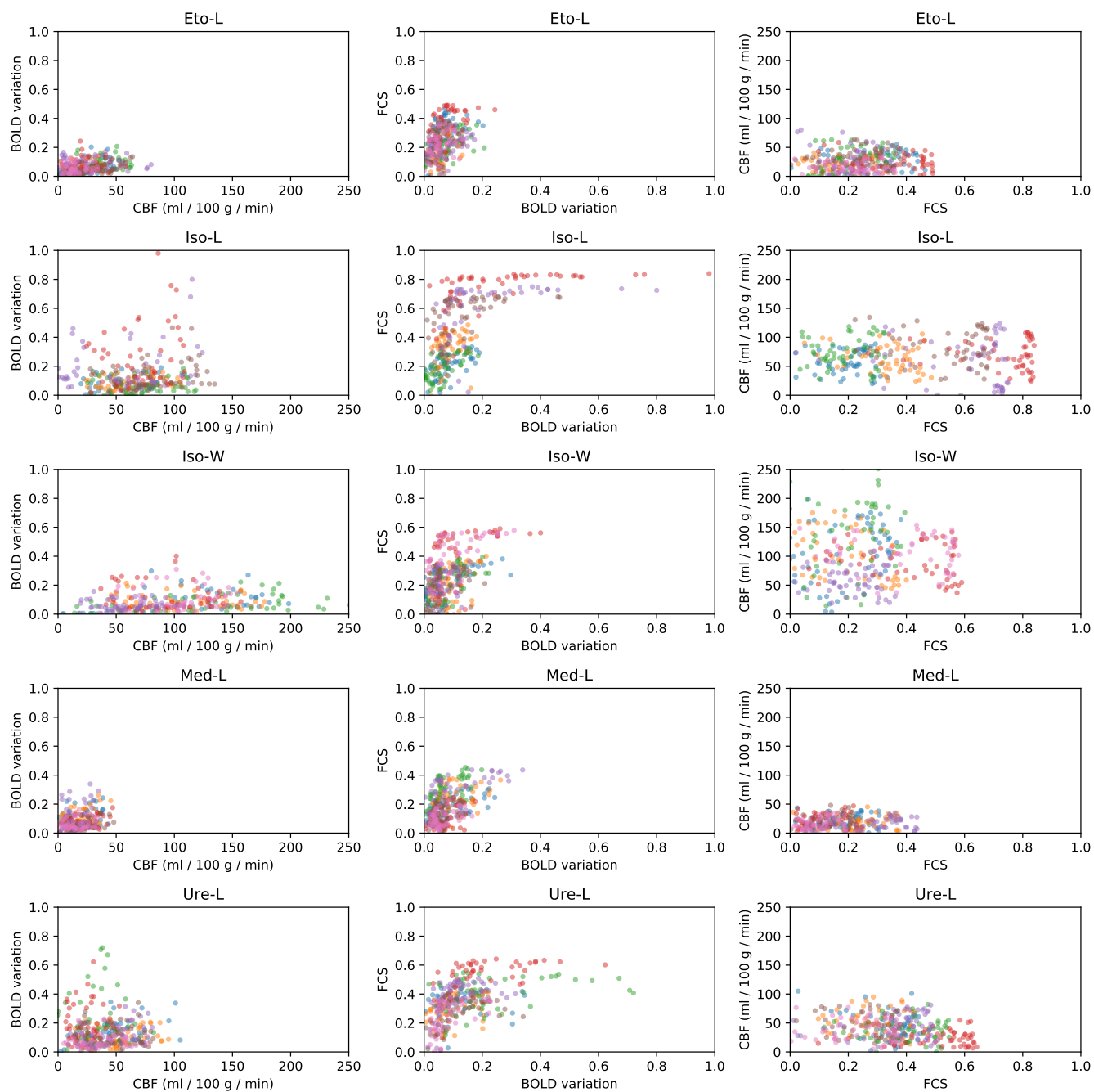


Figure I.30: Scatter plots per group between baseline CBF, BOLD variation and FCS. Dots with the same color belong to the same animal.

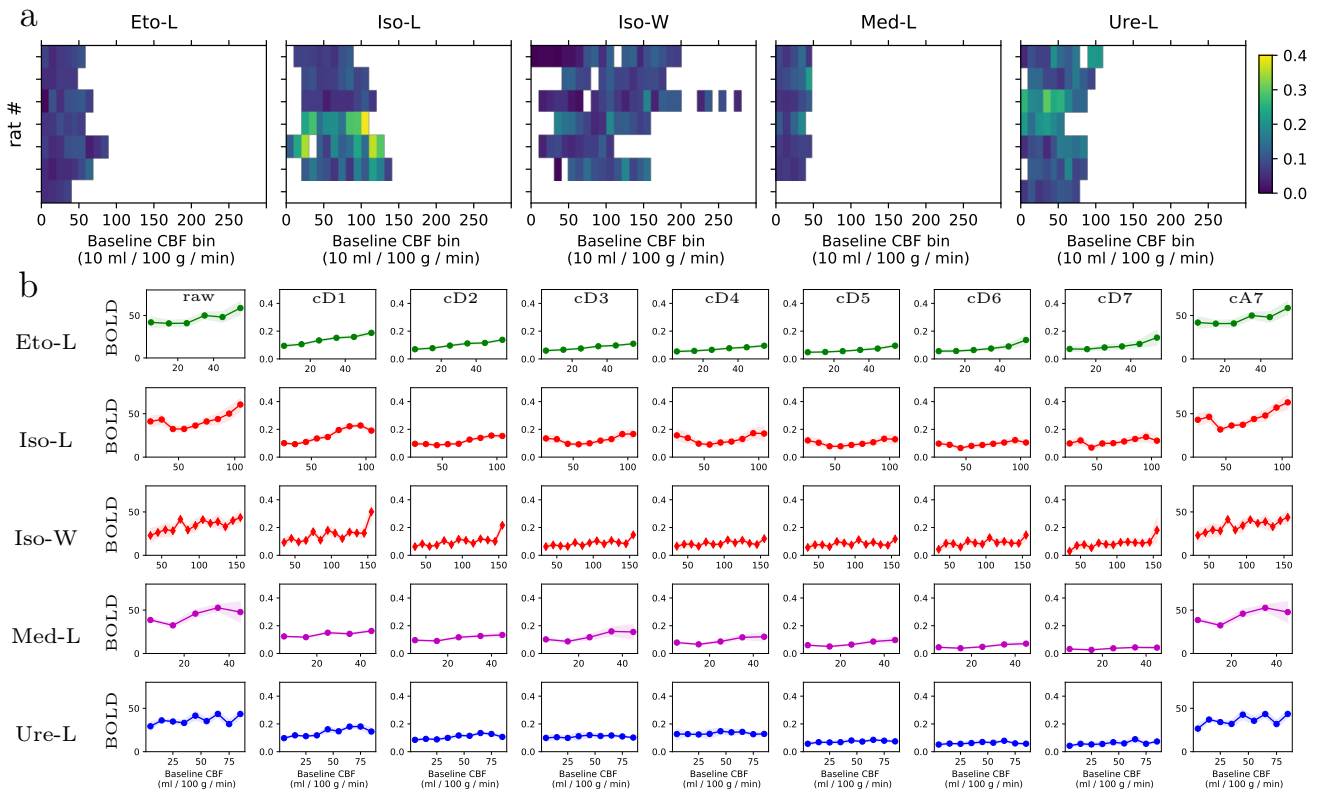


Figure I.31: Influence of population and frequency bands. a) BOLD variation as a function of CBF, for each anesthetized group. Each row represents one animal. BOLD variation is coded using the color scale on the right. b) BOLD amplitude for raw BOLD signal or variations versus CBF per frequency band and anesthetized group. BOLD variation in the cD4 band is presented in the main paper.

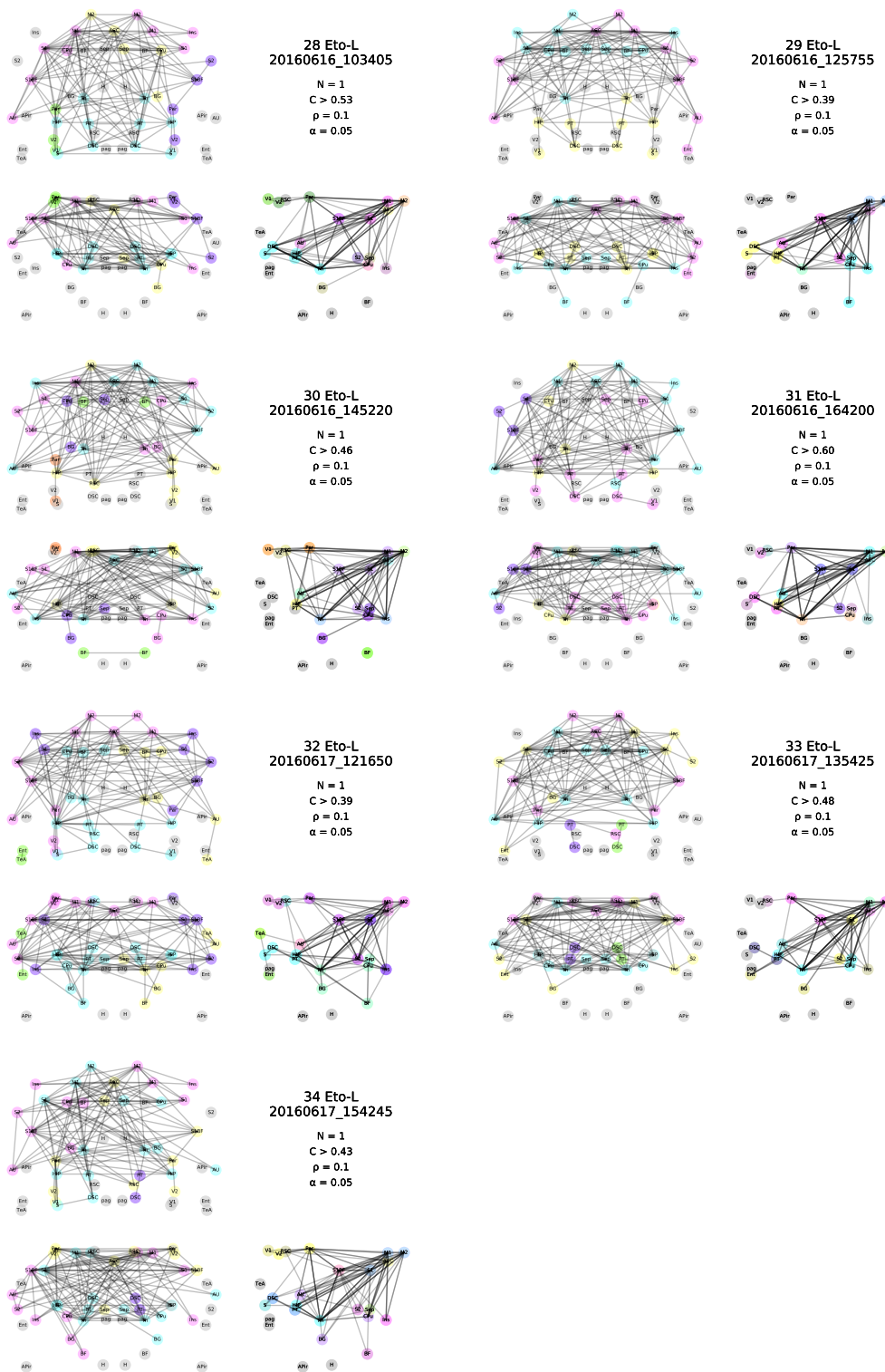


Figure I.32: Individual graph - Eto-L

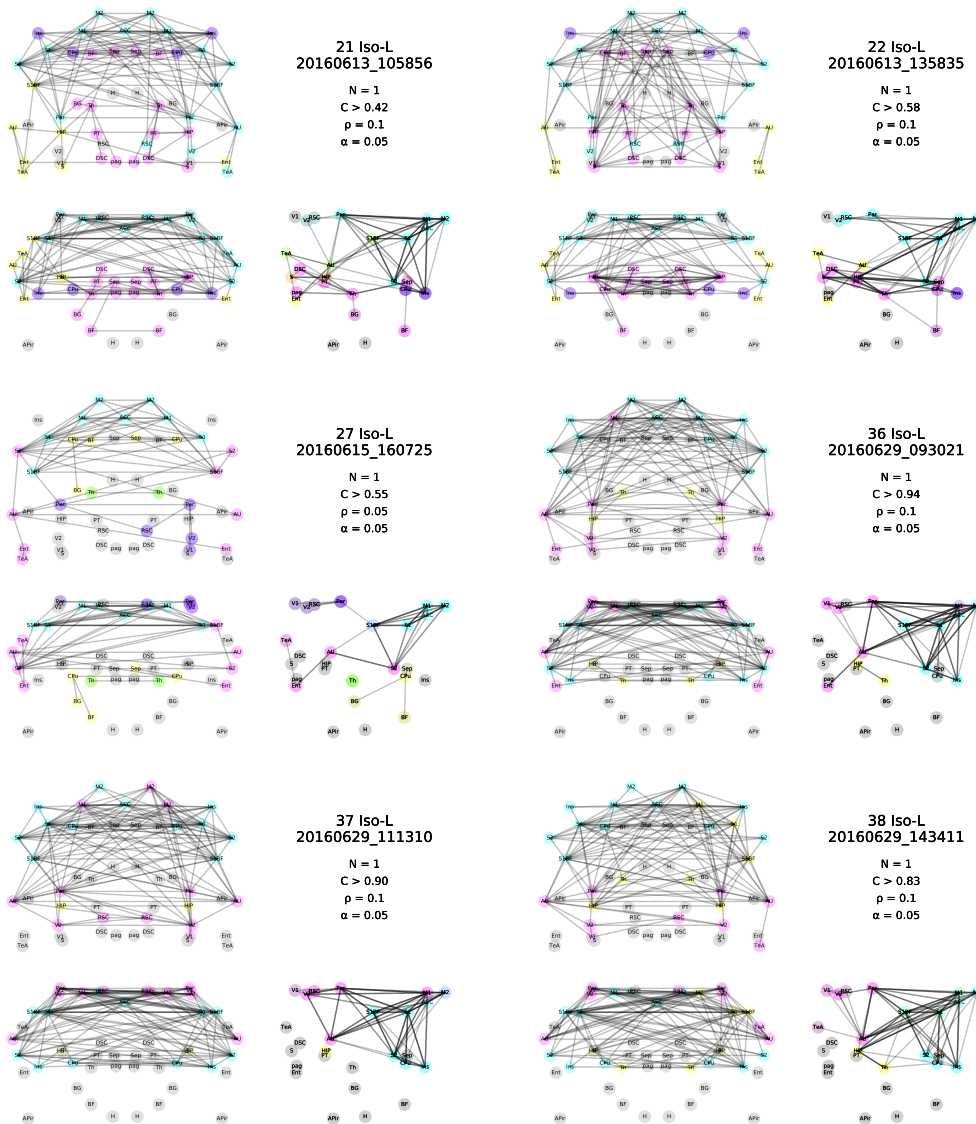


Figure I.33: Individual graph - Iso-L

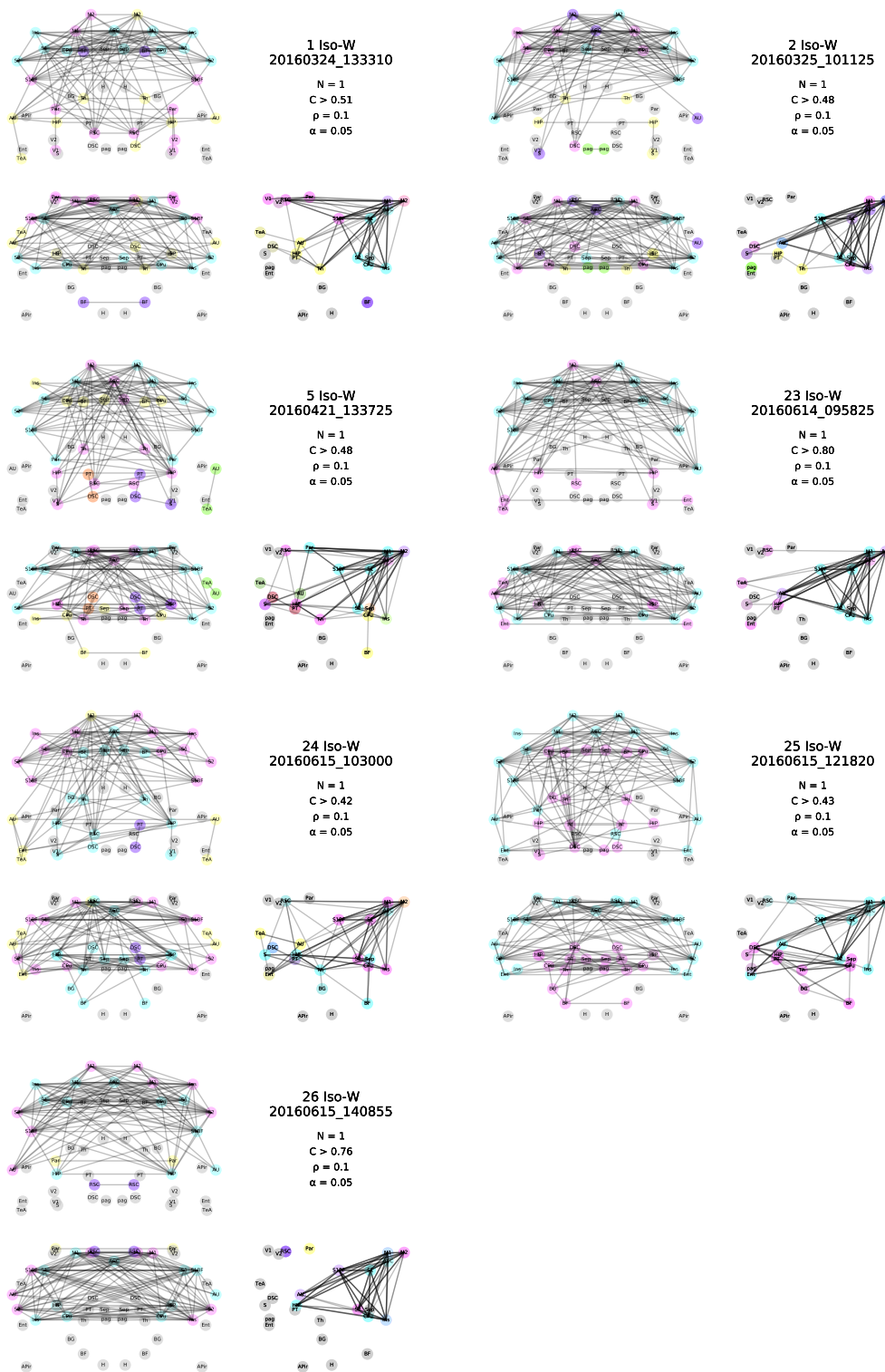


Figure I.34: Individual graph - Iso-W

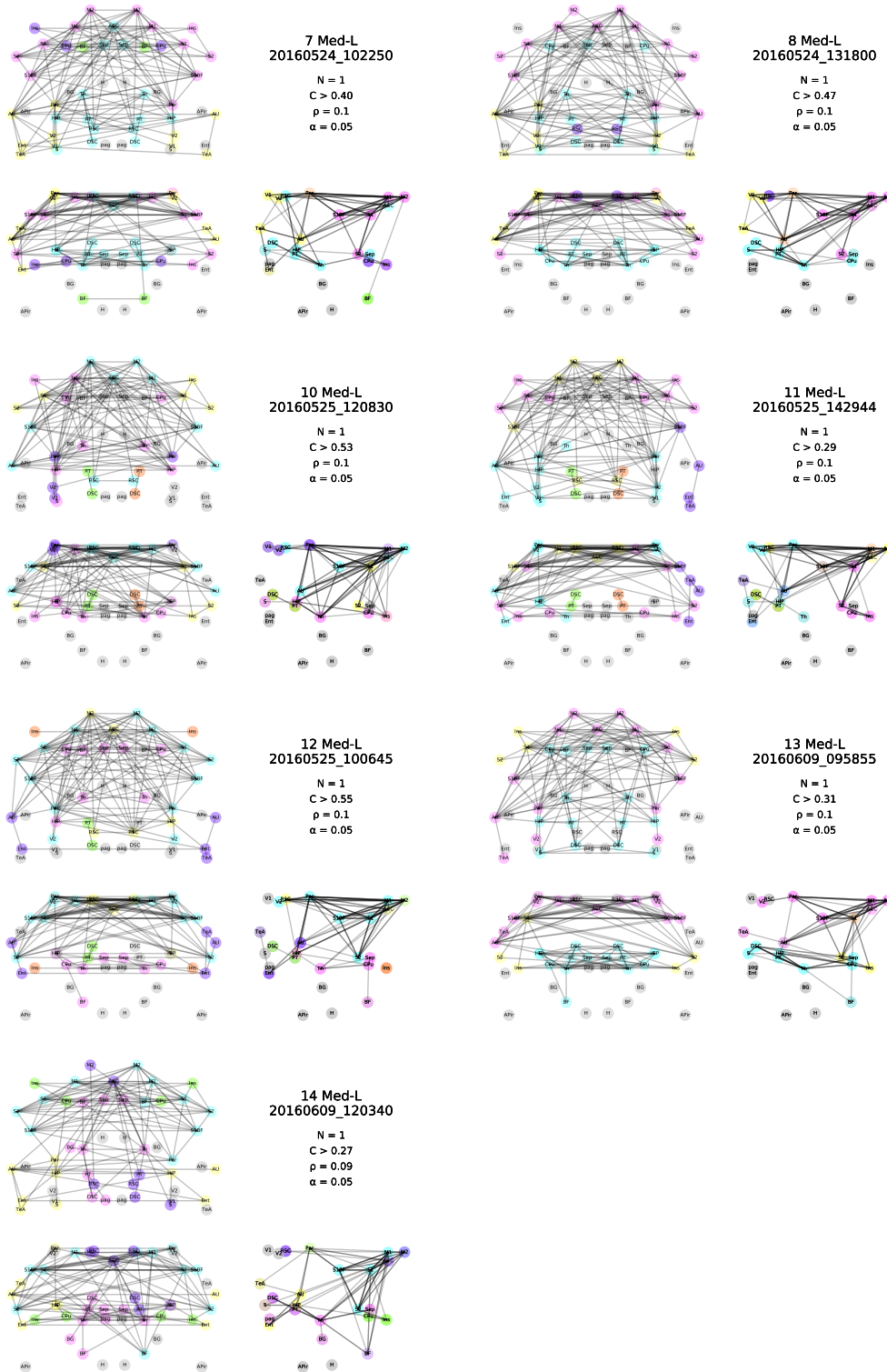


Figure I.35: Individual graph - Med-L

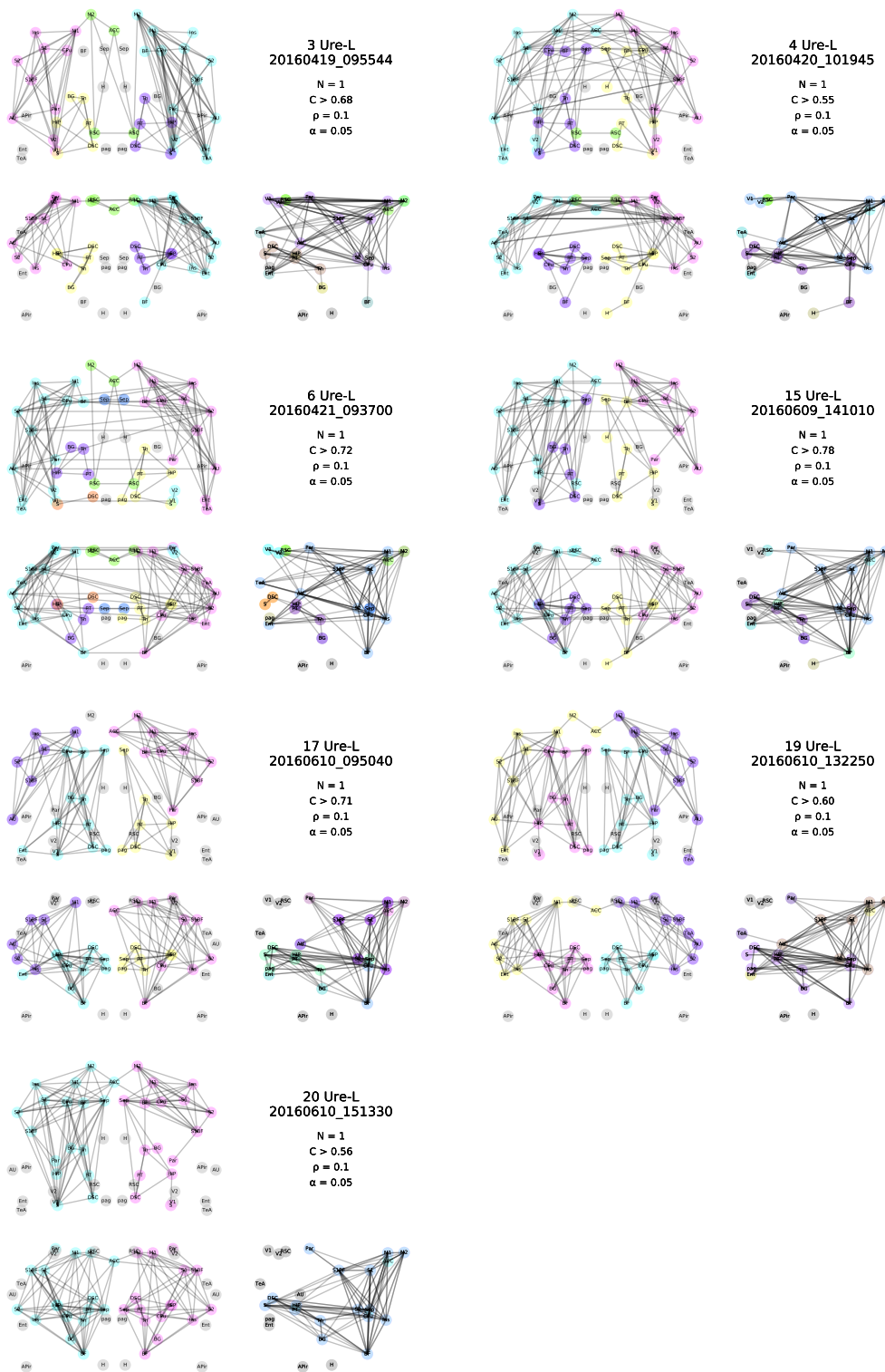


Figure I.36: Individual graph - Ure-L

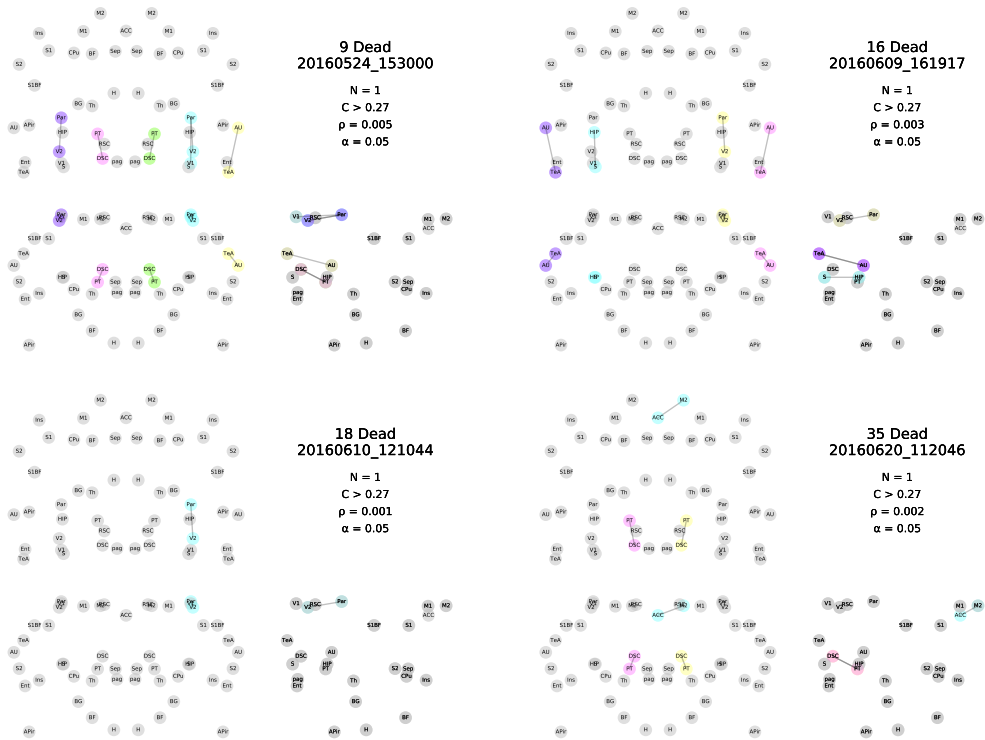


Figure I.37: Individual graph - Dead

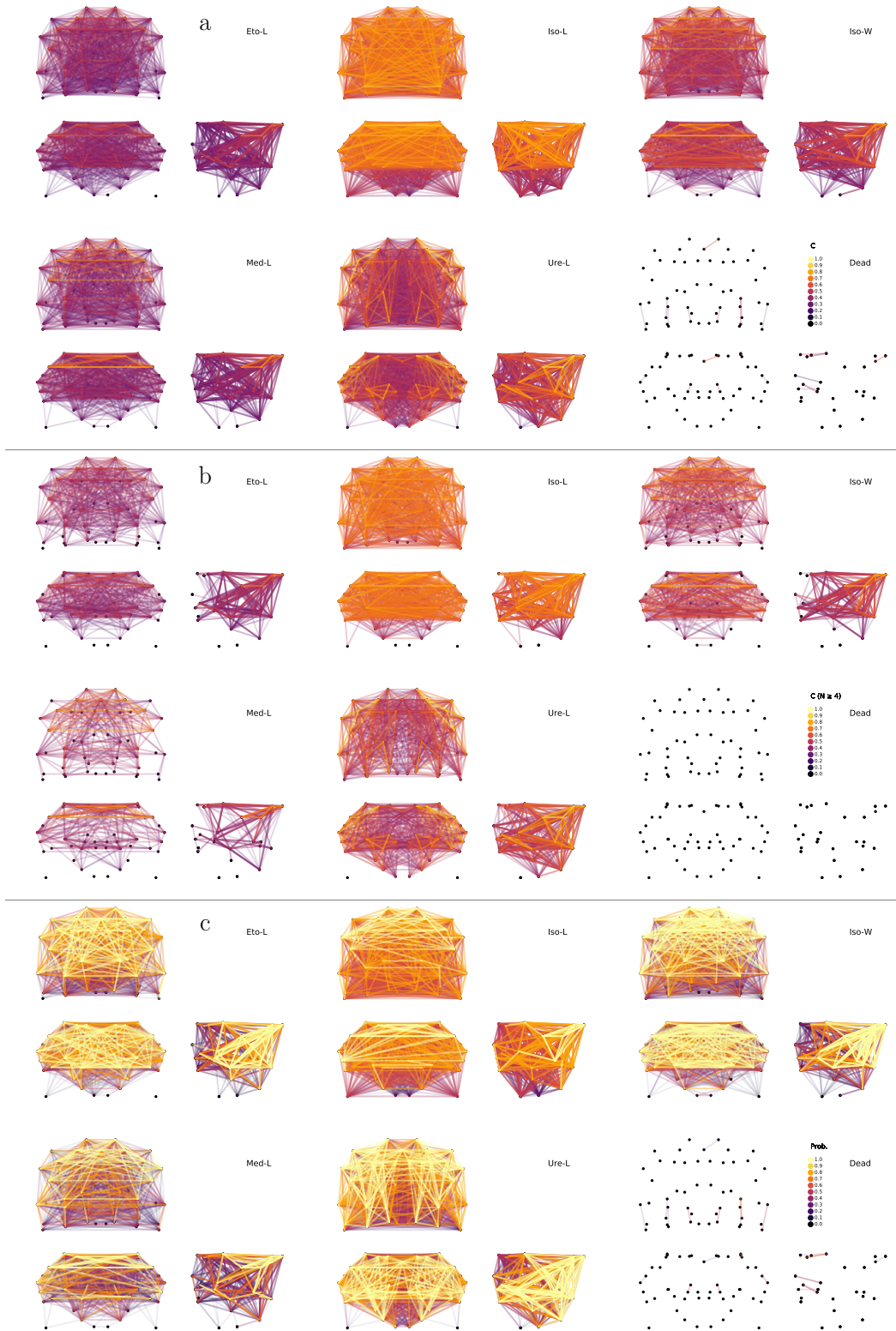


Figure I.38: Sorted Full Graph - Graphs with superimposed edges with the lowest on the background and the highest on the foreground. In these graphs, all available statistically significant edges are plotted for: a) average correlations; b) average correlations with at least 4 animals; c) probability of significant connections. Colors represent weights truncated at one decimal.